*Romanian Reports in Physics, Vol. 68, Supplement, P. S621–S698, 2016*

# PHOTOFISSION EXPERIMENTS AT ELI-NP

D.L. BALABANSKI[1,*], F. IBRAHIM[2], A. KRASZNAHORKAY[3], I. BOZTOSUN[4], D. CHOUDHURY[1], S. COBAN[1,4], P. CONSTANTIN[1], L. CSIGE[3], P.V. CUONG[5], T. DICKEL[6], H. DJAPO[4], I. DOBRIN[7], S. ESSABAA[2], D. FILIPESCU[1], S. FRANCHOO[2], G. GEORGIEV[8], I. GHEORGHE[1,9], D. GHITA[1,10], T. GLODARIU[1,10], M. GUPTA[11], A. JOKINEN[12], J. KAUR[1], N. MARGINEAN[10], R. MARGINEAN[10], I. MOORE[12], H. PENTILLA[12], C. PETCU[1], W. PLASS[6], T. SAVA[10], G. SAVARD[13], C. SCHEIDENBERGER[6], D. YORDANOV[2]

[1]ELI-NP, "Horia Hulubei" National Institute for Physics and Nuclear Engineering, 30 Reactorului Street, RO-077125, Bucharest-Magurele, Romania
[2]Institut de Physique Nucleaire d'Orsay, 91406 Orsay, France
[3]Institute of Nuclear Research, Hungarian Academy of Sciences, 4001 Debrecen, Hungary
[4]Akdeniz University, Dumlupinar Bulvari, 07058 Antalya, Turkey
[5]Institute of Physics, Vietnam Academy of Science and Technology, Hanoi, Vietnam
[6]GSI Helmholtz Centre for Heavy Ion Research, Planckstrasse 1, 64291 Darmstadt, Germany
[7]National Institute for R&D in Electric Engineering ICPE-CA, 030138 Bucharest, Romania
[8]CSNSM, IN2P3-CNRS, Universite de Paris Sud, 91405 Orsay, France
[9]Faculty of Physics, University of Bucharest, 077125 Bucharest-Magurele, Romania
[10]"Horia Hulubei" National Institute for Physics and Nuclear Engineering, 30 Reactorului Street, RO-077125, Bucharest-Magurele, Romania
[11]Manipal University, Manipal Centre for Natural Sciences, Manipal, Karnataka 576104, India
[12]Department of Physics, University of Jyvaskyla, FI-40351 Jyvaskyla, Finland
[13]Physics Division, Argonne National Laboratory, Argonne, IL 60439, USA
*Corresponding author *Email:* dimiter.balabanski@eli-np.ro

*Abstract*. Three photofission experimental programs are proposed to be carried out with the brilliant gamma beams that will be available at the ELI-NP facility. First, we will measure the absolute photofission cross-sections of actinide targets and will study the energy, mass and charge distributions of fission fragments, as well as of ternary fission. We further propose to measure the angular distribution of photofission fragments. One of the goals is to resolve the fine structure of the isomeric shelf and to observe the clusterisation phenomena in super- and hyper-deformed actinide states. For this, an array of Bragg ionization chambers and an array of thick gas electron multipliers will be constructed. Second, the structure of exotic nuclei produced in photofission will be studied, in particular, isotopes of refractory elements, by developing an ISOL-type facility with an ion-guide, a RFQ ion cooler and a mass separator to separate and transport the isotopes of interest to the measurement stations. Last, we aim at studies of *g*-factors of short-lived nanosecond isomers since they are difficult to be measured anywhere else. For measurements and studies of the γ decay of excited states in exotic nuclei, we intent to use the detectors of the ELIADE array.

*Key words*: ELI-NP γ beams, photofission, transmission resonances, ternary fission, Bragg ionization chamber, GEM detectors, neutron-rich nuclei, IGISOL, gas stopping cell, nuclear magnetic moments, in-beam gamma spectroscopy

## 1. INTRODUCTION

Photofission measurements enable selective investigation of extremely deformed nuclear states in the light actinides and can be utilized to better understand the landscape of the multiple-humped potential energy surface (PES) in these nuclei. The selectivity of these measurements originates from the low and reasonably well-defined amount of angular momentum transferred during the photoabsorption process. High resolution studies can be performed on the mass, atomic number, and kinetic energy distributions of the fission fragments following the decay of well-defined initial states in the first, second and third minima of the PES in the region of the light actinides. We aim at investigating the heavy clusterization and the predicted cold valleys of the fission potential. Moreover, a special focus on the fission dynamics and clusterization effects in super- (SD) and hyper-deformed (HD) compound states will be addressed. On the other hand, by mapping the PES of the actinides the harmonicity of the potential barrier can be examined and the parameters of the fission barrier can be extracted. Fission barrier parameters are crucial inputs for cross section calculations in the Thorium-Uranium fuel cycle of $4^{th}$ generation nuclear power plants. The selectivity of the photofission measurements allows high-resolution investigation of fission resonances in photofission in the $2^{nd}$ and $3^{rd}$ minimum of the fission barrier of the light actinides. Detailed study of SD and HD states via transmission resonance spectroscopy is relevant also for a much cleaner energy production by an efficient transmutation of the long-living, most hazardous radioactive component of the nuclear waste, and by controlling the fission process with using entrance channels via HD states. Another topic which can be addressed is the search for exotic fission modes like true ternary fission, collinear cluster tripartition and “lead radioactivity”. It will be very interesting to study the nuclear fission accompanied by light charge particle emission, to measure the light particle decay of excited states and to search for the predicted enhanced α-decay of HD states of the light actinides. The high linear polarization of the Extreme Light Infrastructure – Nuclear Physics (ELI-NP) γ beams (above 99%) provides an opportunity to study the space asymmetry of the angular distribution of the fission fragments and the correlation between the space asymmetry and the asymmetry of the fission process.

Studies of neutron-rich nuclei, lying away from the valley of β stability, are main topic of nowadays nuclear structure research. Such nuclei are produced at isotope-separation on-line (ISOL) facilities in fission, or at in-flight facilities in projectile fragmentation at intermediate or relativistic energies. The low yield of the isotopes of interest is a major shortcoming of the in-flight method, while not all elements can be extracted from an ISOL target due to the long diffusion times of many of them. Photofission provides another possibility to create exotic nuclei in the laboratory. The γ beam at ELI-NP covers the energy of the giant dipole resonance (GDR), which makes it ideal for such studies. The isotopes of refractory elements

can be separated with the ion guide ISOL (IGISOL) technique. After their separation, the nuclei of interest will be transported to different measurement stations, such as a tape station for β-decay measurements, a multi-reflection time-of-flight system for mass measurements and collinear laser spectroscopy beam line for spin and nuclear moment measurements.

Fission fragments are emitted in excited states with angular momenta of about 20 $\hbar$. This provides an opportunity to study their γ decay using an in-beam technique. Such attempts have been done using spontaneous fission and thermal-neutron-induced fission ($n_{th}$-fission). Photofission provides another option for such studies. A unique feature of photofission is the possibility to measure *g*-factors of isomeric states, which cannot be done at neutron facilities, because of the large (n,γ) cross sections of the ferromagnetic materials, which are used for implantation of the nuclei of interest.

The material included in this TDR considers physics cases related to each of the three experimental techniques, discussed above, and the needed instrumentation for realizing the defined physics cases.

## 2. PHYSICS CASES

### 2.1 Studies of the 2nd and 3rd minimum of the fission barrier

The aim of this Technical Design Report (TDR) is to explore the connections between the nucleonic and the collective degree of freedom and, in general, to determine the intersection of the shell, collective and cluster models. To achieve our scientific goal, we plan to study different correlations in atomic nuclei, as well as their interrelations, such as dipole and quadrupole collectivity, and clustering effects in heavy systems.

In the actinide region, the appearance of a deep, local SD second minimum in the PES of the nucleus at large quadrupole deformations was already observed experimentally and described within the macroscopic-microscopic theoretical framework long time ago [1]. Later, unexplained structures in the fission cross sections of the light actinides pointed to extend the existing picture with the triple-humped fission barrier concept with a shallow 3rd minimum in the PES at extremely large quadrupole and large octupole deformations [2, 3]. Recently, it was found experimentally by Krasznahorkay *et al.* in several measurements on uranium isotopes that the 3rd minimum is in fact as deep as the 2nd minimum [4]. On the other hand, very recent self-consistent and microscopic-macroscopic calculations do not predict the existence of such a deep 3rd minimum [5, 6], which opens up a new puzzle on the physics of collective excitations with a large number of nucleons in the vicinity of the $N = 140$ SD and HD magic neutron number.

Theoretical considerations also predicted that, in a cluster description, the HD minimum consists of a spherical $^{132}$Sn-like component with magic neutron $N$ = 82 and proton $Z$ = 50 numbers complemented by an attached elongated second cluster of nucleons [7]. Since the fission mass distribution is distinctly determined by the configuration at the scission point, and the 3$^{rd}$ minimum is very close to the scission configuration, we expect that the mass distributions originating from the 3$^{rd}$ minimum exhibit a much more pronounced asymmetric mass distribution. However, such a dramatic effect of the shell structure has not been observed so far.

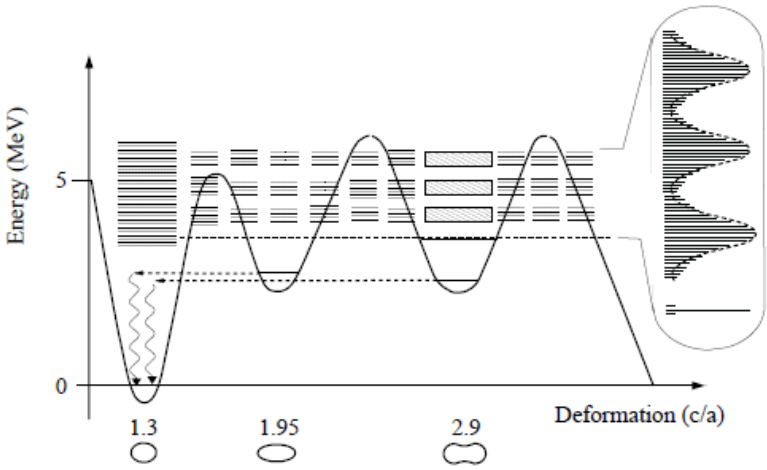


Fig. 1 − Schematical description of the occurrence of transmission resonances in the prompt fission probability through a triple-humped fission barrier. Reproduced from Ref. [9].

The experimental approach to investigate extremely deformed collective and single particle nuclear states of the light actinides is based on the observation of transmission resonances in the prompt fission cross section [8, 9]. For energies of the nuclear system below the maximum of the fission barriers, the wave functions in multi-humped barrier nuclei are concentrated within one of the minima of the deformed potential. Obviously, the tails of these wave functions penetrate the inner barriers and there is a certain degree of mixing between excitations in the first, second and third well. The main parameters, which define the degree of mixing, are the penetrability factors of the internal barriers. It is well known that the fission barrier can be studied by measuring the fission probability as a function of the excitation energy. If the fission barrier is more complex, *e.g.* multi-humped, the Hill-Wheeler transmission coefficient [10] cannot be used, because the picture is complicated by the presence of transition states which are due to the coupling of states originating from the different minima. Thanks to the resonant tunneling effect, such excited states can be mapped by measuring the fission probability as a function

of the excitation energy, as schematically indicated in Fig. 1. If the angular distribution of the fission fragments is also measured, then one can get information on the values of the nuclear spin and its projection $K$ on the symmetry axis of such excited states, as well.

Observing transmission resonances as a function of the excitation energy caused by resonant tunneling through excited states in the 3rd minimum of the potential barrier will allow the identification of the excitation energies of the HD states. Moreover, the observed states can be ordered into rotational bands, proving that the underlying nuclear shape of these states is indeed a HD configuration. For the identification of the rotational bands, the spin information can be obtained by measuring the angular distribution of the fission fragments. Furthermore, the PES of the actinides can be parametrized very precisely by analyzing the overall structure of the fission cross section and by fitting it with nuclear reaction (EMPIRE 3.1 [11] or TALYS 1.2 [12]) calculations.

Photofission measurements enable selective investigation of such deformed nuclear states and can be utilized to understand the landscape of the multiple-humped potential energy surface of the actinides much better. The selectivity of these measurements originates from the low and well-defined amount of angular momentum transferred during the photo-absorption process. So far, transmission resonances have been studied primarily in light-particle-induced nuclear reactions. These studies do not benefit from the same selectivity found in photo-nuclear excitation and consequently they are complicated by statistical population of the states in the 2nd (and 3rd) minimum with a probability of $10^{-4}$–$10^{-5}$. This leads to a typical isomeric fission rate from the ground-state decay of the shape isomer in the 2nd minimum of only about 1/sec. These measurements have also suffered from dominating prompt-fission background.

Until now, sub-barrier photofission experiments have been done only with bremsstrahlung photons and have determined integrated fission yields. In these experiments, the fission cross section was convoluted with the spectral intensity of the photon beam, resulting in a typical effective γ-ray bandwidth of only $\Delta E/E \approx 6\cdot 10^{-2}$. However, a plateau was observed in the fission cross section, referred to as the "isomeric shelf", presumably as a result of the competition between prompt and delayed photofission [13, 14]. Due to the lack of high resolution photofission studies in the corresponding energy region ($E \approx 4$–$5$ MeV), no experimental information exists to confirm this concept. ELI-NP offers an opportunity to overcome previous limitations. The capabilities of this next-generation γ beam system allow one to aim at identification of sub-barrier transmission resonances in the fission decay channel with integrated cross sections down to $\Gamma\sigma \sim 0.1$ eV·b. The narrow energy bandwidth will also allow for a significant reduction of the presently dominant background from non-resonant processes. Thus, ELI-NP is expected to allow preferential population and identification of transitional resonances in the

photofission cross section and ultimately to enable observation of the fine structure of the isomeric shelf.

A 0.3% bandwidth of the gamma beam, which corresponds to an energy resolution of 12–18 keV at 4–6 MeV is required to carry out experiments for the study of the transmission resonances. This energy resolution permits such studies in even-even actinides, where the level density is low enough. Fig. 2 shows the measured photofission cross-section of $^{238}$U in the γ-ray energy range of $E_\gamma$ = 4.7−6.0 MeV [4]. The experiment is performed at HIγS, Duke University, USA, which delivers nowadays the best gamma beams. However, the resolution is not good enough to resolve possible transmission resonances. The solid black line represents a fit of the data, assuming triple-humped barrier with 2$^{nd}$ and 3$^{rd}$ minima of equal depth, while the dashed blue line considers a double-humped barrier. At ELI-NP we plan to start with $^{232}$Th, $^{238}$U and study also some other even-even radioactive targets *e.g.* $^{242}$Pu, $^{230}$Th, $^{234}$U.

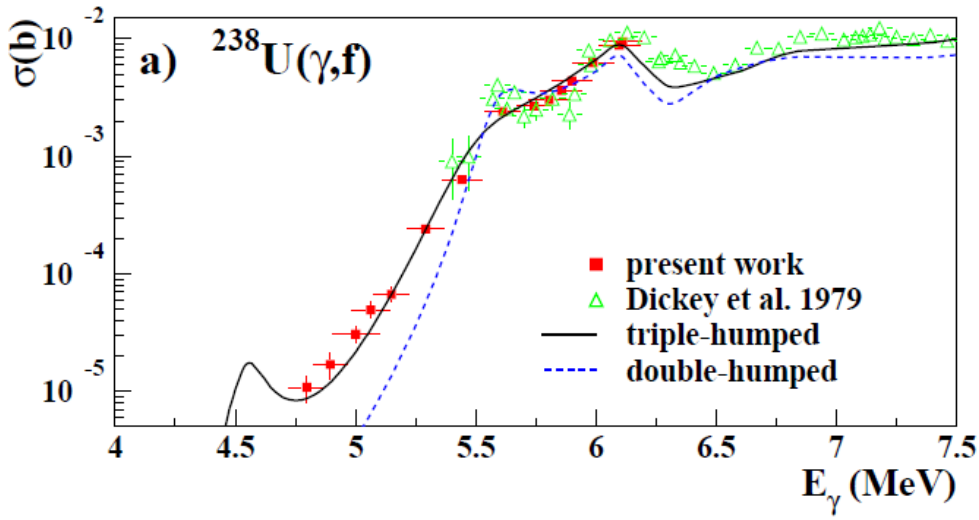


Fig. 2 − The measured photofission cross-section of $^{238}$U in the gamma-ray energy range of $E_\gamma$ = 4.7−6.0 MeV [4]. Reproduced with permission from the American Physical Society.

In short, mass and charge distributions, which will be measured in resonant tunneling experiments at ELI-NP, are easier to understand, especially for the cold fission when the fragments are not excited. In addition, the role of the Pigmy resonances in the entrance channel will be studied, too.

These studies call for developments of state-of-the-art fission detectors to exploit the unprecedented properties of the high-flux, Compton backscattered (CBS) γ beams having a very small, millimeter beam-spot size. A multi-target detector array is under development at the Institute for Nuclear Research of the Hungarian

Academy of Sciences (MTA Atomki) in Debrecen, Hungary, consisting of position sensitive gas detector modules based on the state-of-the-art thick gas electron multiplier (THGEM) technology [15]. The foreseen small γ beam-spot size allows the development of considerably more compact photofission detectors than those of before. Besides, the well-focused γ beam also defines a distinct fission position, such that a remarkably improved angular resolution can be achieved. For the measurement of the mass and atomic number distribution of the fission fragments a highly-efficient, four-folded, Frisch-gridded twin-ionization chamber [16], used as Bragg ionization chamber (BIC) [17], is under development at MTA Atomki. The chamber will be equipped with double-sided Si strip (DSSD) detectors in order to measure α or light particle emission probability from the highly-deformed compound state and to detect any ternary particles from fission. An increased α decay probability would also be a conclusive evidence for the HD structure of the fissioning system. Atomic numbers will be extracted by tracking the Bragg curve of the ions using a desktop digitizer and advanced digital signal processing (DSP) techniques.

The actuality of the proposed project is best represented by the 2010 long range plan of the Nuclear Physics European Collaboration Committee (NuPECC), in which the investigation of the fission process, in particular the low-energy collective excitations of heavy nuclei and the fine structure of the fragment mass distributions are key issues to be focused on in the following years. On the other hand, the exploration of the fission barrier landscape of the light actinides has a number of important aspects beyond fundamental nuclear physics. Development of more efficient nuclear power plants (using the Thorium fuel cycle) requires the potential energy surfaces of major and minor actinides as inputs for cross-section calculations. Nuclear fission represents a breaking-point in the astrophysical *r*-process, which is controlled by the fission barrier of the heavy isotopes. The precise knowledge of the PES of these nuclei is thus, essential for the calculation of the heavy element abundances in the Universe, which is still one of the most compelling open problem in nuclear physics.

As day-one experiments, we propose to study the absolute cross-section and the angular distribution of the fission fragments in $^{232}$Th(γ,f) with the THGEM array, and to study the energy, mass, and atomic number distribution of the fragments that stem from the fission decay of the strongly deformed (presumably HD) states of $^{232}$Th with Bragg spectrometer and DSSD array.

In summary, studies of fission resonances at ELI-NP will benefit from the narrow bandwidth of the γ beam, which is in the range 12–18 keV in the region of interest. The γ probe excites well-defined states. There are a number of open questions related to the resonance cross-section, the resonance structure, etc., which can be addressed. The influence of the Pigmy resonance is not clear and that there is a large scattering of the data nowadays, which cannot be explained by neutron skin. The uncertainty in energy is also large. Mass and charge distribution of the resonances are not studied.

### 2.2 Rare fission modes, ternary fission

Information about ternary fission comes from neutron-induced and spontaneous fission experiments. Since ternary particles are released close to the scission point, they provide valuable information about the scission point and the fission dynamics itself.

Ternary photo-fission has never been studied. The distribution of α particles emitted in spontaneous ternary fission is displayed in Fig. 16 of Ref. [18]. Compared to neutron-induced or spontaneous fission experiments [19, 20], the use of polarized γ beam fixes the geometry of the process, which is an advantage for detail studies. Among the open problems related to the process are the mechanism of emission of ternary particles and the role of the deformation energy, the role of the spectroscopic factor, the formation of heavier clusters, to list a few.

The availability of brilliant γ beams at ELI-NP will make possible detailed studies of the angular distribution of ternary particles. As a day-one experiment, we propose to study the absolute cross section of ternary fission in the $^{238}$U(γ,f) reaction with the THGEM array.

In summary, the ternary particle is a unique probe of the nucleus at the scission point. Experiments at ELI-NP will provide first information about ternary photofission.

### 2.3 Yields in photofission

Neutron-rich isotopes at ISOL-type facilities are obtained by using fission reactions of actinide nuclei, induced by protons, neutrons or photons, or by spallation reactions. Neutron or low-energy proton induced fission techniques are used effectively as sources of exotic isotopes. They result in well-defined isotope production peaks and little isotope production outside these regions. Spontaneous fission is another source of neutron-rich isotopes and such a project is currently been realized at the Argonne National Laboratory (ANL) in USA. A 1 Ci $^{252}$Cf source is used [21], which has different yield distribution, compared to $^{238}$U. In Fig. 3, the yield distribution of neutron-rich nuclei, obtained with different reactions is shown. The figure illustrates the production cross-sections for a $^{238}$U beam at 1 A GeV impinging on hydrogen, deuterium, and lead targets [22]. In the case of $^{238}$U on Pb, photofission takes place due to the exchange of virtual photons, which excite the giant dipole resonance (GDR) of $^{238}$U. As a result, well defined light and heavy fragments are observed in the isotope yield distribution. Note that neutron-rich nuclei in the regions of the light and heavy fragments can be produced best in photofission.

Facilities, which explore photon-induced fission, use intense electron beams, which hit a convertor, producing bremsstrahlung with high enough energy to effectively excite the GDR of $^{238}$U. At ELI-NP we suggest to use the γ beam, which

is delivered by the gamma beam system (GBS) with energies that cover the GDR of $^{238}$U or $^{232}$Th.

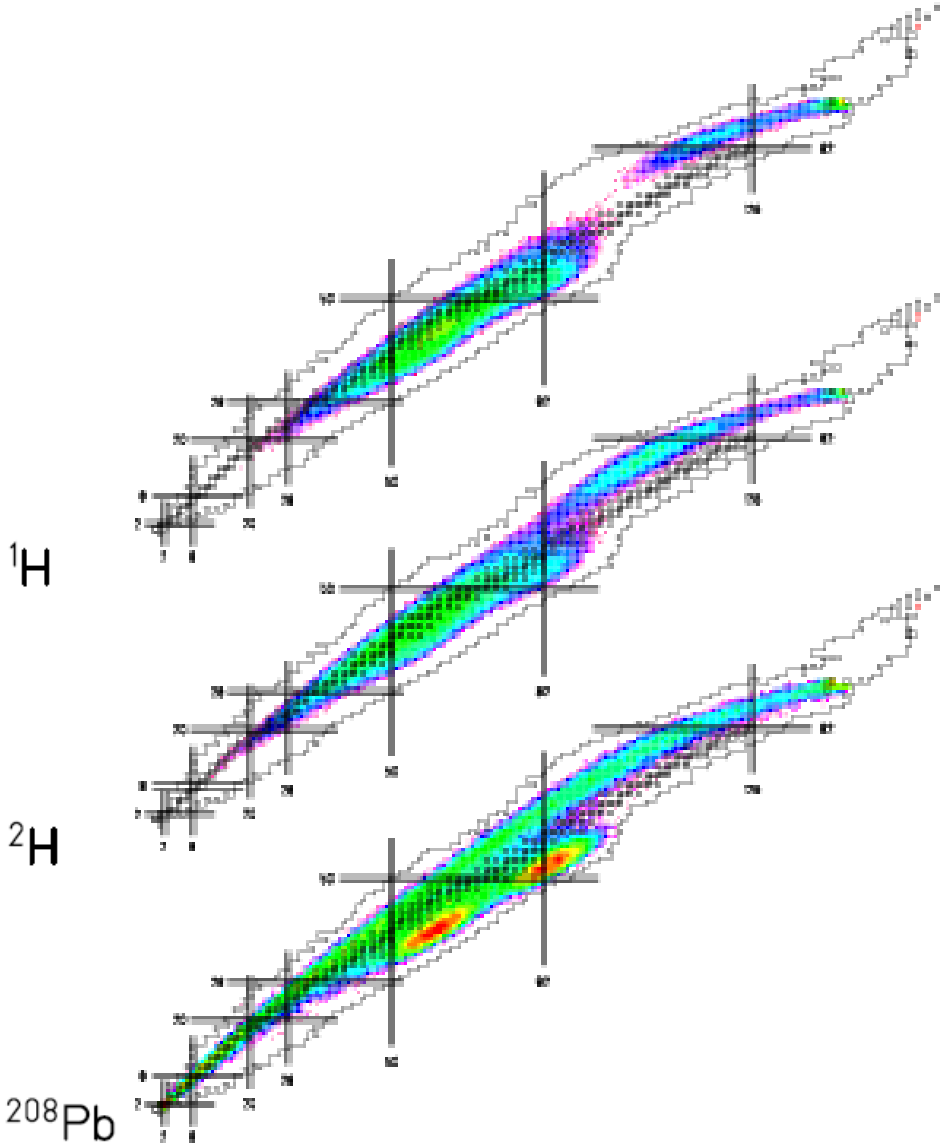


Fig. 3 − Production yields with $^{238}$U using different reactions [22]. Reproduced with permission from the American Physical Society.

A series of calculations aiming at a realistic estimate of the production yield at ELI-NP have been performed. The yields of exotic nuclei are calculated utilizing photofission with high-energy γ beams with energies in the range between 10 and 19.5 MeV, *e.g.* γ rays which overlap with the GDR of $^{238}$U, which is presented in Fig. 4 [23]. An advantage of ELI-NP with respect to bremsstrahlung facilities is that low-energy γ rays, which are inevitably present in the bremsstrahlung spectrum, can be cut with a collimator, because of the profile of the CBS γ beam at ELI-NP.

The ELI-NP γ beam will be sent on a $^{238}$U target of about 800 mg, which will be mounted in a gas cell, placed along the high-energy γ beam line of ELI-NP in the Gamma Source (GS) room, right after the high-energy interaction point where the γ beam has best emittance, as shown in Fig. 5. The γ beam is produced at the high-energy interaction point of the CBS, which is upstream behind the concrete wall, 7 m away from the gas cell. Before the entrance window of the gas cell a Pb collimator is mounted. The production target is mounted in a Cryogenic Stopping Cell (CSC). The CSC will be placed between the M27 deflection magnet and the M28 collimator, as shown in Fig. 5 where the components of the GBS layout are indicated with the prefix M. After collimation, the gamma beam at the CSC entrance will have energies in the range of 10–19.5 MeV, an intensity of about $5\cdot10^{10}$ γ/s (see Appendix A for details), and a spot size with the full width at half maximum (FWHM) of 5 mm. A realistic beam profile at the position of the target is presented in the right-hand side of Fig. 6. The beam source file, which was used in the simulations, was provided by the EuroGammaS consortium, which is the producer of the ELI-NP GBS.

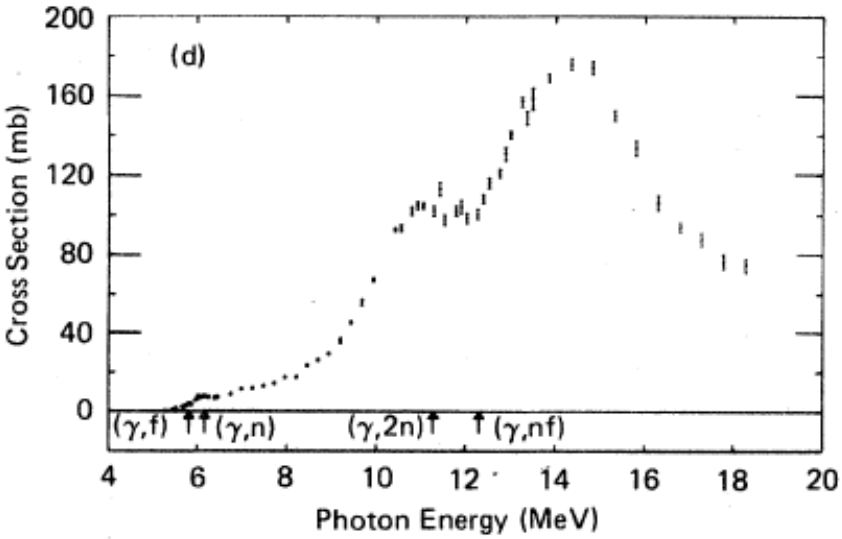


Fig. 4 − Photofission cross section for $^{238}$U [23]. Reproduced with permission from the American Physical Society.

Within these boundary conditions, benchmark calculations have been done. As a first step an 800 mg $^{238}$U cylinder of $\Phi$ = 4 mm diameter and a length of 3.33 mm was considered. In this geometry the whole quantity of $^{238}$U is overlapped effectively by the γ beam, which hits the target along the axis of the cylinder. The calculation should provide the total number of expected fission events. In addition, a gas cell, where the target is placed, was considered. It is filled with He gas at $T$ = 70 K with pressure $p$ of 300 mbar, resulting in a density of the He gas $\rho$ = 0.206 mg/cm$^2$, which is calculated through the relation:

$$\rho = A \cdot p / T \cdot R \tag{1}$$

where $A$ is the weight per mole of the gas and $R$ is the ideal gas constant.

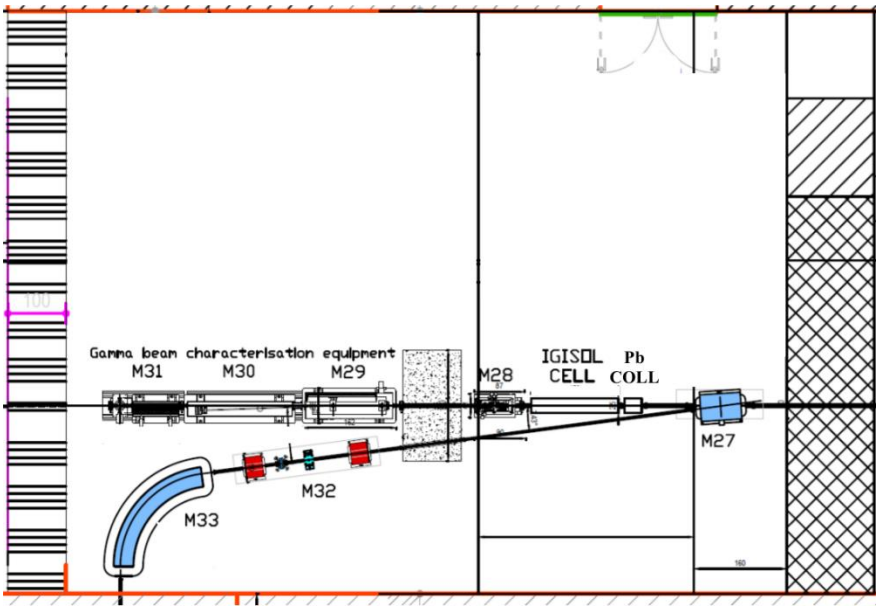


Fig. 5 − Layout of the Gamma Source Room of the ELI-NP experimental building. The IGISOL gas cell is indicated on the figure. A Pb collimator is placed upstream between the gas cell and M27 deflecting magnet [24].

Yield calculations have been performed using two independent GEANT4 applications, developed within the Photofission working group (WG) [25]. GEANT4 is a software for the simulation of the passage (GEometry ANd Tracking) of particles through matter. Each of them is not available in the standard GEANT4 implementation, and is inheriting from the G4HadronInelasticProcess class. The cross-sections are parameterized from [23], and for $E_\gamma$ = 5−7 MeV from Ref. [4]. The high-energy beam source file, provided by the EuroGammaS consortium,

contains $4.4 \cdot 10^6$ photons and is loaded by user defined classes inheriting from the G4VUserPrimaryGeneratorAction class.

The code, using one of the implementations, was validated in calculations of the photofission yield of the gas cell, which was proposed for the Accelerateur Lineaire et Tandem a Orsay (ALTO) facility in France. In this case, photofission in four $^{238}$U thin targets, placed in a gas cell, was considered. Fission was induced by bremsstrahlung, which was produced by the interaction between the 50 MeV electron beam and a W converter, placed at 5 mm away from the entrance window of the gas cell [26].

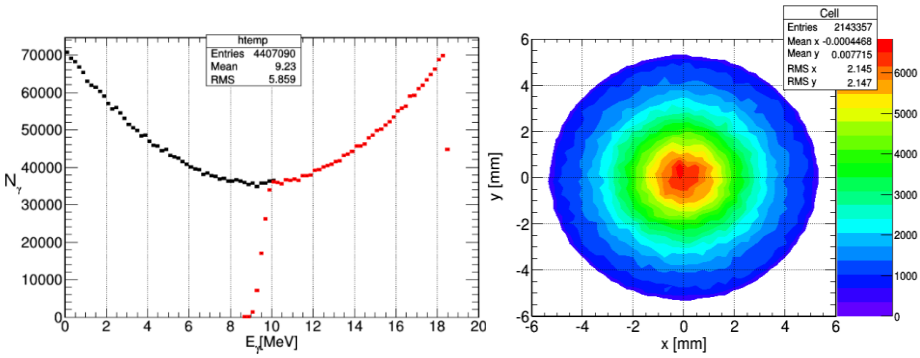


Fig. 6 − Left: The gamma-ray energy spectrum, the red dots correspond to the spectrum after collimation. Right: The collimated gamma beam spot at the CSC entrance window (FWHM ≈ 5mm).

The benchmark calculation for a bulk cylinder of 800 mg $^{238}$U, exposed to the high energy gamma beam with a rate of $5 \cdot 10^{10}$ γ/s, yields about $10^7$ f/s. The parameters of the ELI-NP γ beams, which were used in these calculations, are described in detail in Appendix A. It should be noted that only about 30% of γ beam photons interact with the 800 mg $^{238}$U target used in the simulations. Therefore, the above fission rate is a rather conservative estimate and can be expected for day-one experiments.

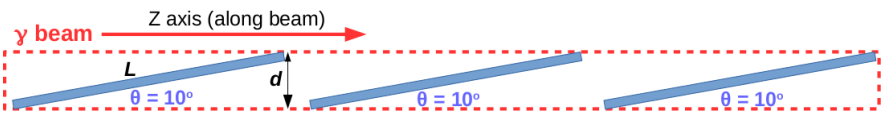


Fig. 7 − Target geometry for photofission yield simulations. Only three out of the 27 targets, which were used in the simulations, are shown.

The next step in the simulations is to consider a stack of thin $^{238}$U foils, with a total mass of 800 mg. The foils are tilted with respect to the beam axis at an angle θ = 10°, such that most of the ions produced in photofission, which leave one of the foils, do not hit the neighboring foils and, at the same time, the photon path through each foil is optimal. The transversal dimensions were chosen to cover the beam spot

FWHM, see right plot of Fig. 6, width $d$ = 5 mm and length $L = d/\sin(10^{o})$ = 29 mm. The target geometry is displayed in Fig. 7. Two values for the foil thickness are used in the calculations, namely 7 μm and 10 μm.

The energy spectrum, $N_{\gamma}(E_{\gamma})$, of the incident γ beam after the Pb collimation is presented in Fig. 8. The collimator acts as a filter for hardening the beam and effectively cuts the low-energy γ rays, such that in the spectrum of Fig. 8 they are only a tiny (about 0.3%) fraction. The number of γ rays selected by the collimator is about 46% of the γ rays that are produced at the high-energy interaction point. A fission rate, consistent with the above benchmark calculation, was obtained for this target configuration, too.

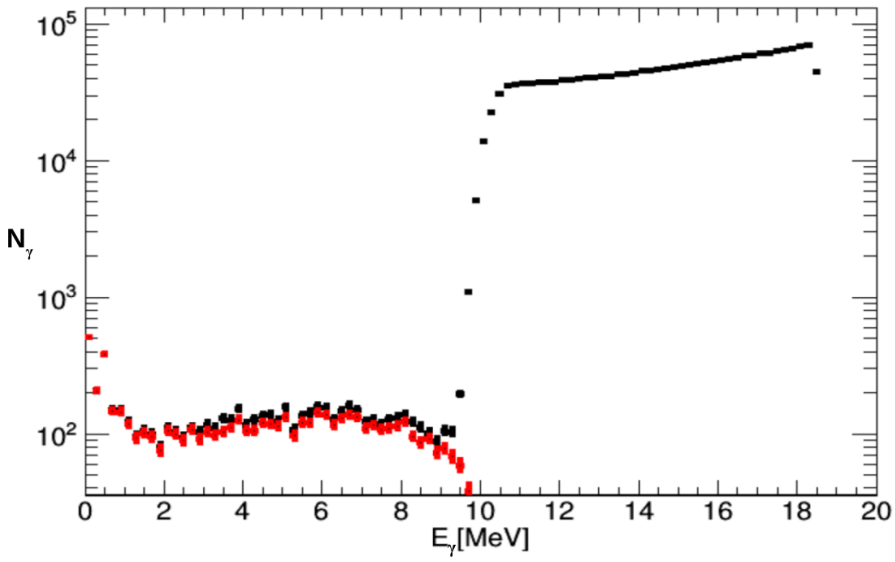


Fig. 8 − Energy spectrum of all incident γ-rays at the entrance of the CSC (black) and of incident γ rays at CSC entrance that do not come from the interaction point (red). The 10 MeV cut reflects the aperture used for the Pb collimator.

### 2.4 Structure of exotic neutron-rich nuclei

Different ISOL or in-flight facilities focus on multiple aspects of studies neutron-rich nuclei. A unique feature of ELI-NP is that the isotopes of interest can be produced in photon-induced fission, using a γ beam with optimized energy. Isotopes of refractory elements can be extracted effectively with the IGISOL method and, after mass and charge separation, send to different measurement stations. Isotopes of refractory elements, which are difficult or impossible to be studied at ISOL facilities where diffusion from a hot target is used, lie in the Ni region, in the

Zr-Mo-Rh region (light fragment) and in the rare-earth region (heavy fragment). Studies at ELI-NP will be focused on these isotopes.

Two deformed regions are known for neutron-rich nuclei, the Sr-Zr region and the heavy rare-earth neutron rich region. Present knowledge related to these nuclei comes from β-decay studies after thermal neutron ($n_{th}$) fission, in-beam γ-ray spectroscopy of fission fragments in spontaneous or $n_{th}$ fission and from in-flight experiments. At ELI-NP after photofission it will be possible to perform β-decay studies and mass measurements, in-beam γ-ray spectroscopy and, eventually in future, collinear laser spectroscopy. Mass measurements will be possible if a multi-reflection time-of-flight (MR-ToF) mass spectrometer is used to identify the extracted ions. All isotopes of one mass chain can be measured at the same time. Thus, their relative production yields and their masses will be determined simultaneously. Programs for measurements of masses, charge radii and ground-state nuclear moments of refractory isotopes exist at the other IGISOL facilities round the world, such as the IGISOL-4 facility at the Jyvaskyla accelerator laboratory (JYFL) in Finland, the Californium Rare Isotope Breeder Upgrade (CARIBU) facility at ANL in USA, and the Slow Radioactive Ion Beam (SLOWRI) facility, which is under construction at the Institute of Physical and Chemical Research (RIKEN) in Japan. The experiments at ELI-NP will compliment these programs, starting with detailed β-decay studies as day-one experiment.

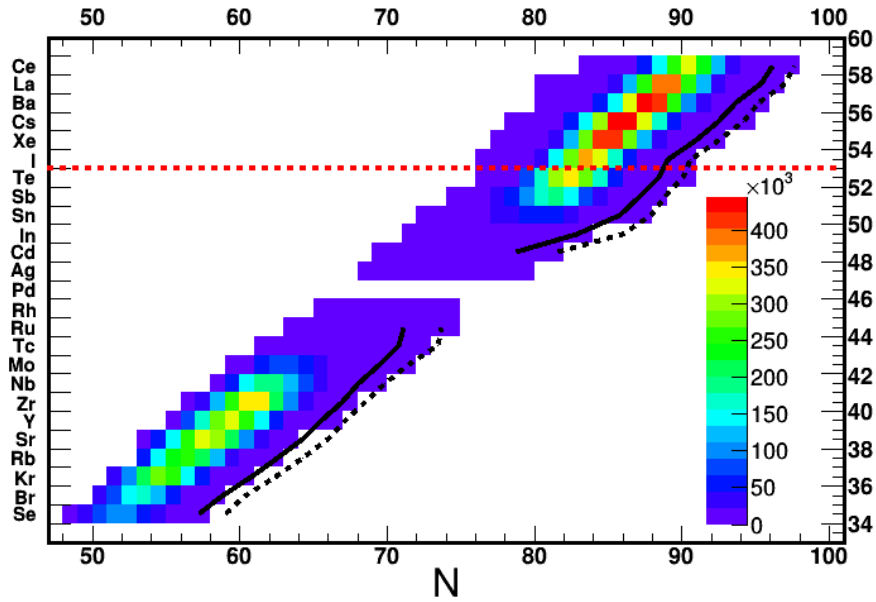


Fig. 9 − Estimated yield distribution in photofission at ELI-NP. The fission yields from [27] were scaled to a total of $10^7$ f/s and extrapolated to high *Z* elements. The dashed red line shows where the extrapolation begins. The solid lines show the 100 f/s limit and the dashed lines show the 1 f/s limit.

The fission yields in low-energy projectile fission of $^{238}$U on $^{208}$Pb were measured [27], a process which takes place via exchange of a virtual photon with energy $E_\gamma$ < 25 MeV. The photofission yield distribution at ELI-NP, presented in Fig. 9, was obtained using the photofission yield from Ref. [27], expressed in fragments per 100 fissions, which was scaled to a total of $10^7$ f/s. In the high $Z$ region (above the dashed red line in Fig. 9), the extrapolation procedure, detailed in Appendix B, was used to extend the yield estimation. The full lines in this figure show the 100 ions/s contours and the dashed lines show the 1 ion/s contours. For example, in order to scale the expected ELI-NP yields in comparison to the world leading facility, ISOLDE at CERN, by considering $10^7$ f/s, $^{128}$Cd will be produced at ELI-NP at a rate of about $10^2$ ion/s, which is an order of magnitude less, compared to what is possible nowadays at ISOLDE. Note that Cd is one of the elements, which are released best from the ISOLDE targets. As stated, the ELI-NP IGISOL facility will focus on studies of refractory elements, which are not easily extracted at an ISOL facility. Most of isotopes in the above-mentioned deformed regions are of refractory elements which opens an opportunity for an IGISOL experimental program at ELI-NP. These studies can address a number of key questions related to the nuclear structure in these regions. Among those could be mentioned *e.g.* the sudden onset of deformation in the $A$ ~ 100 mass region, the structure in the vicinity of the doubly-magic $^{132}$Sn, and the well deformed $A$ ~ 150 region.

Studies of ground-state properties of isotopes in the regions of interest will be possible at the IGISOL facility. For example, the suggested MR-ToF-MS provides the possibility for separation of millisecond isomers and for defining precisely isomeric ratios. The separated beam will be transported to a β-decay measurement station, where low-lying excited states of the isotopes of interest can be studied.

In-beam γ-ray spectroscopy has been done so far in spontaneous or $n_{th}$-fission. Such experiments were performed with the Gammashpere and Euroball spectrometers, using Cf sources, and with the EXOGAM spectrometer at ILL, Grenoble, using $n_{th}$ fission of $^{235}$U and $^{241}$Pu. Here we suggest measurements of the γ-decay of excited states using photofission of $^{232}$Th or $^{238}$U. Study of nuclear $g$-factors is a class of experiments, which is suggested for ELI-NP, and which is impossible with thermal neutrons. The importance of nuclear $g$-factor measurements is related to the fact that they provide information about the configuration of the isomer or the nuclear wave function. The physics, which will be addressed in these experiments, is related to the understanding of the deformed $A$ ~ 100 and $A$ ~ 150 mass regions.

**Onset of deformation in the *A* ~ 100 region:** The neutron-rich $A$ ~ 100 region features the fastest onset of deformation, right at $N$ = 60, ever observed [28] throughout the nuclear chart. The limits of this deformed region reach the Mo isotopes in the north. Some recent mass [29] and transition-probability measurements [30] in the Kr isotopes have shown that their deformation is gradually

increasing as a function of the neutron number. The Rb isotopes can be considered as the south border at which the sudden onset of deformation is observed.

An open question, that needs to be addressed, is which orbitals need to be occupied to achieve the onset of deformation in the Sr-Zr region. Nuclear moment measurements [31] have suggested two possible candidates for the ground state of $^{97}$Rb ($N$ = 60), namely the proton [431 3/2] and [301 3/2] Nilsson orbitals, without being capable to distinguish between them. A recent Coulomb excitation study from ISOLDE [32] identifies a rotational band built on the proton [431 3/2] orbital, clearly showing the importance of the proton part of the nuclear interaction in the onset of deformation. Urban *et al*. [33] suggested that the sudden onset of deformation comes from the interplay between the up-sloping and down-sloping neutron orbitals originating, respectively, from the spherical $g_{9/2}$ and $h_{11/2}$ orbitals.

The rubidium and strontium isotopes provide a perfect test ground for the proton- (odd-mass Rb isotopes), neutron- (odd-mass Sr isotopes) and the proton-neutron (odd-odd Rb isotopes) part of the interaction. Therefore their study can shed light on the interplay of the proton-neutron interaction involved in the development of deformation in this region. For the neutron-rich Zr, Nb and Mo isotopes, the onset of deformation and the influence of triaxiality at $N$ = 60 in the middle of the region of the deformed region can be studied.

*Table 1*

Selected nanosecond isomeric states in the $A$ ~ 100 mass region.

| Isomer | $I^{\pi}$ | $E_x$ [keV] | $T_{1/2}$ [ns] |
|---|---|---|---|
| $^{93}$Rb | $27/2^-$ | 4423 | 111 |
| $^{94}$Rb | $10^-$ | 2075 | 107 |
| $^{95}$Rb | $9/2^+$ | 810 | 95 |
| $^{96}$Rb | $10^-$ | 1135 | 2000 |
| $^{95}$Sr | $7/2^+$ | 556 | 22 |
| $^{97}$Sr | $7/2^+$ | 308 | 169 |
| $^{97}$Zr | $7/2^+$ | 1264 | 103 |
| $^{99}$Zr | $7/2^+$ | 252 | 293 |
| $^{99}$Zr | $9/2^+$ | 1038 | 54 |

While longer-lived isotopes can be identified and separated with the MR-ToF-MS, and isobarically pure beams can be delivered for β-decay studies, the *g*-factors of the shorter-lived isomers can be studied via in-beam γ-ray spectroscopy, using the ELI-NP Advanced γ-ray Detector (ELIADE) array, which is described within the GBS TDR1 “Nuclear Resonance Fluorescence Experiments at ELI-NP”. A number of short-lived isomeric states have been identified in the region (see Table 1). They all can be studied in photofission at ELI-NP within the frame of the present project.

**Vicinity of doubly-magic $^{132}$Sn:** The region in the vicinity of the neutron-rich $^{132}$Sn is of particular interest due to the double-shell closures at $Z = 50$ and $N = 82$. The nuclei from the Sn isotopic chain are governed by neutron-hole excitations involving $\upsilon h_{11/2}$, $g_{7/2}$, $d_{3/2}$, $d_{5/2}$, and $s_{1/2}$ orbitals. Isomeric states in these isotopes are built from the unique parity $\upsilon h_{11/2}$ orbital which is close to the Fermi surface with pure or mixed configurations coming from neutrons that scatter to the close-lying *g*, *d*, *s* orbitals.

In this region only few *g*-factors are known up to date (see those marked with asterisks in Table 2) that can be used as testing cases for the present studies. Furthermore, $^{131}$Sn and $^{133}$Sb being respectively just a neutron and a proton away from $^{132}$Sn will provide an essential information on the p-n coupling, shell quenching effects [34] etc. In $^{131}$Sn a sub-microsecond isomer has been observed and suggested as $21/2^-$ [35] or as $23/2^-$ [36], built on the $\upsilon f_{7/2} h_{11/2}^{-2}$ configuration. A *g*-factor measurement of this isomer would provide firm spin assignment and more information on its configuration. Studies of the isomers in the region would probe the influence of an odd-nucleon to the double-magic core and shed light on core-coupled excitations sensitive to the composition of the core itself [37].

*Table 2*

Selected nanosecond isomeric states in the vicinity of $^{132}$Sn. Isomers marked with asterisks have known *g*-factors and can be used as test cases.

| Isomer | $I^\pi$ | $E_x$ [keV] | $T_{1/2}$ [ns] |
|---|---|---|---|
| $^{130}$Sn | $5^-$ | 2084 | 52 |
| $^{131}$Sn | $23/2^-$ | 4605 | 300 |
| $^{132}$Sn | $6^+$ | 4716 | 20 |
| $^{131}$Sb | $23/2^+$ | 2166 | 1100 |
| $^{132}$Sb | $6^-$ | 254 | 102 |
| $^{132}$Te* | $6^+$ | 1775 | 145 |
| $^{133}$Te | $19/2^-$ | 1610 | 100 |
| $^{134}$Te* | $6^+$ | 1691 | 164 |
| $^{135}$Te* | $19/2^-$ | 1554 | 511 |

**Spin-orientation in photofission:** A major requirement for nuclear moment studies of isomeric or short-lived excited nuclear states is to obtain a spin-oriented ensemble of states. Provided that this could be achieved through the production mechanism itself a significant simplification of the applied techniques could be obtained. The other option, in the case when the nuclear spin ensemble is isotropic in space, is to look for gamma-gamma angular correlations. The difficulties in the second approach are: (i) a high-efficiency gamma-ray detection setup, with detectors placed at specific angles, is needed; and (ii) the background level increases significantly with the increase of the lifetime of the state of interest.

For the preparation for nuclear moment studies of isomeric and short-lived excited states in photofission we looked for existing data on the γ-ray angular distribution in photofission. To the best of our knowledge no such data is available. However, the angular distribution of fission fragments, following gamma-ray induced fission of different targets, has been well studied (see for e.g. Ref. [38, 39] and the references there in). The angular distribution of fission fragments, assuming they are emitted along symmetry axis depends on the probability distribution of the symmetry axis. In the absence of polarization in the incident beam and assuming only electric and quadrupole photofission, the fragments angular distribution is of the form:

$$W(\theta) = a+b\sin^2\theta+c\sin^2 2\theta. \quad (2)$$

And in the case of linearly polarized $\gamma$-ray beams, the angular distribution of the fission fragments is of the form:

$$W(\theta) = a+b\sin^2\theta+c\sin^2 2\theta+P_\gamma\cos(2\varphi)(b\sin^2\theta+c\sin^2 2\theta), \quad (3)$$

where $P_\gamma$ is the fractional beam polarization [38]. In this case, the fragment angular distribution is found to be strongly dependent on the azimuthal angle, $\varphi$. The $b$ values are extracted by Mueller *et al.* from a photofission experiment at the HI$\gamma$S facility [30] and are shown in Fig. 10. The obtained $b$ values are measured through the angular distribution of the prompt neutrons, as the asymmetries in the distribution of prompt neutrons are correlated with the distribution of fission fragments [38]. This

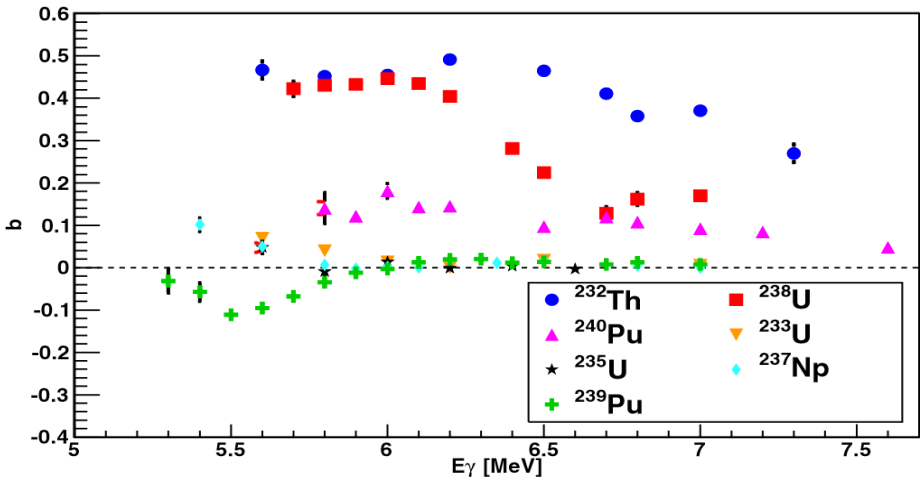


Fig. 10 − Angular distribution of fission fragments in photofission presented in the form of Eq. 3 and the normalization is of the type $a + b = 1$. Reproduced with permission from the American Physical Society.

is due to the fact that the neutrons, which are emitted primarily from the fully accelerated fragments, have spatial distribution along the direction of motion of the fragments. They do not emerge randomly from the nucleus. On the basis of this, an asymmetry can be expected in the angular distribution of gamma-rays emitted by fission fragments. This effect will be studied in detail at ELI-NP.

The measurement of fragment angular distribution using bremsstrahlung is presented in Fig. 11. The general understanding of these results is that this is a process, located in a narrow energy window just above the fission barrier, and the asymmetry is gradually decreasing with the increase of the incident γ-ray energy. The observed anisotropic dipole photofission dominates in $^{232}$Th until 6.5 MeV and until approximately 6 MeV for $^{238}$U. Photofission fragments of odd-*A* actinides show much more isotropic angular distributions. The high polarization of the ELI-NP *γ* beam provides an opportunity for such studies.

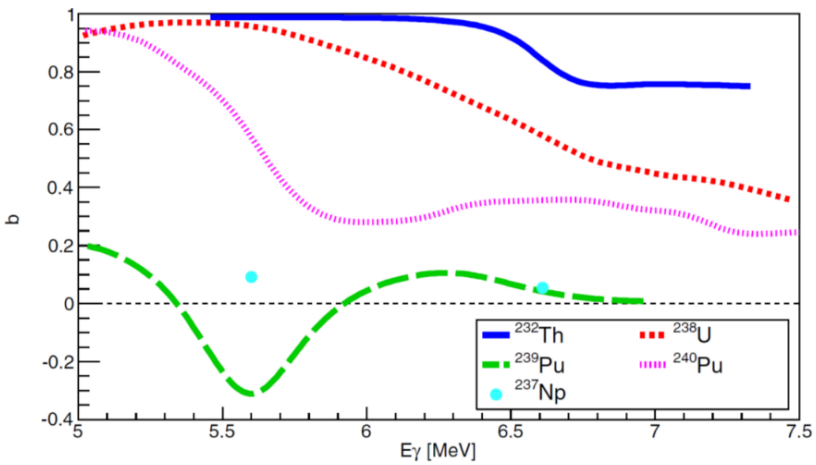


Fig. 11 − Angular distribution of fission fragments in photofission presented in the form of Eq. 2 and the normalization is of the type $a + b = 1$. The data for $^{232}$Th, $^{238}$U and $^{240}$Pu are from [40] and the figure is from [38]. Reproduced with permission from the American Physical Society.

Detailed measurements of the fission asymmetry will be possible within the experimental program defined in Sections 2.1 and 2.2. Asymmetries in the angular distribution of gamma-rays, with respect to the emitted fission product, have been observed [41] for the case spontaneous fission of $^{252}$Cf. Therefore, it can be expected that significant asymmetry in the angular distribution of gamma-rays could be observed as well in the case of photofission, in the conditions in which asymmetries in the fission products have been observed.

Next to the studies of nuclear *g*-factors, which will benefit from the space asymmetry of the angular distribution of the fission fragments, detailed measurements of the fission asymmetry will be possible within the experimental program defined in Sections 2.1 and 2.2.

The angular momentum of γ-rays emitted from the de-excitation of fission fragments during spontaneous fission of $^{252}$Cf [41] is linked with the magnitude and alignment of the primary angular momentum of the fragments. It has been observed that the angular distribution of most of the $\gamma$-rays were found to be consistent with the assumption of complete alignment of primary angular momentum of the fragments perpendicular to the fission direction. Therefore, it can be expected that significant asymmetry in the angular distribution of $\gamma$-rays could be observed as well in the case of photofission in the conditions in which asymmetries in the fission products have been observed. The secondary fragments would be detected with their mass and atomic number distribution and $\gamma$-rays from them would be identified imposing time coincidence requirement.

## 3. TECHNICAL PROPOSAL

### 3.1 High Efficiency Bragg Ionization Chamber and Si DSSD Detector System (ELI-BIC)

Gaseous ionization chambers are ideal devices to measure the total kinetic energy (TKE) of the fission fragments with high resolution and large solid angle when compared to solid state detectors [16]. The measurement of fragment kinetic energies allows the fragment mass distribution to be deduced using the 2E technique [16]. Moreover, the so-called cold fission events, where the fragments are in the ground state, can be selected by setting a proper lower limit on the total kinetic energy (TKE). A multi-target, Frisch-gridded, twin ionization chamber will be constructed by improving the concept of an existing design, which was originally developed for neutron-induced fission experiments.

The prototype design (Fig. 12) is based on a twin gridded ionization chamber. It consists of two parallel plate ionization chambers with Frisch grids and a common cathode. The grid is a mesh made of parallel steel wires, 0.1 mm in diameter, spaced by 1mm, mounted on annular disks with inner diameter of 9 cm.

The anodes and the cathode are circular plates with a 12 cm diameter. The cathode is made from two disks, 0.5 cm thick, with circular holes of 4 cm diameter at the centers. The fissile sample supported by a thin $^{12}$C backing is mounted between the disks. The distance between the cathode and the grid should be long enough to stop all the fission fragments in the detector gas before they reach the grid. The chamber plates are mounted on isolating Teflon rods inside a cylindrical stainless steel tank of 13.5 cm height and 18 cm diameter. The chamber is operated as a gas-flow chamber using a mixture of 90% Ar + 10% $CH_4$ at gas pressure of $p$ = 1 bar. Frisch-gridded, twin-ionization chambers permit simultaneous measurements of the TKE and the emission angles of both fission fragments in coincidence. The energy of the fragment is determined from the anode pulse height, while the sum of the grid

and anode signals is used to deduce the fragment emission angle with respect to the symmetry axis of the chamber. Thus, a precise angle-dependent energy loss correction can be performed. For the proposed multi-target detector layout, four small area (1 $cm^2$) thin (200−300 $\mu g/cm^2$) actinide targets will be placed into the center of each cathode to increase the effective target thickness, and thus the fission yield of the (γ,f) reaction at deep sub-barrier energies.

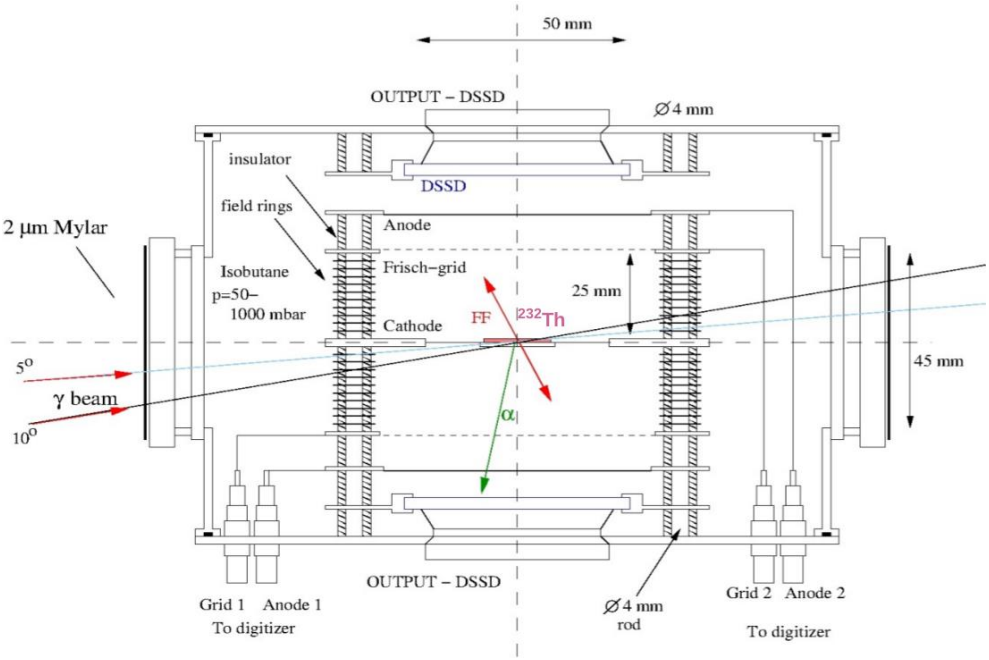


Fig. 12 − Prototype design of a Frisch-gridded twin ionization chamber equipped with DSSD detectors.

The chamber is a versatile tool which allows measurements of mass distribution of the fission fragments induced by brilliant γ beams on Th, U and other actinide isotopes. Due to its capability of determining the specific ionization of the different ions and the localization of their traces, by using digitizers and digital signal processing (DSP) techniques, the chamber can provide also information about charge distribution of the fission fragments. In order to increase the capability of the chamber to detect also the process of nuclear fission accompanied by emission of light charge particles (LCP) *ΔE-E* telescopes will be placed inside the chamber in a transversal position between the electrodes.

The first test experiment of the prototype ionization chamber was performed in November 2013 at MTA Atomki using a $^{252}$Cf fission source. The experiment was devoted to acquire knowledge on the digital signal processing of fission events, in particular, extracting atomic number related information of the signal. A typical

digitalized signal of a charged sensitive preamplifier signal of a fission event is shown in Fig. 13 before signal shape transformations and recorded with a CAEN 5740 62.5 MS/s desktop digitizer [42].

The correlation of the kinetic energy and emission angles of the fission fragments using the $^{252}$Cf source, is shown in Fig. 14. The correlation of the mass and charge of the fission fragments using the $^{252}$Cf source, is shown in Fig. 15.

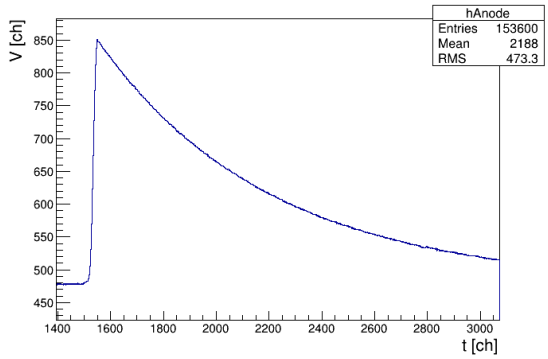


Fig. 13 − Digitized preamplifier signal of a fission fragment.

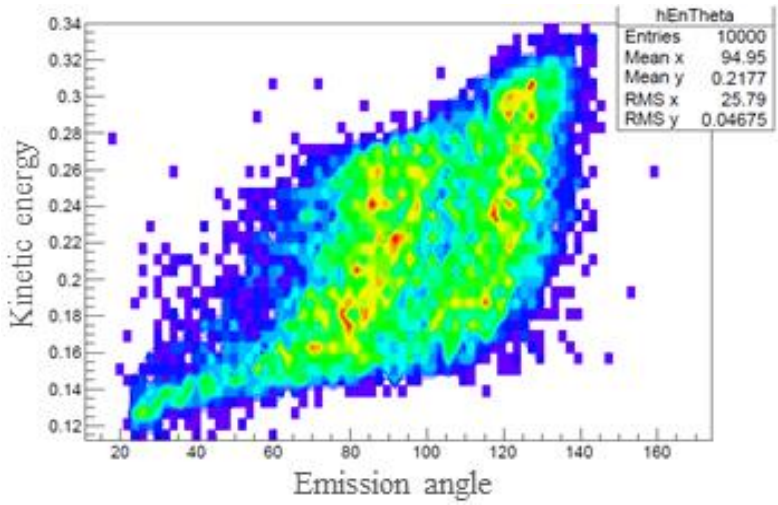


Fig. 14 − Correlation of the experimental kinetic energy and emission angles of fission fragments.

The figure shows the present success of the chamber in measuring the atomic number of the fragments without any field electrodes, proper pre-amplifiers and a proper digitizer. At present the MTA Atomki group is working on increasing the resolving power for *Z*. Due to advanced DSP filtering, the kinetic energy of the fragments can be determined with higher precision compared to previous

measurements (Fig. 14). For the in-beam experiments at ELI-NP, a possible solution is to use CAEN A1422 90 mV/MeV 4 channel F2 type (200 pF) preamplifier [42] with CAEN DT5730, 8 channel, 500 MS/s, 14 bit digitizer [42].

The performance of the BIC is currently been tested at MTA-Atomki, with a one-sided $^{252}$Cf source, for optimizing the high voltages of the anode, grid and field rings (the BIC is "one sided" as well). The effect of the field rings, which now have been implemented in the chamber, is being tracked. Fig. 16 shows from the top, the

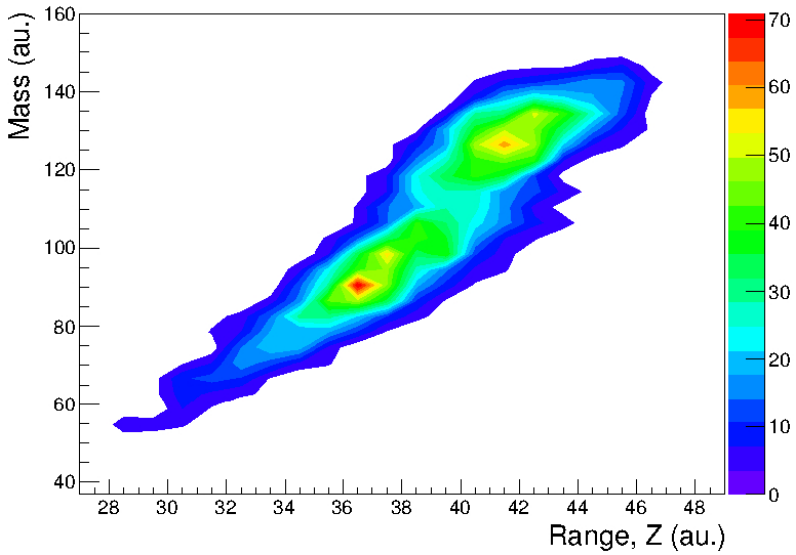


Fig. 15 − Experimental correlation of the mass and charge of the fission fragments.

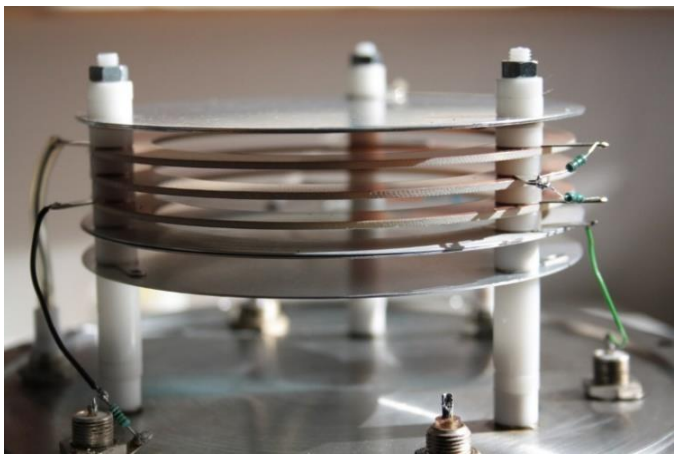

Fig. 16 − Photograph of the one-sided BIC used for the present test measurements.

cathode (with $^{252}$Cf), 3 field rings (with spacers of 4.5 mm), Frisch-grid, and the anode at the bottom. The same layers are used for the other side of the cathode, which were removed at the time of the testing. The 10 MΩ voltage dividers can also be seen in the figure. These are grounded via the detector chamber through a 10 MΩ resistor (can be seen in the left side of the figure). Spacers and screws were made of Polyoxymethylene (POM).

After the $^{252}$Cf source tests, the BIC will be tested with neutron beam and $^{232}$Th target. Test experiments will be performed at the cyclotron laboratory of MTA Atomki, using a Be target and deuteron beam (thermalizing the neutrons), and at the Budapest Neutron Center.

For transmission resonance experiments with the Bragg ionization chamber in the E8 experimental hall of ELI-NP, we have carried out GEANT4 simulations to estimate the size of the effective gamma beam spot at the target position. The target is considered to be positioned at 30 m from the interaction point (IP), the production point of the gamma beam, and the ELI-NP collimator (M28 in Fig. 5) is at 890 cm from the interaction point (IP). A detailed description of the ELI-NP collimator is given in GBS TDR2 "Gamma Above Neutron Threshold Experiments at ELI-NP" (GANT) and in Ref. [24]. The simulations have been carried out using the 5.8 MeV gamma beam source file provided by the EuroGammaS consortium. We have used the bandwidths (BW) of 0.3%, for 1.5 mm collimator slit aperture, and 0.5%, for 2.5 mm collimator slit aperture, according to the delivery specifications of the γ beam. The results of the simulations are listed in Table 3. The target dimensions, mentioned in the table, are calculated considering a 10° tilt of the target with respect to the beam direction. A typical beam spot at the target position for 0.3% bandwidth, obtained from this simulation, is shown in Fig. 17. Note that the beam spot at the target position is an ellipse, with a short axis defined by the diameter of the beam spot and a long axis defined by the tilt angle along with beam spot diameter.

The double Bragg spectrometer will be coupled to DSSD detectors. An example of such detector is shown in Fig. 18.

*Table 3*

Estimated beam spot diameter ($\Phi$) and the required target dimensions (TD) to be used for the study of transmission resonances in the Bragg ionization chamber. The 5.8 MeV gamma beam source file has been used with 0.3% and 0.5% bandwidths.

| Beam BW | Collimator Slit Aperture (mm) | For 95% of the beam | | For 90% of the beam | |
|---|---|---|---|---|---|
| | | $\Phi$ (mm)[a] | TD (mm)[b] | $\Phi$ (mm)[a] | TD (mm)[b] |
| 0.3% | 1.5 | 4.77 | 4.77, 27.47 | 4.62 | 4.62, 26.61 |
| 0.5% | 2.5 | 7.85 | 7.85, 45.21 | 7.55 | 7.55, 43.48 |

[a] $\Phi$: Beam diameter at the experimental point

[b] TD: required Target dimension ($x$,$y$) for 10° tilt with respect to the beam direction

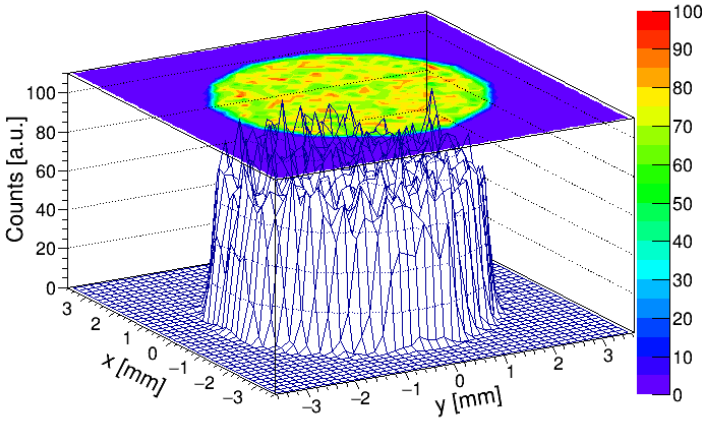


Fig. 17 − Beam spot at the target position for transmission resonance experiments with the Bragg chamber.

Fig. 18 − An image of a double-sided silicon strip detector.

The possible synergy with the DSSD detectors, which are considered within the GBS TDR4 "Charge Particle Detection at ELI-NP" (CPD) experiments, has been studied. In photodisintegration reactions of astrophysical relevance, particles can be emitted with energies as low as few hundred keV, due to the comparatively low photon energies in stars, of the order of about 10 MeV during the latest stages of stellar evolution (pre supernova conditions). Such energies are slightly larger than particle emission thresholds, thus a close link with nuclear structure considerations and nuclear spectroscopy is apparent. Under these conditions, no $\Delta E$ detectors can be used for particle ID, unless an untenable detection threshold is introduced,

strongly limiting our access to the relevant energy interval. Pulse shape analysis (PSA) has proved not applicable yet at such energies while time-of-flight measurement would imply a very large detector, entailing very high costs to guarantee the necessary high energy and angular resolution, which are especially important for nuclear spectroscopy. Therefore, particle identification will be performed by means of full reconstruction of reaction kinematics. Thanks to the high energy and angular resolution (about 0.5% and 0.2%, respectively) and the broad angular coverage, the kinematics of the different reactions can disentangled and, consequently, the signal can be separated from background processes, if present.

Since few particles are emitted per reaction event, low granularity is necessary, allowing us to keep the number of electronic channels comparatively low by using charge partition position sensitive detectors. It is important to underscore that no digitalization of the signal is necessary, since PSA is not viable, so a small data flow will be produced as few detectors will be fired. On the other hand, the request of high resolution implies the usage of suitable electronics; for instance, standard analog electronics would perfectly match the required resolution standards still being a viable solution thanks to the total number of channels necessary, *e.g.* about 300. Regarding radioprotection issues, no significant radioactivity is produced since ($\gamma$,$\alpha$) and ($\gamma$,p) reactions are mostly studied. This allows us to replace targets and study different photo-dissociation reaction in the measurement campaign.

In the case of photofission reactions, the physical conditions are quite different, requiring a different approach. First of all, photofission processes involve the emission of many energetic particles. This implies the necessity of accurate particle identification and a reasonable granularity to prevent multiple hits. This can be achieved by using double-sided silicon strip detectors coupled with PSA. No kinematic identification would be possible as a large number of particles is emitted and because of the different physics leading to the fragment production, such as secondary emission of particles and in-flight decay. The large number of electronic channels, about 300, requested by double-sided silicon strip detectors makes it necessary the use of Application Specific Integrated Circuit (ASIC) electronics, while the digitalization of signals from each strip would produce a large data output, calling for a dedicated high-speed acquisition system. DSSD detectors would guarantee the requested energy and angular resolution. Regarding radioprotection issues, the study of photofission on actinide (usually radioactive) targets cannot avoid contaminating the detectors with fission fragments and maybe even with long-lifetime actinides. Therefore a dedicated detector setup is necessary, besides the previous consideration based on the different physics to be investigated, which will be used only for this purpose. For radiation safety reasons a dedicated laboratory might be necessary to manipulate the detectors and the other irradiated materials.

To measure the kinetic energy and angular distributions of the fission fragments (with isotope identifications) and to identify the ternary particles with measuring their energy and angular distributions, we propose an array of four Frisch-

gridded ionization chambers with DSSD detectors. The proposed multi-target detector layout, using four actinide 200−300 μg/cm$^2$ thin targets tilted at a 10° angle with respect to the γ beam with dimensions 0.5 × 4 cm$^2$, to get 90% of the beam, which will be placed in the center of each cathode. Such a multi-target setup results in an increase of the effective target thickness, and thus the fission yield of the (γ,f) reaction at deep sub-barrier energies. The setup will be optimized to use beams of 0.3% bandwidth, which will result in using smaller targets and will lead to an improvement of the energy and angular resolution of the experiments. The setup includes four double-armed Bragg spectrometers with digital read-out. The cathode is segmented to provide particle identification of the ternary particle. Eight DSSDs are coupled to each ionization chamber to detect ternary particles.

This setup will be used in two types of experiments: (i) studies of the properties of the fission fragments (angular, energy, mass and charge distributions) on/off the fission resonances, and (ii) identification of the ternary fission particles and study their correlation with the properties of the fission fragments defined above.

The setup will be mounted in experimental area E8 of the ELI-NP laboratory building or, if possible, in E7, as close as possible to the interaction point, to take advantage to the ELI-NP pencil beams. The BICs will be mounted in a common reaction chamber placed on a platform, which will be aligned along the beam using the ELI-NP laser tracking system.

### 3.2 Thick Gas Electron Multiplier based Detector System (ELITHGEM)

For the fission-fragment angular distribution measurements, a multi-target detector array will be developed, consisting of position sensitive gas detector modules based on the state-of-the-art THGEM technology [15]. THGEM is a robust, simple to manufacture, high-gain, gaseous electron multiplier. Its operation is based on gas multiplication within small, submillimeter to millimeter diameter holes drilled in standard double-face Cu-clad printed circuit boards (PCB). The entire structure of the THGEM together with a segmented readout electrode provides a true pixelated radiation localization. The electron multiplication of the THGEM is based on the large potential difference between the two sides of the board resulting in a strong dipole field within the holes. Electrons, deposited by ionizing radiation in a conversion region above the THGEM, are focused into the holes by the dispersed electric field. Then the electrons are multiplied within the holes under the high electric field (25–50 kV/cm). A small fraction of the resulting avalanche electrons are collected on a bottom electrode, while the significant part is transferred to a collecting anode or to a second multiplier element. Each hole acts as an independent multiplier. This leads to high-gain operation in a large variety of gases about a multiplication factor of about $10^4$. At the low-pressure operation mode, the signals are exceptionally fast, having a rise time of $\tau_R \approx 3$–4 ns. With the standard design

(1 mm holes pitch), a position resolution of 2 mm can be achieved by using segmented anode planes with 1−2 mm wide anode pads.

In the proposed design, the detector covers almost a full solid angle (around 80% of 4π) and has an angular resolution of about 5°. The background sensitivity and the radiation damage are negligible; however, the extremely low counting rates in photofission experiments at deep sub-barrier energies require sufficient α particle discrimination. This goal can be achieved by the coincident detection of both fission fragments. It has to be emphasized that the foreseen unprecedented sub-millimeter γ beam spot size allows the development of considerably more compact photofission detectors than those of before when only bremsstrahlung γ sources were available with a beam spot diameter of 4–5 cm. The well-focused γ beam also defines a distinct fission position, so a remarkably improved angular resolution can be achieved compared to previous bremsstrahlung photofission experiments.

A prototype THGEM unit, consisted of a THGEM board manufactured at CERN (Fig. 19), a transmission mesh, and a segmented, delay-line readout anode (Fig. 20), has been designed and constructed recently at MTA Atomki. Fig. 21 shows a picture of the THGEM 4π prototype unit.

The testing of the prototype unit has been performed with a $^{252}$Cf fission source. Typical preamplifier output signals (same event, two ends of a delay line) are shown in Fig. 22, together with a one-dimensional position spectrum (Fig. 23).

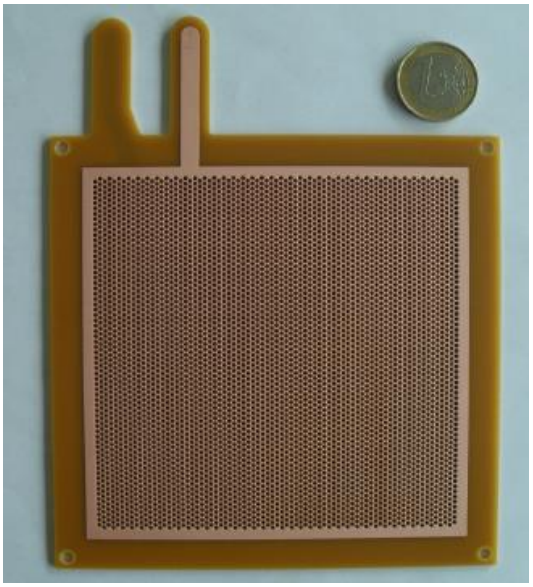

Fig. 19 − A 10 × 10 cm$^2$ THGEM board, designed and manufactured at CERN.

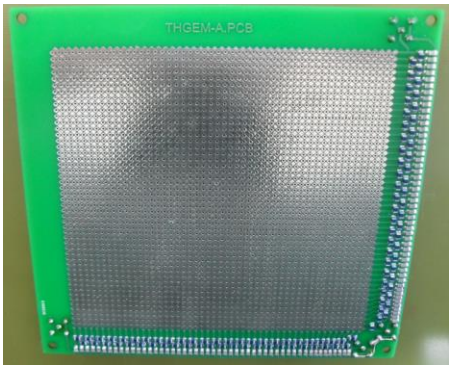


Fig. 20 − The prototype of a segmented anode board of delay-time readout type.

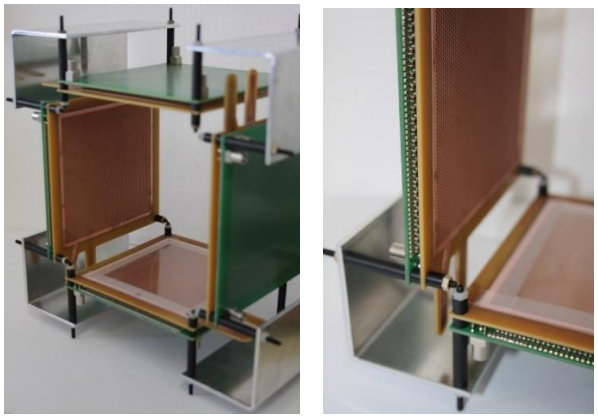

Fig. 21 − Picture of the THGEM 4π prototype unit.

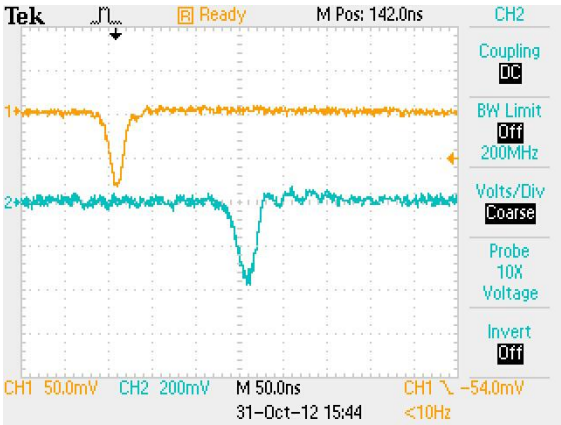


Fig. 22 − Preamplifier output signals of a detected fission fragment at the two ends of the delay line.

To determine the absolute intrinsic efficiency of the detectors, one has to involve a pair of detectors having the same geometry. By using a thin actinide target and charged particle beams with beam energy over the fission threshold the efficiency can be deduced by counting the single and coincidence events. Such a test experiment will be performed at the cyclotron laboratory of MTA Atomki.

Fig. 24 presents the result of the measurement by using the fission fragment source, $^{252}$Cf. One layer of THGEM board, equipped with a delay-line readout anode

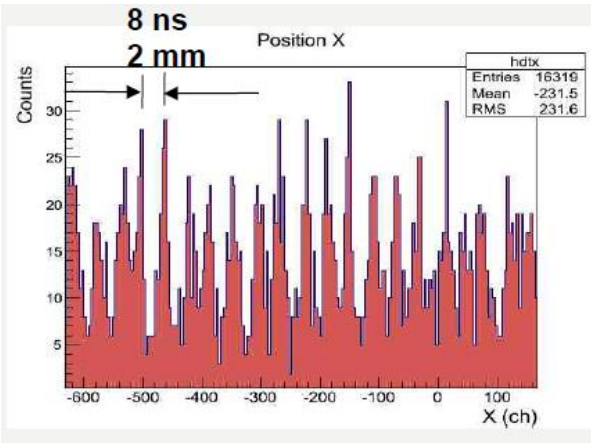


Fig. 23 − One-dimensional position spectrum of fission fragments.

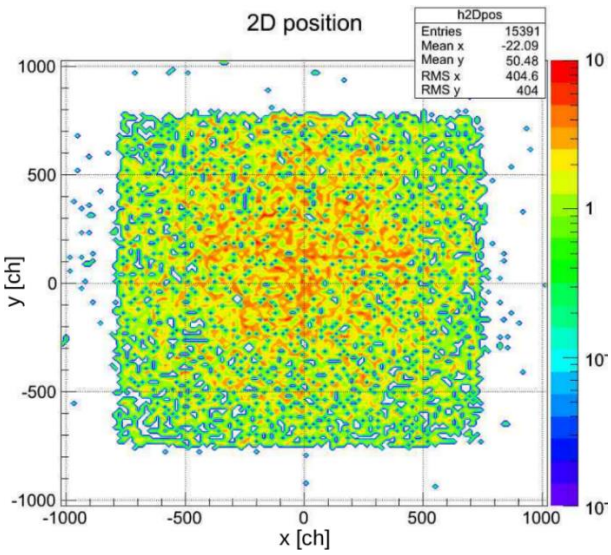


Fig. 24 − A 2D isotopic distribution of the fission fragments from the point source, with one layer of THGEM board equipped with a delay line read out anode.

is used. The histogram shows the isotropic distribution of the fission fragments from the point source.

For experiments in the GDR range with the ELITHGEM array in the E8 experimental hall of ELI-NP, we have carried out simulations to estimate the size of the effective gamma beam spot at the target position (30 m from the IP). The simulations have been carried out using the 12.9 MeV and 18.5 MeV γ beam sources, which were obtained from the EuroGammaS consortium. Bandwidths of 0.3% and 0.5% have been used. The results of the simulations are presented in Table 4. The target dimensions mentioned in the table are calculated considering a 45° tilt of the target with respect to the beam direction. Typical beam spots for the 12.9 MeV and 18.5 MeV gamma sources with 0.5% bandwidth, obtained from this simulation, are shown in Fig. 25.

A possible realization of the array, consisting of 12 THGEM detector units to cover full solid angle is shown in Fig. 26. Ten fissile targets are placed along the axis. The setup provides a modular (extendable) structure.

*Table 4*

Estimated beam spot radius (*R*) and the required target dimensions (TD) for GDR study using the THGEM array. The 12.9 and 18.5 MeV γ beam sources have been used with 0.3% and 0.5% bandwidths.

| Gamma source used | Beam BW | Collimator Slit Aperture (mm) | For 95% of the beam | | For 90% of the beam | |
|---|---|---|---|---|---|---|
| | | | $\Phi$ (mm)[a] | TD (mm) [b] | $\Phi$ (mm)[a] | TD (mm) [b] |
| 12.9 MeV | 0.3% | 0.5 | 1.60 | 1.60, 2.26 | 1.54 | 1.54, 2.18 |
| | 0.5% | 1.5 | 4.77 | 4.77, 6.74 | 4.62 | 4.62, 6.53 |
| 18.5 MeV | 0.3% | 0.5 | 1.60 | 1.60, 2.26 | 1.55 | 1.55, 2.19 |
| | 0.5% | 1.3 | 4.12 | 4.12, 5.82 | 4.00 | 4.00, 5.66 |

[a] $\Phi$: Beam diameter at the experimental point

[b] TD: required Target dimension (*x*,*y*) for 10° tilt with respect to the beam direction

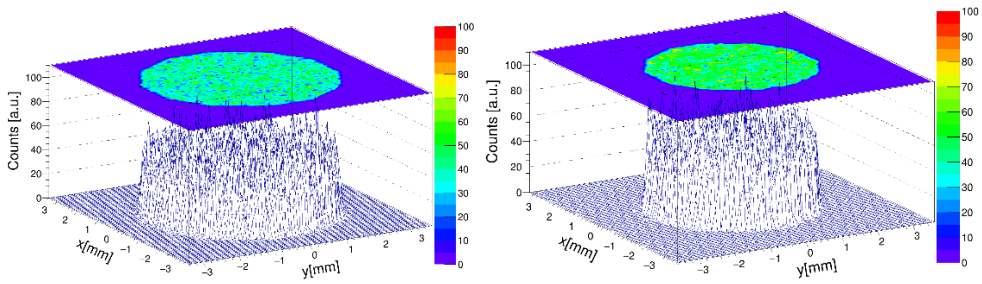


Fig. 25 − The beam spots at the target position for the experiments with the THGEM array and the 12.9 MeV (left) and the 18.5 MeV (right) sources.

For in-beam experiments at ELI-NP, a possible solution is to use fast preamplifiers based, for example, on the Ortec V120 unit [43] and 48 timing channels, for example, a VME crate and two 32 channel CAEN time-digital convertor (TDC) [42]. Ten $^{232}ThO_2$ targets on $^{12}C$ backing of 2 mg/cm$^2$ thickness will be mounted in the chamber of the array. The THGEM array will be placed in a stainless steel reaction chamber of 50 × 30 × 30 cm$^3$. The chamber will be operated as a gas flow chamber using isobutene at a pressure of $p$ = 5 mbar. Absorbers will be used for stopping the fission fragments

This setup will be used in two types of experiments: (i) measurement of cross-sections and fission fragment angular distributions as a function of the photon energy and mapping of fission resonances, and (ii) measurement of cross-sections and angular distributions of ternary α particles as a function of the photon energy by using polarized photons. Mapping of highly deformed states will be done, too.

Photofission experiments the THGEM array will be carried out in experimental hall E8 of ELI-NP. The setup will be mounted on a platform, along the beam line in E8, which will be positioned such that the center of the targets remain in-line with the beam axis. The alignment will be done using the ELI-NP laser tracking system.

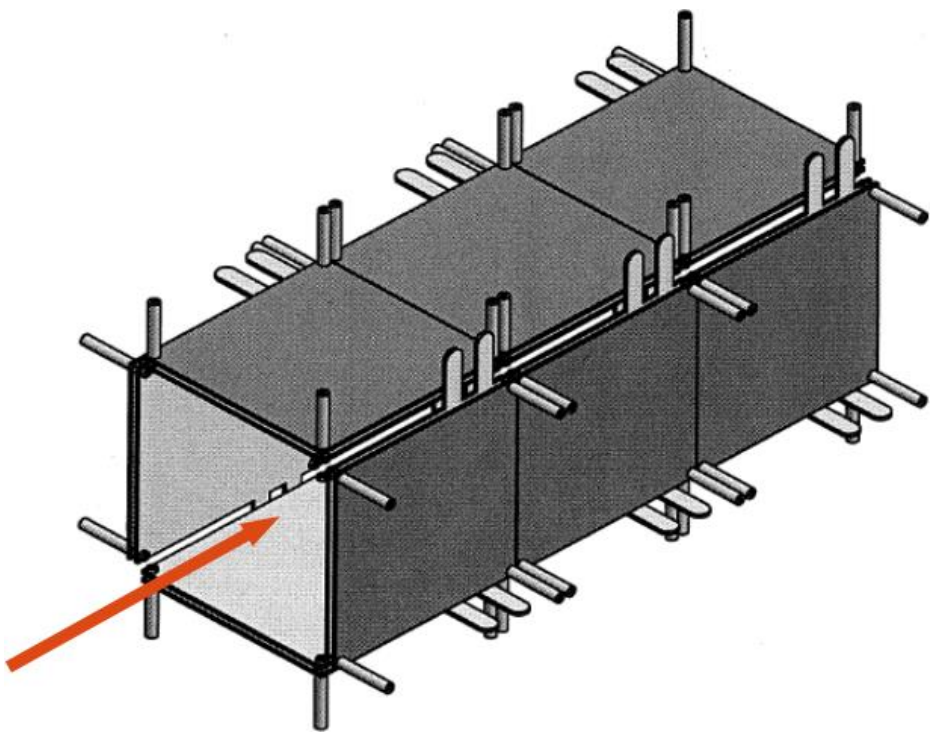

Fig. 26 − A 3D side view of the array of THGEM detectors.

### 3.3 IGISOL beam line and beam transport to measurement stations

The conceptual idea of the ELI-NP IGISOL beam line is presented in Fig. 27. The location of the IGISOL setup is defined based on the best usage of the ELI-NP γ beam. The ELI-NP IGISOL facility is considered to be built in two stages. A demonstration phase (phase I) in which the IGISOL setup will be mounted right after the high-energy interaction point of the ELI-NP GBS. In this case, space in the GS (Gamma Source) room and in experimental hall E1 of the ELI-NP laboratory building will be used. The space needed for setting up an IGISOL beam line in this area, commission it and start first experiments is available, and the option how to combine the IGISOL beamline with other experiments or beam-diagnostic measurements, which will be done here, has been worked out. A possible realization of the setup is shown in Fig. 28.

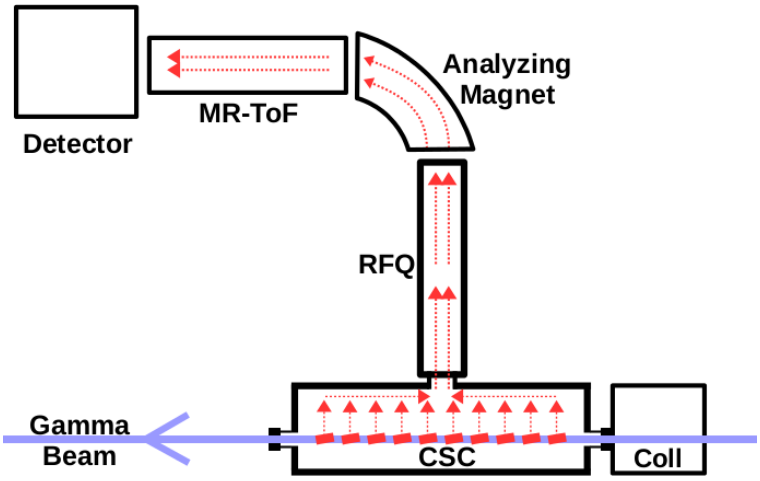


Fig. 27 − Main components of the IGISOL beamline at ELI-NP include the collimator and the CSC, which are mounted along the axis of the gamma beam. Tilted targets release fission fragments in directions depicted by dashed arrows. The RFQ, the analyzing magnet and the MR-TOF-MS prepare the radioactive beam for measurements.

The CSC and the radio frequency quadrupole (RFQ) will be mounted on a common platform, which can be placed in and out of the γ beam. Two possible scenarios for the IGISOL system are considered: (i) a cryogenic stopping cell (CSC), followed by RFQ ion cooler and a MR-ToF mass separator, adjacent to them, and (ii) after the CSC and RFQ devices, the beam is sent to analyzing magnet (classical mass separator). After that the beam goes to the measurement stations. The advantage of the first scenario is that mass measurements can be done in addition to the beam separation, and a very compact experimental setup can be realized.

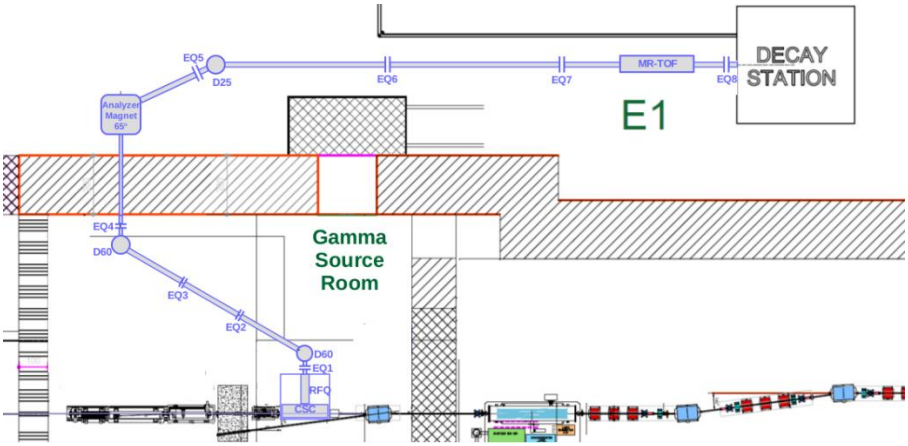


Fig. 28 − Layout of the IGISOL beam line in the ELI-NP laboratory building.

The Pb collimator and the CSC will be movable and can be placed in and out of the beam line, depending on the use of the IGISOL beam line. A concept is provided in Figs. 29 (top view) and 30 (side view), which demonstrates the way the CSC and RFQ devices can be moved with respect to the rest of the system, which will be fixed. The CSC and RFQ stand on a platform that can rise by 50 cm to take

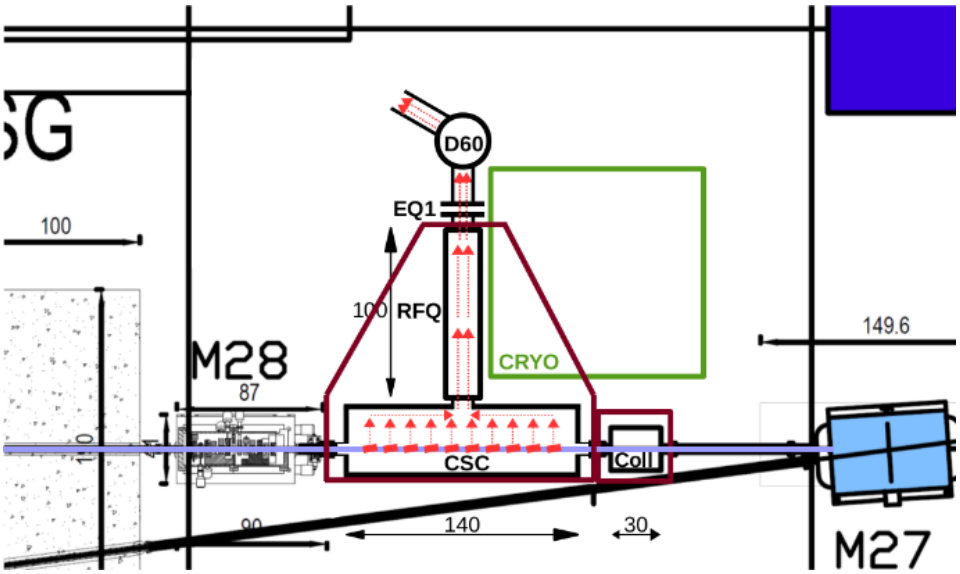


Fig. 29 − Top view of the CSC and RFQ placement in the GS room: The gamma beam in blue, the targets in red, ion trajectories are denoted with dashed red arrows, the CSC/RFQ and collimator platforms in brown and the cryogenic unit in green. The first two components of the beam transport line (EQ1 and D60) are shown in the figure, too. M27 and M28 indicate the electron beam deflecting magnet and the γ beam collimator of the GBS. The dimensions are in centimeters.

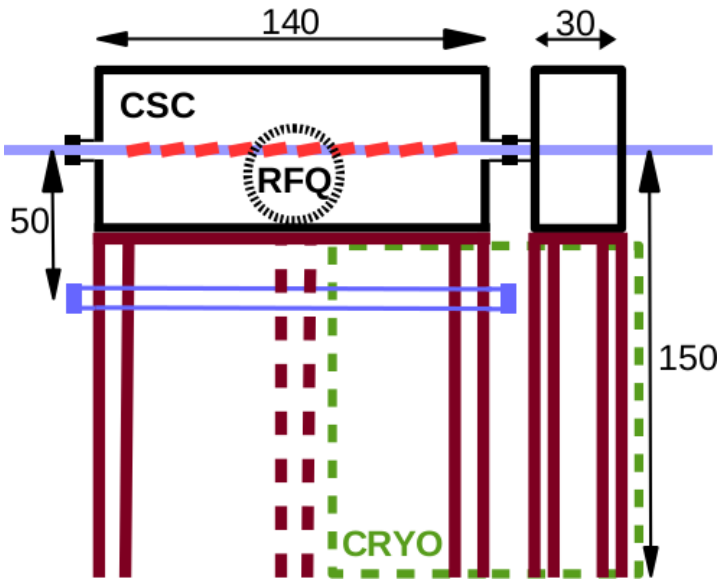


Fig. 30 − Side view of the CSC and RFQ placement in the GS room. The notations are as in Fig. 29. The CSC/RFQ platform (in brown, to the left) can be lifted by 50 cm. The collimator platform (in brown, to the right) can be either lifted by 50 cm, or shifted by 20 cm towards the cryogenic unit.

them out of the gamma beam, while the collimator stands on its own platform that can either slide horizontally 20 cm towards the cryogenic unit to take it out of the gamma beam, or can be lifted by 50 cm. The CSC requires infrastructure which has to be mounted close to it. This includes a gas-flow cryostat, indicated in green in Figs. 29 and 30, and a He gas recovery unit, for He recirculation and purification. There are two options for placement of this unit – in the basement or on the roof of the GS room just above the CSC ion catcher. This part of the roof is realized with casted concrete.

The contribution of the scattered γ rays and of the annihilation photons is negligible. GEANT4 simulations were performed to evaluate the scattered γ beam from the production targets. The results are illustrated in Fig. 31.

The distribution of the ionization events in the CSC gas is presented in Fig. 32: the blue dots show the ion-induced He ionization vertices, where the ions are fission fragments released from the targets, and green dots are electron- and positron-induced He ionization vertices, where these electrons and positrons originate from $\gamma \rightarrow e^+e^-$ pair production processes in the targets. The pair production vertices are shown with black dots in Fig. 32 and, due to their high rate, fill the entire volume of the 27 targets used in the simulation.

The results of the GEANT4 simulations of the CSC setup, which was described in Section 2.3, are presented in detail in Appendix C. Here we emphasize the main

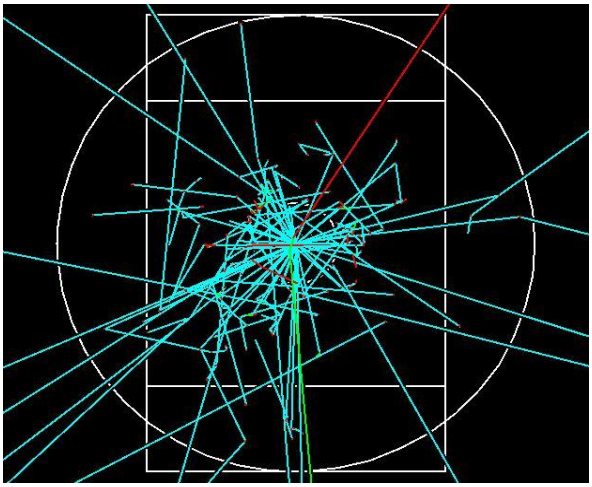

Fig. 31 − Beam view of the gas cell geometry, illustrating scattered γ beam. The collimator inner and outer radii are 4.5 and 20 mm respectively, the Al window is of 25 × 25 mm$^2$ and transversal gas cell dimension is 25 × 40 mm$^2$.

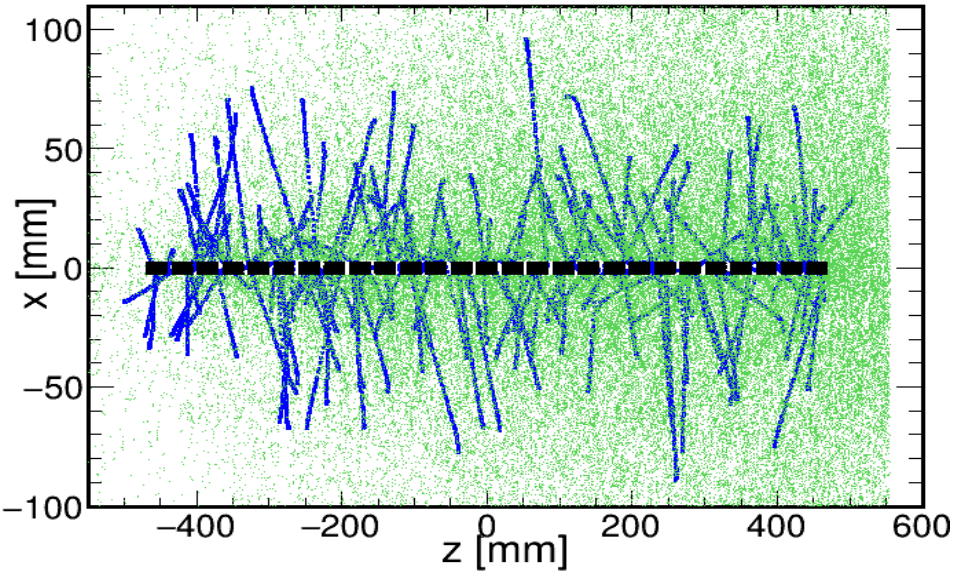


Fig. 32 − A 2D view of the ionization processes in the gas cell. Black dots are vertices of $\gamma \rightarrow e^+e^-$ pair production in the 27 targets of $^{238}$U, green dots are vertices of $e^+/e^-$-induced ionization and blue dots are vertices of ion-induced ionization (by fission fragments). The gamma beam propagates along the $x = 0$ line from left to right.

results. About 11% of the fragments produced in photofission leave the 10 μm targets. In the case of 7 μm targets, 16% of them leave the target, hence a 45%

increase of the release efficiency. However, using 7 μm targets also implies an increase in the number of targets, if one wants to keep the mass of uranium to its maximum value of 800 mg for the first phase of the experiment. Space limitations that exist in this phase put a limit on the maximum number of targets that one can use, effectively reducing the gain due to increased release efficiency of thinner targets.

The ions of the fission fragments lose on average about a third of their energy in the target. The average energy of the released ions is $\langle E \rangle \approx 57$ MeV, with a very small variation for the two thicknesses. This energy is then deposited in the cell gas. The rate of energy deposition via ionization by the fission fragments in the gas in the stopping volume of the cell is about 15 GeV/(cm$^3$·s). This is the largest contribution to the total energy deposition via ionization. The next largest contribution is coming from the gas ionization induced by $e^+/e^-$ from pair production in the target, with less than 5% of the total. It should be noted that while the peak of the energy deposition by the fragments is about 7 cm away from the targets (see Appendix C), that of the energy deposition by electrons and positrons is close to the targets (see Fig. 32). Radioactive beams with kinetic energies up to 2 MeV/u at high intensities are stopped at the Hermholz Center for Heavy Ion Research (GSI) in Darmstadt, Germany, in a CSC with similar volume, 1 m length and 25 cm diameter [44, 45]. This regime of operation implies rates of energy deposition superior the present estimates, giving us confidence that the space charge effects will not significantly affect the efficiency of the CSC at ELI-NP.

Next, an estimate of the possibility for creation of space charges in the CSC has been done. The simulated events in Fig. 32 indicate that the ionization process is equally distributed throughout the volume of the gas cell. Note that ultraviolet photons with energies $E_{uv} \approx 10$ eV, which are created in the gas volume are not taken into consideration by GEANT4. On the other hand, they contribute significantly for the space-charge creation and their contribution needs to be studied, too.

At an ISOL facility the intensity of the separated and detected radioactive beam of interest depends on many factors. It can be characterized as follows:

$$I = \Phi \cdot \sigma \cdot N \cdot \varepsilon_{target} \cdot \varepsilon_{source} \cdot \varepsilon_{separator} \cdot \varepsilon_{det} \tag{4}$$

Here $\Phi$ is the flux of the incoming beam, $\sigma$ is the reaction cross section, $N$ is the number of atoms in the target, $\varepsilon_{target}$ is the isotope release efficiency of the target, $\varepsilon_{source}$ is the efficiency of the ion source, in our case the CSC ion extraction efficiency, $\varepsilon_{separator}$ is the ion separation efficiency and $\varepsilon_{det}$ is the efficiency of the detection system. All these factors have been studied in order to define the feasibility of such experiments at ELI-NP. The target element release efficiency is $\varepsilon_{target} \approx 10-20\%$ (see Appendix C). However, there is room for further optimization of this parameter. A next round of simulations should answer what are the optimal number, titling angle, thickness, dimensions and spacing of the targets [46].

### 3.3.1 IGISOL Gas Cell and RFQ Ion Cooler

The IGISOL thin-target technology can be realized in two ways, through ion neutralization in a gas catcher and subsequent ionization with a laser ion source (LIS), or through ion survival in the gas cell (IGISOL ion survival). Both schemes are used in different laboratories. A key element in this technology is the gas catcher (or gas cell). In this case creation of space charge and its distribution in the gas cell need to be evaluated. This should be followed by efficiency calculations of the gas-catcher ion transport. Typically noble gases, Ar or He, are used for stopping and thermalizing the recoiling ions, as well as transporting them by the gas-flow through a differential pumping system towards the acceleration stage of a mass separator.

Another option is the ion transport to be done by electric fields, which guide the ions. The electric field transport takes over for ions with energies below 1 keV. The slowing down of the ion in the gas changes its charge state by means of charge-exchange collisions, which are determined by the velocity of the ion. In a 100% pure gas, the recoiling ions can reach a $2^+$ charge state in He, because for most elements the second ionization potential is below the first ionization potential in He. However, impurities of $H_2$, $O_2$ or $H_2O$ at a sub-ppm level can reduce the charge state to $1^+$, or lead to neutralization. In Ar, a $1^+$ charge state can be reached for most elements. Several mechanisms lead to a decrease of the transport efficiency, recombination losses due to three body interactions with impurities, diffusion to the walls of the gas catcher and plasma screening and space-charge effects, which become important at high ionization rates in the gas cell. At ELI-NP a Cryogenic Stopping Cell (CSC) is suggested to be used, which will be placed between the M27 deflection magnet and the M28 collimator (see Fig. 28). It will have its own γ beam collimator, which is indicated in Fig. 28, to select a γ beam with energies that overlap with the Giant Dipole Resonance (GDR) of the target ($^{238}$U). The CSC and the RFQ ion cooler will be moved, together with the collimator, out of the beam area when experiments are not performed at the IGISOL beam line.

After collimation, the γ beam at the CSC entrance will be in the energy range of 10−19.5 MeV with an intensity of about $2.3\cdot10^{10}$ γ/s and a spot size with FWHM ≈ 5 mm. The $^{238}$U targets inside the CSC will have a thickness of up to 10 μm to allow for the release of the fission fragments which are produced in the center of the target [47]. Hence, a set of thin targets will be used and, in order to avoid fragments from one target hitting neighboring targets, they must be arranged in the geometry sketched in Fig. 7. Up to 27 rectangular targets will be used, which correspond to less than 800 mg $^{238}$U, inclined at an angle $\theta \sim 10^{\circ}$ with respect to the γ beam, with the $d$ = 5 mm and $L$ = 29 mm to cover the γ beam spot. Once the dimensions of one target are established, the maximum number of targets (27) is fixed by the maximum mass of $^{238}$U suggested to be used, $M \leq 800$ mg. The total length of the target region inside the CSC is then about 1 m.

To estimate the CSC width along the fission fragment release direction, which is perpendicular to the target foils, a GEANT4 simulation of their stopping in the He gas was done. Appendix C details the results of this simulation. The main result regarding the CSC design is that more than 95% of the fragments, which are released from the targets, are stopped in about 12 cm of He gas at 70 K and 300 mbar, as shown in the left plot of Fig. C7. This implies that the diameter of the gas cell should be about 25 cm.

Fig. 33 − A CSC at GSI: the gold-colored cylinder in the upper side of the figure. The cryogenic unit is in the center and its precooling Dewar vessel is on the left side. Published with permission of GSI.

The extraction of the fission fragments can be done using just a gas flow only if the cell is small [47]. For a gas cell with the size described above, extraction only by gas flow would take too long for short-lived radioactive nuclei to survive. Hence, it is suggested to use a different extraction method that combines extraction via DC and radio frequency (RF) electric fields with gas flow extraction close to the cell nozzle. The advantages of this approach are an increase of the stopping power and the freezing out of the impurities. The price to be paid is the need of a cryogenic structure.

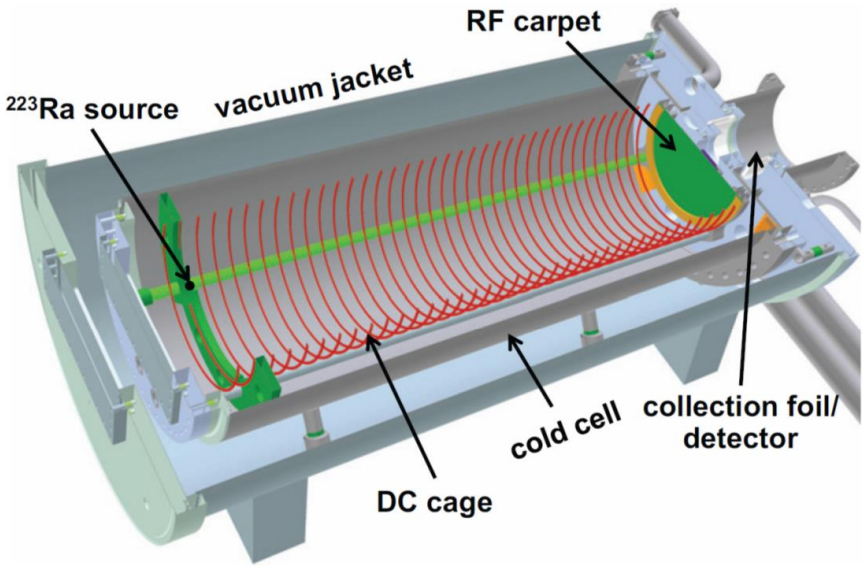


Fig. 34 − A 3D model of the GSI CSC [48]. Between the outer chamber which is at room temperature, and the inner chamber which is cooled down to about 70 K, there is vacuum isolation. The DC cage electrodes are in red and RF front cap carpet is in green. The gas exit hole is in the center of the RF carpet, where the extraction RFQ starts. Published with permission of IOP Science.

Such a gas cell, with an active length of 1 m (1.4 m with vacuum enclosure), is the CSC built and used at the Fragment Separator (FRS) at the Ion Catcher Facility at GSI, Darmstadt, [44, 45] (see the picture in Fig. 33). A 3D-model of the GSI CSC is shown in Fig. 34. Several innovative technologies are employed in its design: (i) large DC fields (up to 30 V/cm), created by ring electrodes, for fast ion extraction; (ii) RF carpets: resonant RF fields (6 MHz) that prevent ion adhesion to the cell walls and direct the ions towards the exit nozzle [48]; (iii) cryogenic operation (around 70 K) for increased ion stopping and gas purity [49]. These innovations allowed fast (about 25 ms) and efficient (about 50%) extraction of the fission fragments.

A new design of the CSC, with transversal extraction on the top of the gas cell with respect to the beam instead of longitudinal extraction, was suggested by the GSI group [50]. The most significant new features of this CSC are: (i) orthogonal extraction, providing shorter extraction path; (ii) cell division in two chambers with different pressures, 300 mbar and 10 mbar, respectively, which facilitates a very efficient gas pumping; (iii) higher DC field strengths, which are possible due to the shorter length in direction of the extraction; and (iv) smaller ratio of RF carpet area to stopping volume, hence smaller power dissipation and improved cryogenic operation. All these improvements are expected to allow faster, as low as 5 ms, and more efficient (close to 100%) extraction, at a rate of $10^7$ ions/s injected in the gas cell.

The CSC with transversal extraction is the design of choice for the ELI-NP IGISOL beamline. Its conceptual design is shown in Fig. 35. This decision is based on the following arguments: (i) increased fission fragment rates; (ii) shorter extraction times; and (iii) higher energy deposit in the gas. The CSC will sustain heavy ion rates up to $10^7$ ions/s, similar to the expected rates at the SuperFRS facility, while the current CSC design allows ion extraction at rates below $10^4$ ions/s, the current rates at the FRS facility. The design of a cell with transversal extraction is expected to result in a decrease of the extraction time by a factor of around five, which permits measurements of wider range of neutron-rich isotopes, pushing the limit towards shorter-lived isotopes. The tolerated value for the energy-density rate, which is deposited in the gas via ionization, can take higher values before space charge effects affect significantly the CSC functionality.

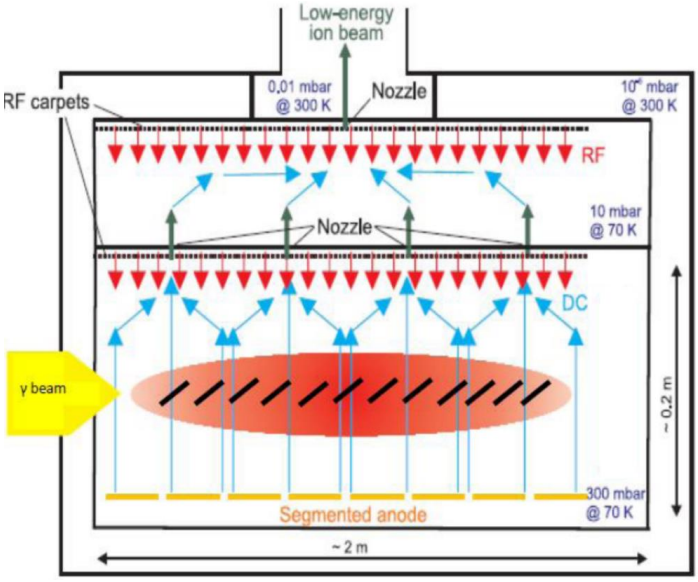


Fig. 35 − Conceptual design of a cryogenic stopping cell with orthogonal extraction.

The CSC will be equipped with a gas recovery unit allowing for the recirculation and purification of the inert gas (He) and a liquid-gas-flow unit with a cryocooler system that keeps the temperature at levels T ≈ 60−90 K [44, 45]. By using these technologies, the impurity level inside the cell is kept at a level below 1 ppt which significantly reduces the rate of ions, which form molecules with the gas impurities. Also, lower temperatures lead to larger densities of the extracted jet through the exit nozzle at a given gas density inside the cell, hence higher extraction efficiency at the same He pumping capacity.

There are two possibilities for the ELI-NP CSC, to use the existing GSI CSC, which is proven to work, or to develop and employ the new design with transverse

extraction [50]. In both cases the targets will be placed in the central area of the CSC, as shown in Fig. 35. It is suggested that for the ELI-NP CSC the new design should be employed.

The radiofrequency quadrupole (RFQ) ion cooler at the Facility for Antiproton and Ion Research (FAIR) in Darmstadt, Germany, [51] is designed to transport the high-intensity beam which exits the CSC with low kinetic energy, of the order of a few eV. Note that the CSC and RFQ should handle the $10^7$ ions/s beams separated by the SuperFRS facility at FAIR. The RFQ is compact, at about 1 m, modular and maintains a high transmission efficiency of about 90% for mass resolution $m/\Delta m \approx 240$. The beam extraction is done by differential pumping with two 1000 l/s turbomolecular pumps creating a pressure of $2\cdot10^{-2}$ mbar. Note that the pressure inside the cell is at least 100 mbar. Next stages perform beam cooling along 20 cm at $3\cdot10^{-2}$ mbar, mass separation along 40 cm at $10^{-4}$ mbar and beam bunching along 46 cm at $5\cdot10^{-3}$ mbar. The RFQ uses He as buffer gas. The design the ELI-NP CSC will be done in such way that the existing high-efficiency GSI RFQ ion cooler can be used.

Of utmost importance for the performance of the CSC is the gas cleanliness, which sets severe requirements on the gas-transport system, with ultraclean tubes, cryocatchers, etc. The gas-transport system includes its own He storage vessel and a gas purification system, which should be placed in basement (or on the roof of the GS room), together with the pumps.

The ion beam, which is prepared after the RFQ ion cooler, is well defined and can be used for ion-optics calculations, for further analysis and purification of the beam and bringing it to the experimental measurement stations. Typical emittances of RFQ in the $(x,y)$ space for $^{133}$Cs ions are presented in Fig. 36. The coordinate spread of the beam is $\sigma_x = 0.065$ mm and $\sigma_y = 0.069$ mm and the velocity spread of the ions is $\sigma_{vx} = 0.47$ km/s and $\sigma_{vy} = 0.50$ km/s.

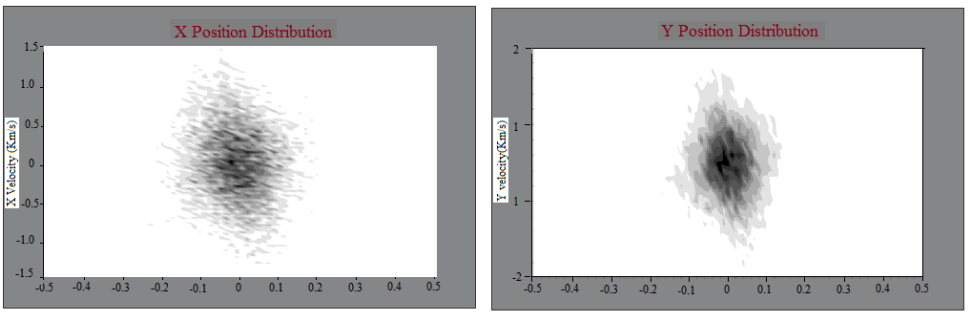


Fig. 36 − Emittances of the GSI RFQ in the *x*-space (left) and in the *y*-space (right).

**Comparison of the performance of the ELI-NP IGISOL facility with other IGISOL facilities:** Laboratories, which focus their research programs on the extraction of refractory elements, are the CARIBU ion source at the ANL in USA, the IGISOL-4 facility at JYFL, University of Jyvaskyla, Finland and the SLOWRI beam line at RIKEN, Japan. The yields are compared after the RFQ, when the beam is formed.

The expected isotope yields at the ELI-NP IGISOL facility are deduced with Eq. 4, and the target fragment release efficiency was accepted as $\varepsilon_{target} \approx 0.2$, the source efficiency as $\varepsilon_{source} \approx 0.2$, which was obtained considering an efficiency of the CSC of about 25% and an efficiency of the RFQ of about 90%. The expected total photofission rate is about $10^7$ f/s, which means that an extraction of about $9 \cdot 10^5$ ions/s can be expected.

There are several possibilities to increase the isotope yield at the ELI-NP IGISOL facility:

(i) **an increase of the target release efficiency**, which will be achieved by the optimization of the target thickens and the geometry of the target assembly;

(ii) **an increase of the target material quantity**, *e.g.* the simulations demonstrate that using 800 mg $^{238}$U exhausts only about 30% of the available γ beam; the optimal quantity of target material needs to be defined, combining sufficient target burning, creation of high-enough specific activity and fast ion transport within the CSC;

(iii) **an optimization of the delivered γ beam**, *e.g.* at present the parameters of the machine are optimized such that at the high-energy interaction point, the CBS meets the requirements for a brilliant narrow-width γ beams and utilization of broad-band beams was never looked upon; it is expected that an optimization of the electron beam parameters will result in an increase of the broad-band γ beam intensity; and

(iv) **an increase of the CSC efficiency**, *e.g.* at present we consider an efficiency of the CSC of about 20%, which has already been achieved with the existing gas cell, but with the new design with transversal extraction, higher efficiency of about 50% is expected.

All these factors indicate that there is room to increase the isotope yields at ELI-NP by an order of magnitude or more, which means that with this optimization two more masses away from stability can be reached for each isotope.

Next, the performance of ELI-NP is compared to the existing facilities. Considering an optimal operation of the ELI-NP IGISOL facility, the ELI-NP sensitivity line is set at about $10^2$ ions/s, which is sufficient for β-decay experiments.

At ANL the CARIBU ion source uses a 1 Ci $^{252}$Cf source deposited as a thin film. The isotopes of interest are produced in spontaneous fission. They are slowed down in a He gas cell, equipped with a RF carpet on the walls to direct the ions towards the Laval nozzle. After the extraction the jet is sent to a RFQ ion cooler, the He gas is pumped through a differential pumping system and the ion beam is accelerated to 120 kV [21]. The isobar separation is done via a high-resolution analyzing magnet ($m/\Delta m = 9000$) [52] and the isotopes of interest are sent to different

measurement stations. The experimental isotope yields of the CARIBU facility are presented in Fig. 37. Note that these yields have been achieved at the start of the facility and they are been continuously improved. At present, about 20% of the activity is extracted as ions form the $^{252}$Cf source.

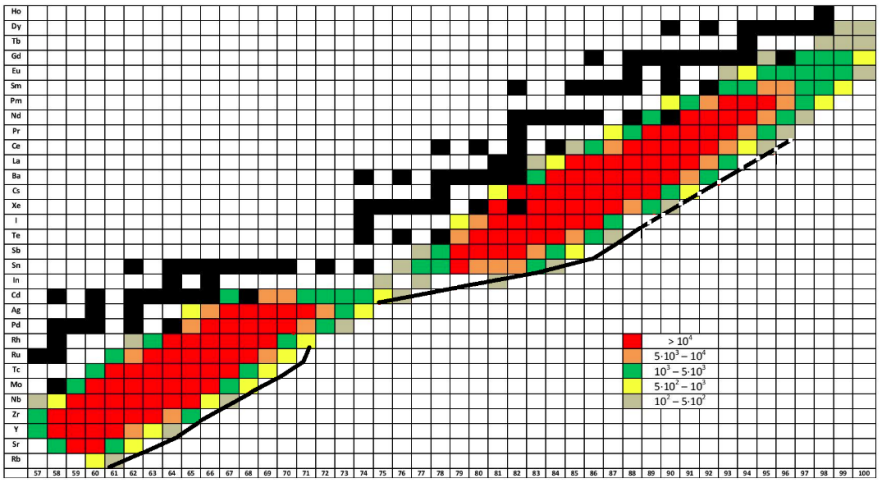


Fig. 37 − Experimental yields of fission fragments at the CARIBU $^{252}$Cf ion source at ANL. The solid black lines indicate the expected yields at the ELI-NP IGISOL facility, based on the measured low-energy fission yields [27]. The dashed line is extrapolation of the experimental data.

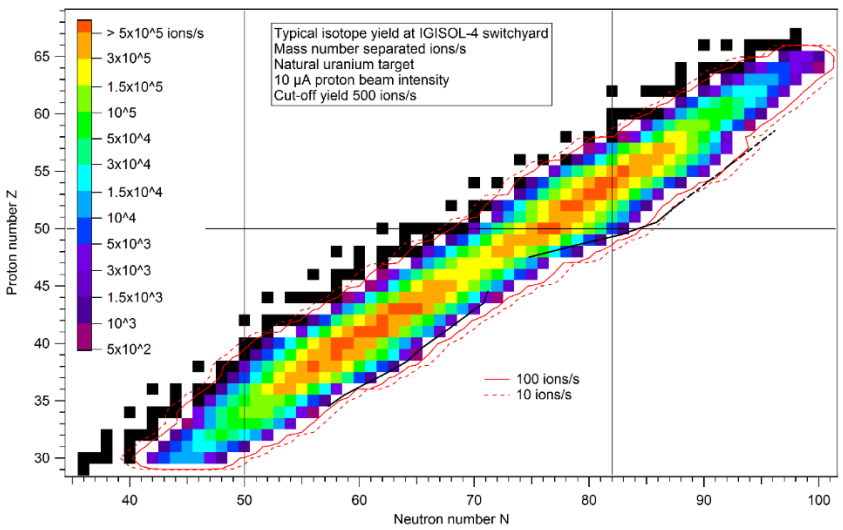


Fig. 38 − Expected isotope yields at the IGISOL-4 facility at JYFL, Jyvaskyla. The solid black lines indicate the expected yields at the ELI-NP IGISOL facility, based on the measured low-energy fission yields [27]. The dashed line is extrapolation.

Rare isotopes are extracted at the IGISOL facility at JYFL, University of Jyvaskyla following fission with low-energy protons, where this technique was pioneered [53]. At present, the IGISOL-4 facility is operational there [54]. The 10 μA proton beam hits a $^{nat}$U target. The isotopes of interest are slowed down are in He gas and are extracted by the He gas flow. The gas jet from the Lavalle nozzle is injected in RFQ ion cooler, which is a sextupole ion-beam guide (SPIG). A laser ion source (LIS) may additionally be used for element selection. The lasers shoot at the area of neutralization of the ions. Two-step acceleration to 10 kV and 40 kV is applied. The beam is analyzed via a $\Delta m/m$ = 1/150 analyzing magnet and sent to measurement stations. The expected isotope yields at JYFL, University of Jyvaskyla are presented in Fig. 38.

At RIKEN (in Japan), at the SLOWRI beam line, which is under construction, rare isotopes are produced, either by extracting the beam from the second stage of the BigRIPS spectrometer (the in-flight radioactive ion beam separator at RIKEN) as a ready beam, or at the disperse focus as a parasitic beam on both sides of the main beam. RF coating of the gas cell cylinder along the beam line is applied with a running wave potential. The gas cell ends with an end cup with etched end-cap coating. Either He gas cell (2 m long) where the RFQ carpet pushes the ions, or a Ar gas cell at 1 atm, where the beam is neutralized in 10 cm, are used. The gas jet from the Laval nozzle is injected in RFQ ion cooler, which combines quadrupole and octupole fields. A LIS is coupled to the ion guide. The ready beam after differential pumping is sent to three measurement stations: (i) for mass measurements with a MR-ToF-MS trap, which allows millisecond measurements, compared to about one second needed in a Penning trap, (ii) collinear laser spectroscopy beam line for nuclear moment measurements and (iii) a spectrometer for β-decay and delayed neutron emission measurements. The expected isotope production line of 1 ion/s at SLOWRI, RIKEN from [55] is presented in Fig. 39 with a full line. This line is given up to Sn ($Z$ = 50), but isotope production at SLOWRI extends well beyond this element. The comparison with the corresponding 1 ion/s line for the ELI-NP IGISOL facility shown with dashed lines in Fig. 39, implies comparable production rates with the first IGISOL phase at ELI-NP.

A comparison of the production isotope yields for the Mo ($Z$ = 42) and the Ce ($Z$ = 58) isotopes is presented in Figs. 40 and 41. The data are fitted with Gaussian curves. The extrapolation of the experimental yields which was done, *e.g.* in the case of the Ce isotopes, is described in Appendix B. The JYFL IGISOL-4 data are in green and the CARIBU data are in red. The expected ELI-NP yields are in blue, the filled blue squares (for Mo) and the solid blue line (for Ce) are the yields expected for the first phase of the ELI-NP IGISOL facility, while the open squares (for Mo) and the dashed blue line (for Ce) are the yields which can be realized after the optimization of the facility.

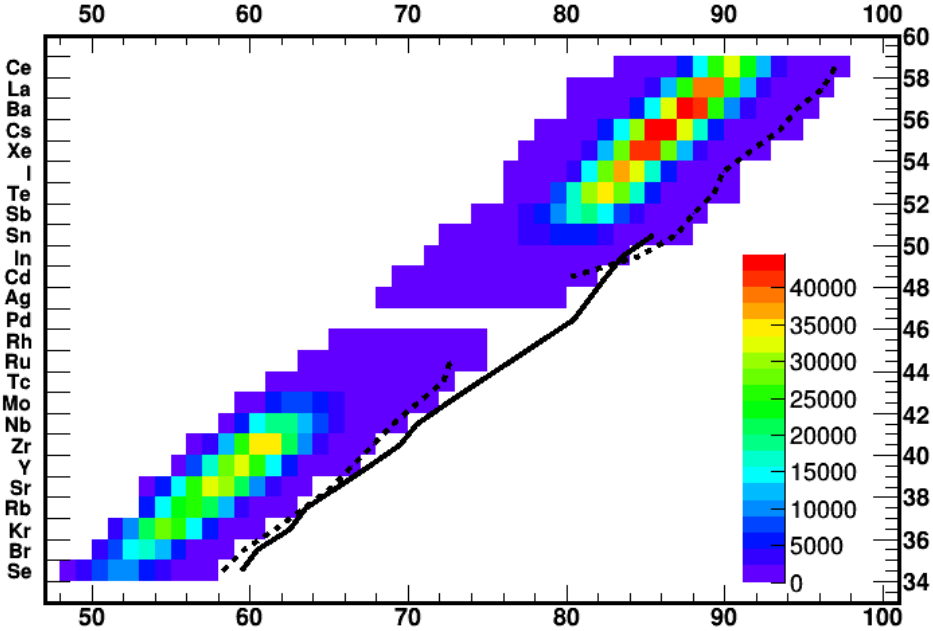


Fig. 39 − Expected isotope yields at the ELI-NP IGISOL facility. The solid black line indicates the expected line corresponding to 1 ion/s at the RIKEN SLOWRI facility. The dashed lines show the 1 ion/s line at the ELI-NP IGISOL facility.

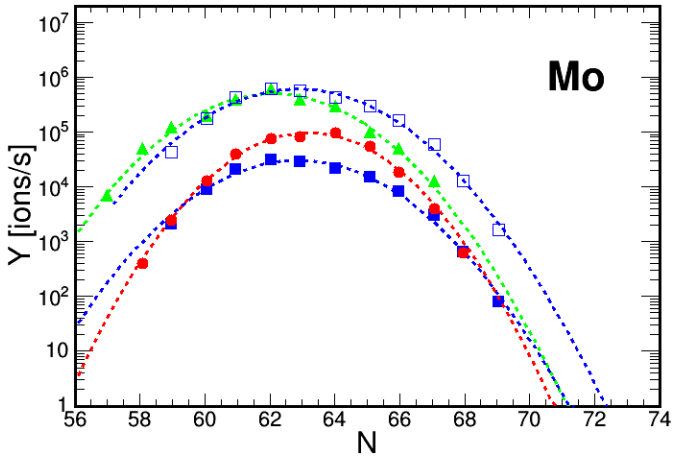


Fig. 40 − Comparison of Molybdenum production rates at CARIBU (red circles), IGISOL-4 at JYFL (green triangles), ELI-NP phase I (filled blue squares) and phase II (open blue squares).

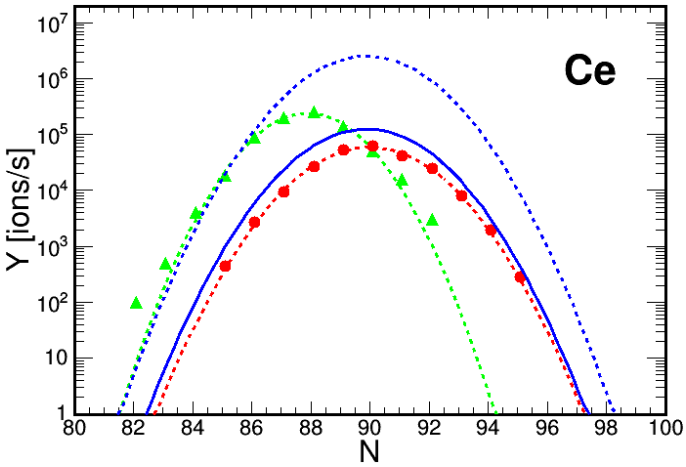


Fig. 41 − Comparison of Cerium production rates at CARIBU (red circles), IGISOL-4 at JYFL (green triangles), ELI-NP phase I (solid blue line) and ELI-NP phase II (dashed blue line).

### 3.3.2. Multi-reflection time-of-flight (MR-ToF) mass separator

The Multiple-Reflection Time-Of-Flight mass separator (MR-ToF-MS) unit [56] is a broadband and powerful mass spectrometer with a mass resolving power $m/\Delta m \approx 10^5$ obtained in a flight-time of about 5 ms. It can also be used as an ultra-high resolution mass separator to provide isobarically pure beams. Such device will be used also for laser-driven nuclear physics experiments and is described in more detail in the corresponding HPLS TDR1 "Laser Driven Nuclear Physics Experiments at ELI-NP".

The best position for the MR-ToF mass separator is right behind the CSC. The device is very important for the optimization and the commissioning of the CSC. With the MR-ToF-MS mass measurements will be possible, at much lower rates than those discussed in Section 3.3.1. The sensitivity limit can be set at one detected ion per hour. Considering a detection efficiency of 20%, experiments will be possible at rates of 5 ions/h.

### 3.3.3. Laser Ion Source

A laser ion source (LIS) at ELI-NP is not considered as a first priority project, because the beam purification can be achieved in a much simpler way. However, space for a laser hut, which can host lasers is foreseen, *e.g.* on the roof of the GS room above the IGISOL beam line, in a section done by casted concrete. This allows the laser beams to be sent to the interaction point with minimum reflections. A minimum space of $6 \times 3$ m$^2$ is required, but in case the hut hosts lasers for collinear laser spectroscopy, additional optical tables should be placed there. The required

space and a typical distribution of the laser room are shown in Fig. 42. The laser tables will be placed on the roof of the GS room, which is on the anti-vibration slab of the ELI-NP laboratory building. The floor of the hut will be elevated in a way that it is not in contact with the tables. Space for mounting of the laser power supplies outside of the laser hut should be foreseen. It should be equipped with its own chiller system and closed-circuit $H_2O$ system. It should have filter system above the optic tables, and its own ventilation (under-pressure air system).

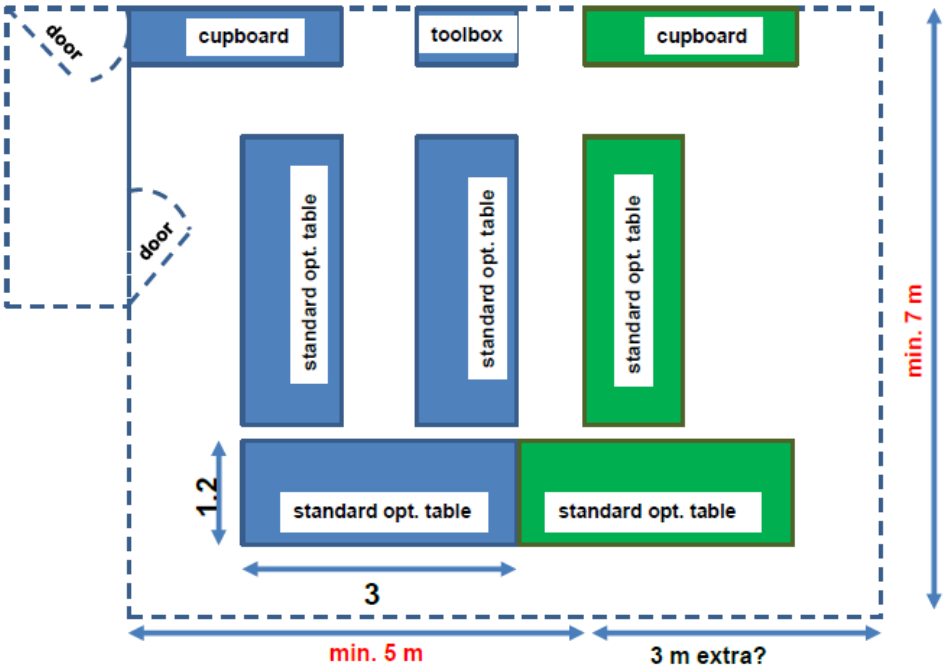


Fig. 42 − Space requirements and equipment distribution for a laser hut of the IGISOL facility. In blue is the equipment for the LIS and in green for collinear laser spectroscopy.

### 3.3.4 Mass separator

Herewith, an approach of beam extraction, beam transport and isotope mass separator design has been proposed. As explained before, we consider two scenarios for the ELI-NP IGISOL beam line, in one of them, which was discussed in Section 3.3.2, the mass separation is done with a MR-ToF-MS. Here we discuss the use of a classical mass separator. Within the Photofission WG we have considered a provisional ion-beam transport line to the E1 experimental area in order to define the elements of the beam optics. A more precise layout of the beam line, taking into

consideration all the equipment which will be placed in the GS room and in the E1 experimental area, is presented in Fig. 28.

**General considerations:** The total transport time of the produced nuclides between the target room and the experimental hall has to be as short as possible. The nuclides are transported initially as a gas steam, later as ions. Due to geometrical constraint related to the limited space, the mass separator has been provided with an magneto-optical beam line section made of two deviators connecting the ion guide and the first quadrupole system in the target room with the rest of the apparatus in the experimental hall.

The mass separator has been designed so as to allow the simultaneous collection of a wide range of masses, about ± 5% relative mass difference on both sides of the central beam ($M \sim 100$). Moreover, it gives more freedom in operational conditions, for example in the choice of mass marker used for control of beams. Nearly circular focal spots of 1−2 mm diameter (FWHM) are obtained in the focal plane, to be compared to the distance of 14 mm (for a central mass of 100) between consecutive isotope beams. The radius of curvature of the electromagnet is defined by the geometry of the magnet.

**Electrostatic ion optics:** The starting conditions are influenced by the beam extraction parameters: the maximum extracted intensity, the emittance of the beam and positive space charge compensation by secondary electrons resulting from the interaction of ions with residual gas molecules. A preliminary study has been performed using the code TRANSPORT [57] for the general implantation of the separator into the dedicated experimental hall (Figs. 43 and 44). The ion source front end is located at position PV20 of the gamma beam line. The beam will be transported from the GS room towards the E1 experimental hall after crossing the shielding hall at position PAR20. The beam tube diameter is defined from the estimate of the ion beam radius at the entrance and the exit of the tube located at the shielding wall of 1 m thickness.

The convergence of the beam should be towards the center of the tube. For geometrical reasons, two 60° deviations of have been considered for the transport of the beam upstream of the magnet.

The virtual image of the source point at the exit of the RFQ has been obtained by the mean of an electrostatic quadrupole doublet EQ1. This image is used as the object point for the magnet. The diameter of the beam tube has been limited to 150 mm to guarantee an acceptable conductance of the beam tube. The quadrupole doublet EQ4 allows adjusting the amplitude of the beam and improving the magnet resolution. The beam transmission between the two deviators is improved by the mean of the quadrupole doublet EQ2 and EQ3. The quadrupoles have an aperture of 110 mm diameter and an electrode length of 175 mm. Along the transport beam line, deflection plates are used to correct the beam position and the angle at the entrance of the deviators and the magnet. To obtain an achromatic beam (both angle and position) and the requested focalization on the β-delay tape transport system four

doublets of quadrupoles are inserted in the emergent beam line from the magnet separator. The three electrostatic deflectors D60 and D25 have an effective length of

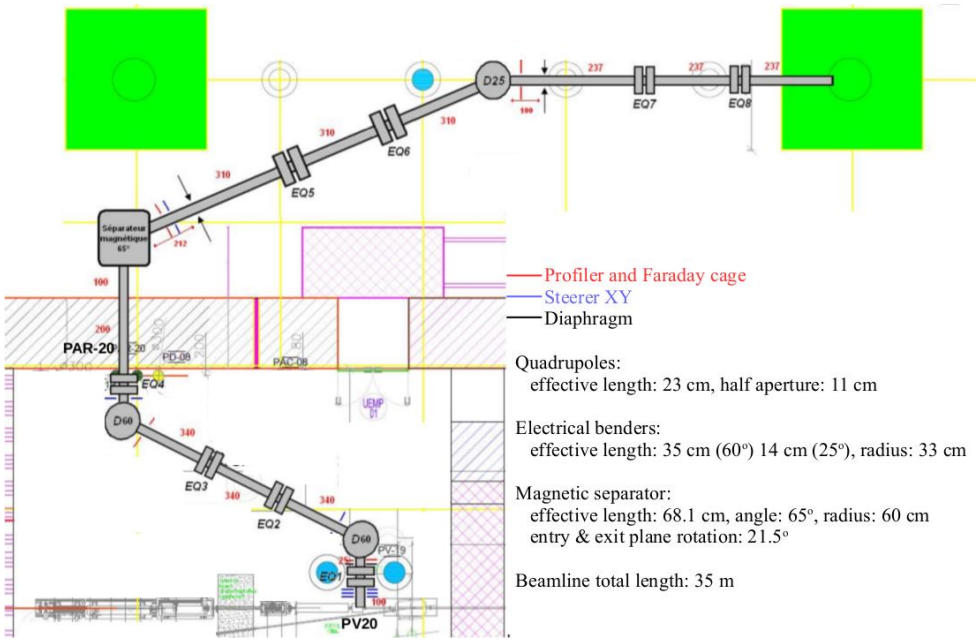


Fig. 43 − Layout of the IGISOL beamline in the Gamma Source room and the E1 room.

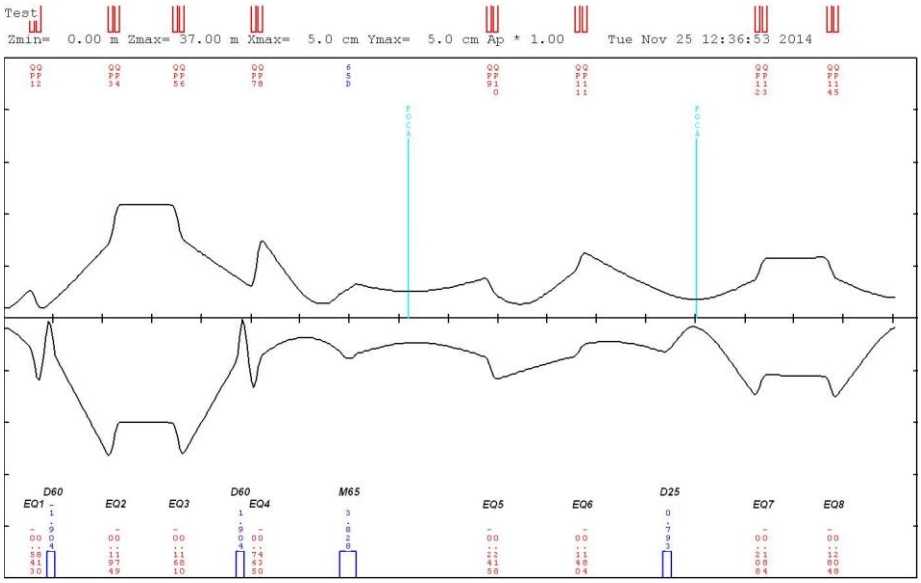


Fig. 44 − Calculation of the beam transport from the exit of the RFQ toward the tape station.

33 cm for curvature radius of 31 and 75 cm respectively. For focusing, the needed high voltage supplies are all identical, *e.g.* 10 kV stabilized to $10^{-4}$%.

The stable mass marker beams diagnostic is performed by the mean of profile monitor, scanners at the entrance of the tube and the entrance of the magnet and also by the mean of faraday cups and/or μ-channel plates to measure the beam intensity.

**Magnet separator specifications:** The magnet separator is similar to the existing one used at the ALTO facility. The design consists in an electromagnet having the following parameters: (i) deviation with a deflection angle of 65°; (ii) radius of 600 mm, a pole gap of 66 mm; and (iii) angle tilt of 21.5° at the entrance and the exit of the magnet.

The magnet is powered with a stabilized current supply which varies from 0 to 280 A to get a maximum magnetic field of 7310 G. Usually, for the separation of fission fragments at ALTO, the current applied to the magnet does not exceed 150 A. It is stabilized to $10^{-3}$ over a period of several hours to limit the deflection of the beam in the focal plane (less than 0.3 mm). Note that for collinear laser spectroscopy experiments, the stability which is needed is $3\cdot10^{-5}$. The obtained dispersion at ALTO is better than 1370 allowing a distance between consecutives masses in the focal plan of 13.7 mm. Mechanical design of the chamber based on the existing one at ALTO will be adapted to the ELI-NP mass separator.

**Vacuum system:** An adequate vacuum is maintained in the separator by means of five turbo pumps placed as follows:

(i) On the extraction chamber for differential pumping 1500 l/s,
(ii) On section 1 located between the two 60° deviations 1000 l/s,
(iii) On section 2 upstream of the analyzing magnet 1500 l/s,
(iv) On section 3 downstream of the magnet 1000 l/s,
(v) On section 4 downstream of the magnet after the 25° deviation 1000 l/s.

Typical pressures of $5\cdot10^{-6}$ mbar will be achieved after the extraction chamber and $2\cdot10^{-6}$ mbar in both beam line sections.

**Remote control and indicators:** The control system consists in the remote control of parameter settings from different components of separator (magnet, optics, diagnostics) to the control desk. Regarding the indicators, transfer of readings (magnetic field, diagnostic parameters) are provided from different components level to the control desk. The control of other parameters related to the safety and services (vacuum, water cooling, etc.) is also required.

### 3.3.5 Beam transport system

As discussed before, we consider two solutions, to build the whole system in the GS room, or the use the measurement stations at the E1 experimental area, which will be common with the laser-driven nuclear physics experiments, *e.g.* to a β-decay measurement station. The IGISOL beam-transport line is described in Section 3.3.4. Its total length is 35 m.

### 3.3.6. Measurement stations

At all ISOL and IGISOL facilities there are measurement stations, which measure masses, β-decay and nuclear moments and mean-square charge radii. We suggest at ELI-NP to design and set first a β-decay tape-transport system. This experimental setup will be designed and used also for laser-driven nuclear physics experiments and will be described in more detail in the corresponding TDR.

A β-decay tape-transport spectrometer is suggested to be jointly built by groups from the Institut de Physique Nucleaire d'Orsay (IPN) and the Department of Nuclear Physics of the "Horia Hulubei" National Institute for R&D in Physics and Nuclear Engineering (IFIN-HH). This spectrometer will be used at the ALTO and ELI-NP facilities, as well as at the DESIR facility of SPIRAL2. A view of the spectrometer is presented in Fig. 45.

The specific features of the proposed detection setup are related to the requirements of the method, namely:

- high-efficient gamma-ray array with a reasonable energy resolution. For this purpose we envisage to combine advanced scintillator detectors (high-efficiency) with several Ge detectors, providing superior energy resolution.
- beta-detection setup, that would provide at the same time high efficiency and the possibility for beta-asymmetry measurements.
- holding magnetic field at the target position necessary for keeping the spin-polarization.

### 3.3.7. Space and building requirements

The location of the IGISOL setup has been defined on the basis of the best usage of the ELI-NP γ beam. The ELI-NP ISOL facility is considered to be built in two stages. A demonstration phase (phase I) in which the IGISOL setup will be mounted right after the high-energy interaction point of the ELI-NP GBS and the IGISOL facility will be assembled in the main ELI-NP building. In this case, the space available in the Gamma Source room and in the experimental hall E1 will be used. There is a constraint, related to the available space, which needs to be worked out with the civil engineering group, the gamma beam provider and laser beam experiments. Three layouts for the placement of the IGISOL beam line are presented in Figs. 28, 46 and 47. The first layout shows the full IGISOL setup extending from the GS room to the E1 experimental area, the second layout displays an IGISOL setup placed in the GS room, and the third layout is a version of the second without an analyzing magnet.

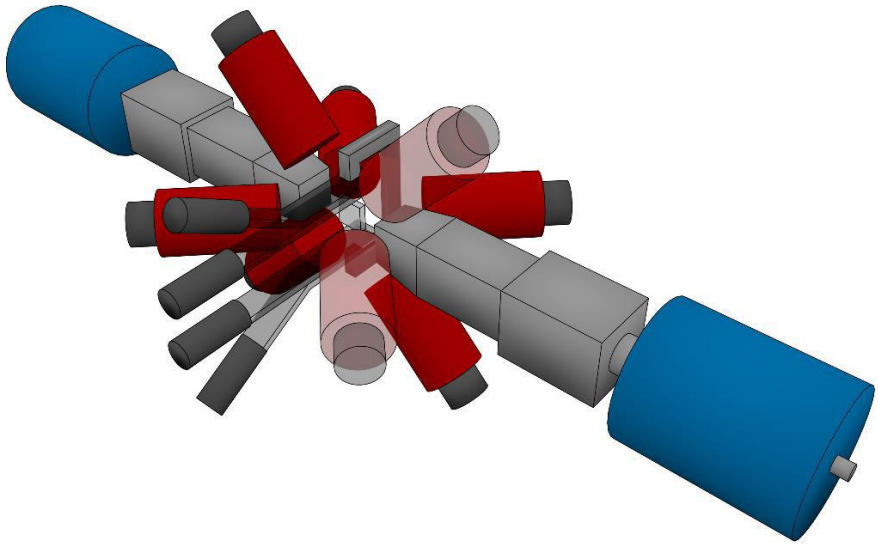

Fig. 45 − An artistic view of the β-decay spectrometer.

The latter two solutions will be used in the implementation phase of the project. The setup in Fig. 47 will be used *e.g.* for the commissioning of the MR-ToF-MS. The mass-separation will be achieved by using the second section of the RFQ and MR-ToF-MS. If the achieved separation is not sufficient, an analyzing magnet can be added to the setup, a layout is presented in Fig. 46.

The following specific needs for the assembly of the IGISOL beam line at the ELI-NP laboratory building are already foreseen:

- Space of about 2 m between elements M26 and M27 of the ELI-NP GBS, which is needed for mounting of the IGISOL collimator and the CSC;
- Wall penetration between the GS room and E1 experimental area of the ELI-NP laboratory building;
- Floor penetrations in the GS room, which are needed for the pumps and the gas-transport system, which will be placed in the basement (or on the roof of the GS room);
- Part of the roof of the GS room is executed with casted concrete, providing a possibility to place a laser hut on top of it, including the corresponding roof penetrations;
- Space at experimental area E1 for the ion-beam transport to the corresponding measurement stations there.

### 3.4 In-beam high-resolution gamma spectroscopy set up

The detectors of the ELIADE array will be used for in-beam γ-ray spectroscopy of fission fragments. Triple and higher-fold γγ-coincidence events will be recorded. The detectors of the ELIADE array might be be coupled to a Bragg spectrometer for identification of one of the fragments. The ELIADE array covers the backward angles. Thus, a BIC can be mounted at forward angles. Fast-timing $LaBr_3$ detectors, *g*-factor magnets and a fission plunger are considered for different assemblies of the setup. As stated in Section 2.4, a niche for the ELI-NP spectroscopic experiments are measurements of *g*-factors of exotic nuclei. Therefore, we consider in detail the feasibility of this type of experiments.

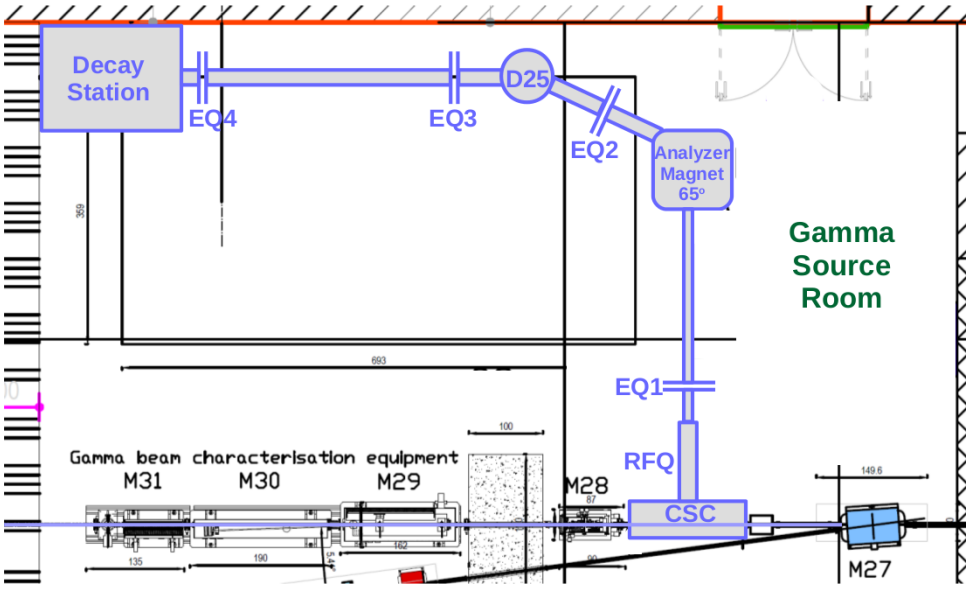


Fig. 46 − Top view of the placement of the whole IGISOL beam line in the GS room.

#### 3.4.1 Magnet assembly for *g*-factor measurements

One of the unique points for the present project is the possibility to provide an access to nuclear moment studies for short-lived isomeric states (100 ns and below) that are not accessible by other production mechanisms, *e.g.* in-flight fission or projectile fragmentation, which require the use of a fragment separator with a considerable time of flight. However, the nuclear moment studies of short-lived isomeric states would require the use of sufficiently strong magnetic fields, which at the same moment need to be sufficiently homogeneous. For example, a 3 T field would provide a period of the TDPAD $R(t)$ function of about 100 ns for an isomeric

state with a *g*-factor of 0.2. This would mean that isomeric states with lifetimes below 50 ns would be reachable. In such a case the low-lifetime limit would be rather imposed by the time resolution of the Ge detectors that is expected to be similar to 10 ns for energies above 300 keV. Thus, isomeric states down to 20 ns to 30 ns would be reachable.

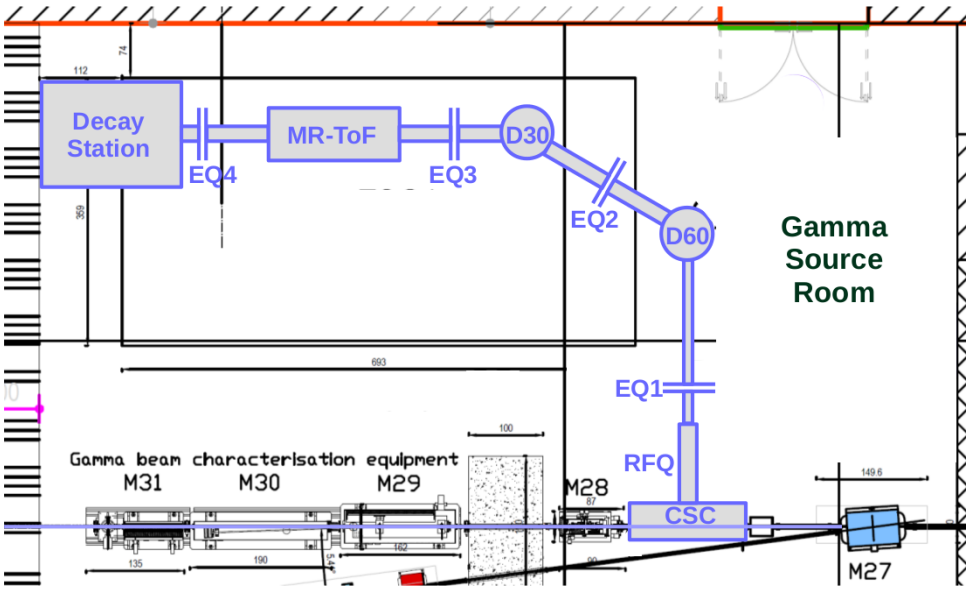


Fig. 47 − Top view of the placement of the whole IGISOL beam line in the GS room.

In order to meet these requirements, in collaboration with the National Institute for R&D in Electrical Engineering (ICPE-CA), Bucharest, a preliminary design of a HTS superconducting magnet for *g*-factor measurements was done. The general objective of the project consists in the realization of a dipole superconducting magnet that will produce a magnetic field above 2 T with a uniformity of $10^{-3}$ along the active area of the magnet.

The conceptual model is described in Fig. 48 and the projected characteristics of the magnet are:

- three channels with access to the central area (for the incident beam, for sample access, for the emitted radiation;
- $\phi$ = 20 mm diameter of the incident γ channel;
- $\phi$ = 6 mm diameter of the sample access channel;
- $\phi$ = 20 mm diameter of channels for the measurement of the γ decay;
- the dimensions of the useful field are around 80 $mm^3$;
- cooling without cryogenic agents (cryocooler use) by thermal conduction;
- winding with HTS superconducting materials.

To obtain a high and uniform magnetic field in the central area, where the *g*-factor target will be placed, a constructive solution was chosen, which is adequate to the conditions imposed by the technical requirements, namely a Helmholtz configuration of the superconducting coils. Since the superconducting coils require proper functioning conditions, especially at low temperatures, around 30 K, these must be introduced in a cryostat. Altogether, a cooling system of the superconducting winding must be designed, which will be done by a cryocooler through thermal conduction. To produce magnetic field, the coils will be powered by a DC programmable power source of 300 A.

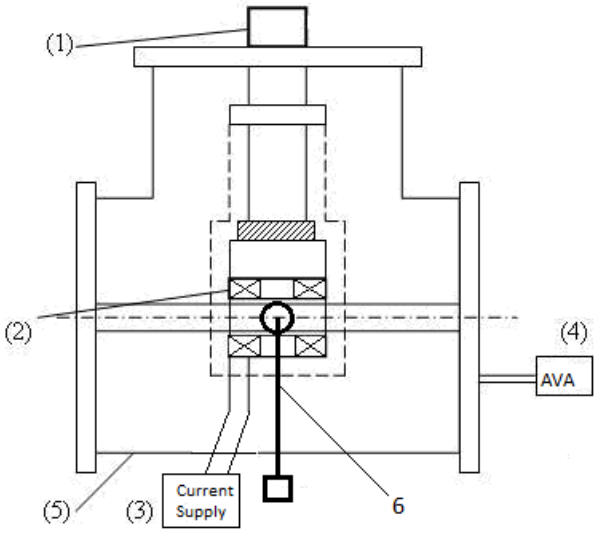


Fig. 48 − Conceptual model of HTS superconducting model. (1) Cryocooler; (2) Superconducting coils; (3) Programmable DC power supply 300 A; (4) Vacuum pump; (5) Coil cryostat; (6) Sample support.

Numerical modeling was performed for the conceptual design of the magnet. The results for the magnetic field for an optimized version with iron yoke, current of $I$ = 170 A and $N$ = 692 turns of the coils, are illustrated in Fig. 49.

The values, which were obtained in the calculations are: $B_{max}$= 3.18 T and the corresponding uniformity is $\Delta B/B$ ~ 0.22% in the aperture area.

For the isomeric states that require low magnetic fields, *e.g.* those with high *g*-factors compared to their lifetimes, we consider the use of a simple permanent magnet assembly as well (see Fig. 50). A similar one has already been constructed and used at ALTO, Orsay and has the following characteristics: (i) use of compact NdFeB permanent magnets with a return yoke of C-type; (ii) field in the center of

the target between 0.1 and 0.5 T, depending on the configuration; and (iii) field uniformity better than 0.5%.

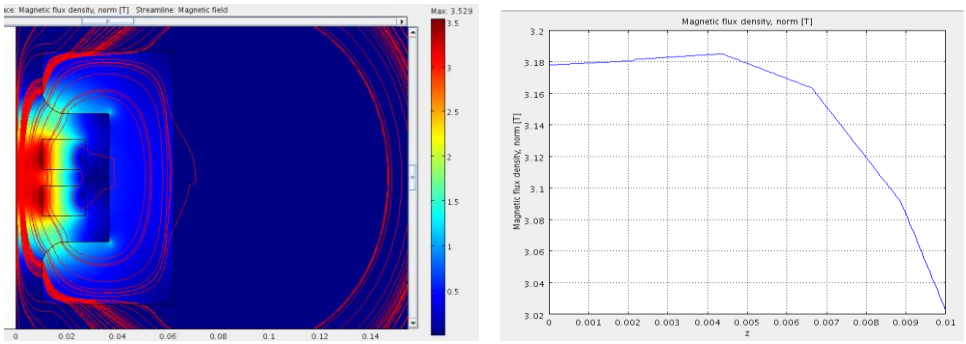


Fig. 49 − Left: The magnetic field and the field lines. Right: The magnetic flux density in the center of the magnet.

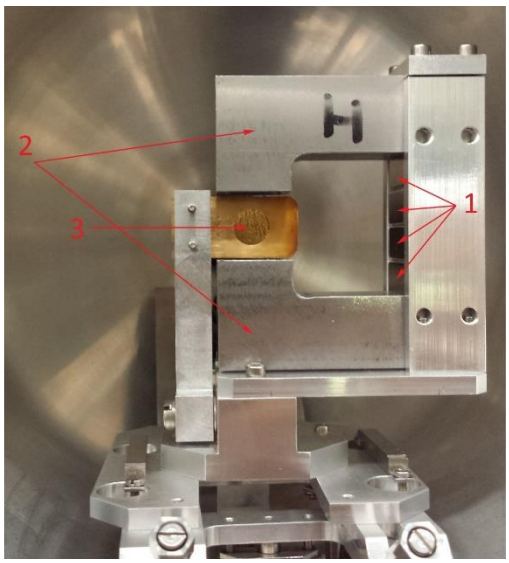


Fig. 50 − Permanent magnet assembly as already used at ALTO, Orsay. 1 – NdFeB magnets; 2 – return yoke; 3 – target.

The advantages of using a permanent magnet assembly are in its simplicity. However, in order to minimize any systematic effects it would be advantages to have the possibility to alternate the direction of the magnetic field. This can be done with a mechanical rotation of the magnet itself using a stepper motor.

The in-beam γ-ray spectroscopy setup will be realized in the E8 experimental hall. The alignment at the γ beam line will be done using the ELI-NP laser tracking system.

For nuclear moment experiments, a sandwich configuration of the targets will be used, arranged in alternative layers of target fissile material and host material. Less than 800 mg of $^{238}$U and less than 100 mg of $^{232}$Th target material will be used. The target geometry that will be used to obtain the fission yield and the number of fragments that would be implanted in respective host material is shown in Fig. 51. The thickness and the number of layers of target-host assembly will be optimized by maximizing the number of fragments that would be stopped in host and by utilizing the maximum γ beam. We plan to start with $^{238}$U target and ferromagnetic material Fe/Cu as a host. The study will be extended to thick targets ($UIr_2$) in which the fragments will be self implanted in the target itself. The $UIr_2$ alloy was found to be a good compound for th preparation of actinide targets in order to preserve the nuclear alignment with in the lifetime of isomeric states to be studied [58]. The alloy would also solve the problem of paramagnetic relaxation and radiation damage effects that oppose efforts in this field.

The target dimensions are decided on the basis of the collimated gamma beam spot at the target position. The simulation of the target, which will be positioned at 30 m from the interaction point in E8 and approximately 21 m from the ELI-NP collimator, has been done using the 5.8 MeV gamma beam source. The slit aperture of ELI-NP collimator is kept at 0.1 cm for the simulations. The simulation result of collimated gamma beam spot is shown in Fig. 52. In order to use 90% of the beam intensity, target dimension would be about 1 cm. The thickness of the target would be decided after the fission fragments yield simulation.

The in-beam γ-ray spectroscopy setup will be realized in the E8 experimental hall. The alignment at the γ beam line will be done using the ELI-NP laser tracking system.

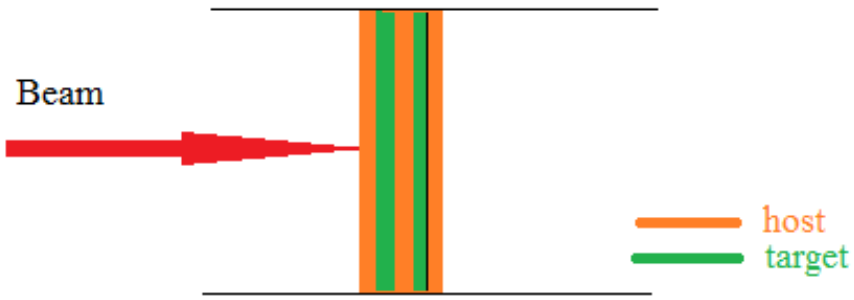


Fig. 51 − Target geometry that would be used for fission fragments yield calculations.

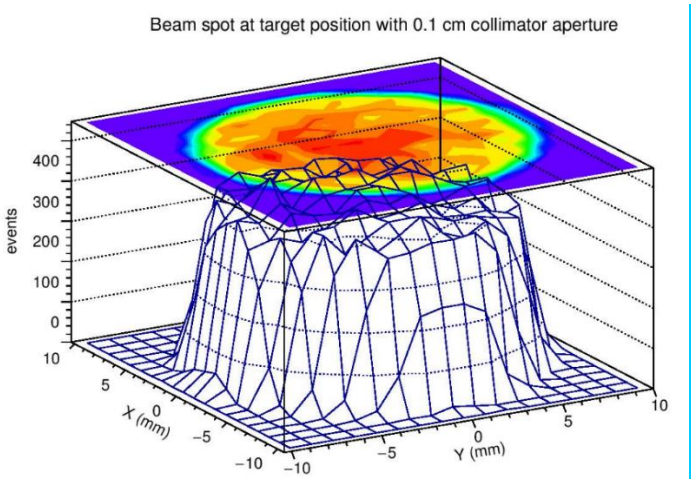


Fig. 52 − The collimated beam spot at the target position in E8.

### 3.5 Targets

All experiments, which are described in this TDR will use actinide targets which are not very thick, *i.e.* foils 5−10 μg/cm$^2$. In addition, in some cases they will be used in a sandwich-like configuration For example, a 10 μg/cm$^2$ $^{232}$Th foil on a 50 μg/cm$^2$ Cu backing, another $^{232}$Th layer on Cu and so on.

The collaboration has some stock of actinide targets, which will be sufficient to begin the experiments described in Sections 2.1 and 2.2. Highly sophisticated target assemblies need to be designed and manufactured for the experiments described in Sections 2.4 and 2.5. At present licenses for the production of actinide targets have the laboratories at the University of Mainz in Germany, PSI in Switzerland, the ANL and Lawrence Livermore National Laboratories (LLNA), USA and JAEA/JPark at Tokai, Japan. The possibility for target production at the Institute for Reference Materials and Measurements (IRMM) in Geel, Belgium, should be investigated, too.

## 4. ESTIMATE OF COUNT RATES/FEASIBILITY OF PROPOSED DEVICES

The estimated count rates for the different experiments and the proposed devices in this TDR are presented in Table 5.

### 4.1 High Efficiency Ionization Chamber and Si DSSD Detector System (ELI-BIC)

GEANT4 simulations yield a rate of 8 f/s for binary fission mass and isotope distribution measurements with the BIC array if we consider a flux of $8\cdot10^8$ γ/s (see Table A1 in Appendix A1) for pencil-type beams of bandwidth $\Delta E/E$ = 0.3−0.5% and an effective target thickness of 1 mg/cm$^2$. For $^{238}$U target foils with thickness 0.2-0.4 mg/cm$^2$, the release efficiency for the pair of fragments is high, around 70%, hence the signal out of the targets is about 6 pairs/s.

*Table 5*

Count rates of the photofission experiments at ELI-NP.

| Experiment | Device | Flux (γ/s) | Target | Events (f/s) | Signal |
|---|---|---|---|---|---|
| Transmission resonances | ELI−BIC array | $8\cdot10^8$ | 5 × (0.2−0.3) mg/cm$^2$ $^{232}$Th, $^{238}$U, etc. | 8 | 6 fission pairs/s |
| Transmission resonances | ELITHGEM array | $8\cdot10^8$ | 10 × 2 mg/cm$^2$ $^{232}$Th, $^{238}$U, etc. | $(0.3-2)\cdot10^3$ | $(0.6-6)\cdot10^2$ fission pairs/s |
| Ternary fission | ELITHGEM array | $8\cdot10^8$ | 10 × 2 mg/cm$^2$ $^{232}$Th, $^{238}$U, etc. | 0.6−4 | 0.03−0.2 events/s |
| IGISOL | Phase I | $5\cdot10^{10}$ | ≤ 800 mg $^{238}$U | $10^7$ | $4\cdot10^5$–$10^6$ ions/s |
| IGISOL | Phase II | $3\cdot10^{11}$ | 2–5 g $^{238}$U | $10^8$ | ≥ $10^7$ ions/s |
| In-beam γ spectroscopy | *g*-factor setup | ~ $10^{10}$ | ≤ 800 mg $^{238}$U or $^{238}UIr_2$ | $6\cdot10^4$ | $10^5$ γ/s |

### 4.2 Thick Gas Electron Multiplier based Detector System (ELITHGEM)

The simulated binary fission rate is $(0.3-2)\cdot10^3$ f/s, depending on the beam energy, and 0.6−4 f/s for ternary fission if we consider the same pencil beam ($\Delta E/E$ = 0.3−0.5%) with a flux of $8\cdot10^8$ γ/s, but a variable energy in the range 5−19 MeV, and a target thickness of 20 mg/cm$^2$. For a $^{238}$U target foil thickness of 1 μm, the pair release efficiency is 20−30%, hence the binary fission signal out of the target is $(0.6-6)\cdot10^2$ pairs/s. The ternary fission signal out of the target is more difficult to simulate since our GEANT4 model does not include this type of fission, and the release efficiency of the three ions from such an event has not been estimated. However, if we consider a similar efficiency of the array, as in the case of binary fission, the signal rate is about 0.03−0.2 events/s.

### 4.3 IGISOL beam line and beam transport to measurement stations

Isotopes, which will be produced as $10^{-3}$–$10^{-4}$ of the total fission yield, will reach the measurement stations of the IGISOL beamline at rates of $10^3$–$10^2$ ions/s, which is sufficient for *e.g.* β-decay studies. Isotopes, which are produced as $10^{-5}$, will reach the measurement stations at rates of 10 ions/s, which is the limit for β-decay studies. These rate estimates are done taking into account a fission yield of $10^7$ f/s (see Section 2.3) and an expected ion-survival probability throughout the IGISOL of about 10%.

As discussed in Section 3.3.1, the fission yield is considered for day-one experiments. This is based on the estimate that the total flux will be $5\cdot10^{10}$ γ/s. After optimization of the ELI-NP GBS for wide bandwidth beams, an increase with a factor of two or more will be possible. The setup which is considered is based on the assumption that less than 800 mg of $^{238}$U target material will be used. Only 30% of the beam interacts with such a target. The efficiency of the CSC is taken, based on the existing GSI CSC cell. It can be improved by at least a factor of two. After day one, we estimate that isotopes that are produced at rates of $10^{-6}$ of the total yield will be measured in β decay. If a MR-ToF mass separator is constructed, mass measurements of isotopes, which are produced are extracted at rates of 5 ions/h will be possible. This will shift the experimental limit at ELI-NP further away from the line of β stability.

With the optimization of the ELI-NP IGISOL facility, the fission yield will be possible to be increased and reach $10^8$ f/s. This will allow measurements further away of stability. The expected isotope yields at ELI-NP, considering the highest possible fission rate, are presented in Fig. 53. The solid black line indicates isotopes which will be delivered at rates of $10^2$ ions/s, and the dashed line is set at rates of 1 ion/s. The comparison between the expected isotope yields delivered by the IGISOL beamline in the two phases of the ELI-NP facility is shown in Fig. 40 (for Molybdenum) and in Fig. 41 (for Cerium) in blue.

### 4.4 In-beam high-resolution gamma spectroscopy set up

Using a gamma beam with an energy 5−7 MeV and a $^{238}$U target with a total mass of 800 mg, our simulations generate $6\cdot10^4$ f/s. Considering that each fission fragment evaporates on average 6−7 photons, we get about $4\cdot10^5$ γ/s emitted from the targets. On the other hand, previous measurements using Ge arrays, like those done with the EXIL spectrometer at the Institute Laue-Langevin (ILL) facility in Grenoble, France, suggest a limit of about $10^5$ γ/s in the rate capability of these devices.

Hence, based on the experience with the EXIL spectrometer and having in mind that the efficiency of the ELIADE array is around 10%, it is possible to carry

out in-beam spectroscopy studies of fission fragments which are produced as $10^{-3}$–$10^{-4}$ of the total fission yield.

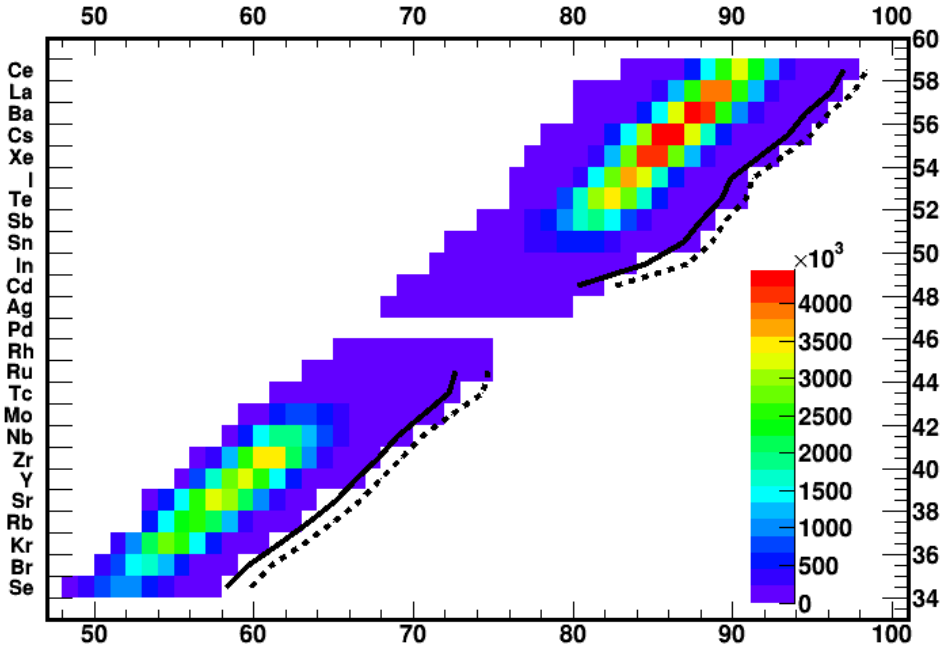


Fig. 53 – Estimated photofission yield distribution in phase II of the ELI-NP facility: the fission yields from [27] were scaled to a total of $10^8$ f/s. The full lines show the 100 fragments per second contours and the dashed lines show the 1 fragments per second contours.

## 5 SPECIFIC NEEDS AND UTILITIES, TRANSVERSAL NEEDS

### 5.1 Infrastructure needed from ELI–NP

**Mechanics of the detector support.** Movable tables, allowing remote control of the detector positioning on the beam line and aligning it along the beam axis, should be designed. The detector positioning will use the ELI-NP tracking system. Dedicated alignment system procedures should be defined for each instrument.

**Collimators and shielding materials.** The different experimental setups will require collimation and shielding, which should be designed according to the requirements in each case.

**Gas supply system.** Photofission experiments at ELI-NP require a gas supply system, which should deliver the needed gases and gas mixtures for the ELI-BIC and ELITHGEM detector arrays, as well as a He gas supply system for the CSC of the

IGISOL facility. These systems should include units for gas storage, gas circulation and, if needed, gas re-cycling and purification.

**Cryogenic laboratory**. In the first stage of the ELI-NP project for photofission experiments, the support of the Mechanics workshop will be used. For the design and the construction of the devices of IGISOL facility, the existing infrastructure of the partners will be used. In the second phase of the project, when mounting the IGISOL beam line at ELI-NP, a cryogenic laboratory will be needed. This can coincide with the extension of the ELI-NP experimental area towards the Reactor building.

**Control system.** The E8 experimental area of the ELI-NP Laboratory building will be partially dedicated to photofission experiments, since the ELI-BIC and ELITHGEM detector arrays, as well as the ELIADE *g*-factor measurement setup, will be mounted there at the high-energy γ beam line. The ELIADE detectors and data acquisition system (DAQ) are described in the GBS TDR1 "Nuclear Resonance Fluorescence Experiments at ELI-NP". Note that there is a suggestion the ELI-BIC spectrometer to be mounted in the E7 area, where the experiments will benefit from the smaller size of the γ beam.

The ELI-NP demonstrator of the IGISOL beam line will be mounted in the Gamma Source (GS) and E1 areas. These areas will have the experiment monitoring and control systems architecture similar to the GBS and Gamma Beam Delivery and Diagnostics (GBDD) control systems, which are described in the GBS TDR0 "Gamma Beam Delivery and Diagnostics". The architecture is based on the Experimental Physics and Industrial Control System (EPICS) which will permit local distributed control of the equipment and additional clients to remotely supervise/control the experiment. This solution will allow a standardization of the control systems inside ELI-NP, while providing easy maintenance, better security, better logging and interfacing methods between the experimental areas, GBS and GBDD.

A dedicated UserRoom platform will be used to remotely control the equipment from outside the E8/GS/E1 areas as the experiment is running. An EPICS framework will be developed to link the experimental area to the UserRoom platform using a dedicated client-server architecture that will allow maintenance and upgrades to be performed without interacting with other systems.

A data storage server will be available for short term experimental data saving and this shall benefit in general from dedicated data busses, separated from the client-server EPICS architecture that controls and monitors the equipment itself, in order to achieve the highest data throughput.

Dedicated EPICS servers are envisaged to interface the experimental equipment listed in Table 6.

Each of the above equipment will have a Human-Machine Interface able to locally, from inside the interaction area, or remotely, from the User Room, monitor and control the parameters needed to run the equipment and the experiment. For

equipment where the Application Programing Interface (API) is not provided, or the required development time does not fit into the general schedule, the link between the User Room and the experimental area will be made using remote desktop, or similar, and by using their proprietary software. The UserRoom platform will also provide, through the EPICS architecture, information to the user regarding the GBS parameters and GBDD configuration. The GBS and GBDD parameters will be controlled from the Gamma control room by the operators from personnel and machine safety reasons.

In addition, there are few other requirements, which will be necessary for the photofission experiments at ELI-NP: (i) electrical power of high stability; (ii) cable ducts; (iii) disk storage; (iv) fast internet transmission lines; (v) Central Processing Unit (CPU) for off-line data processing; (vi) beam-energy profile and beam-intensity information, integrated into the DAQ.

*Table 6*

EPICS control interfaces for the photofission experiments.

| **Detector type setup** | **System to be interfaced with EPICS** | **Location of the system** |
|---|---|---|
| ELI-BIC and ELITHGEM arrays | Common gas-circulation systems; and vacuum monitoring system | E8 (or E7) |
| ELI-BIC array | High-Voltage system | E8 (or E7) |
| ELI-BIC and ELITHGEM arrays | Common DAQ system | E8 (or E7) |
| IGISOL beam line | All the necessary systems composing the IGISOL line (Collimator, CSC, RFQ, Quadrupole magnet, vacuum, etc.) | Gamma Source |
| IGISOL beam line measurement stations | DAQ system | Gamma Source or E1 |
| ELIADE *g*-factor measurements | ELIADE DAQ system *g*-factor magnet control | E8 |

## 6. SAFETY REQUIREMENTS

The proposed project for photofission experiments involves the usage of nuclear material only with very limited activity, well below the activity limits of UN 2910 “Radioactive material, excepted package-limited quantity of material”,

*e.g.* 25−30 mg $^{232}$Th, $^{235}$U. $^{238}$U is discussed below. A low activity (5 KBq) $^{252}$Cf fission source is also needed for the test of the THGEM and the BIC arrays.

The filling gas of the THGEM detector array and the ionization chamber is isobutane and P10, respectively. Both gases are flammable thus needs special treatment by using gas leakage monitors/detectors.

The IGISOL facility will operate at a rate of around $10^7$ f/s, which will result in creating a neutron field of the same order. The day-one target which will be used in this experiment will be 800 mg $^{238}$U.

For the in-beam γ-ray spectroscopy experiments, multilayered actinide targets will be used, the actinide material being of the order of 800 mg $^{238}$U.

## 7. COLLABORATIONS

For the preparation of this TDR and for designing the different instruments and beamlines which were described in the TDR, memorandums of Understanding (MoUs) were signed with:

1. Magyar Tudományos Akadémia Atommagkutató Intézet (MTA ATOMKI), Debrecen, Hungary
2. GSI Helmholtzzentrum für Schwerionenforschung GmbH, Darmstadt, Germany
3. Justus-Liebig Universitat, Giessen, Germany
4. Institut de Physique Nucléaire, Orsay, France
5. Manipal University, India
6. Akdeniz University, Antalya, Turkey
7. Centre of Nuclear Physics, Institute of Nuclear Physics, Vietnam Academy of Science and Technology, Hanoi, Vietnam
8. Institutul National de Cercetare Dezvoltare pentru Inginerie Electrica ICPE-CA, Bucharest, Romania.

These MoUs established a framework for cooperation between the parties regarding the implementation of ELI-NP and its scientific program.

## 8. CONCLUSION

At the ELI-NP facility, a GBS with beyond state-of-the-art performance is under construction. It will deliver tunable, brilliant, narrow-bandwidth, polarized γ beams with energies up to 20 MeV. The superior parameters of the GBS of the new

laboratory has been used to define a photofission research program, which addresses key questions of modern nuclear physics and will allow the exploration of new frontiers in science. For the realization of this scientific program, several innovative detector systems have been proposed within this TDR and their conceptual design has been discussed. A large scientific community has been involved and participates in the development of the photofission scientific program, the definition of day-one experiments and the design and construction of the different detector arrays. These experiments will be carried out at the high-energy γ beamline of the ELI-NP GBS, and first experiments are expected to take place in 2018.

***Acknowledgements.*** This work is supported by the Project Extreme Light Infrastructure - Nuclear Physics (ELI-NP) - Phase I, a project co-financed by the Romanian Government and European Union through the European Regional Development Fund. A. Krasznahorkay and L. Csige acknowledge support from the Hungarian OTKA foundation under grant no. K106035. P.V. Cuong acknowledges the support of the Vietnam National Foundation for Science and Technology Development (NAFOSTED) under grant no. 103.04-2014.29.

## APPENDIX A: THE ELI-NP GAMMA BEAM RATES

In Table A1 are listed the γ beam parameters at four specific gamma energies, as published by the provider of the ELI-NP GBS, namely for $E$ = 2.0, 3.45, 9.87, 19.5 MeV (upper side of Table 63 in Ref. [24]).

In Table A2 are listed the parameters of the gamma beam system, which will become operational at ELI-NP [59]. The main parameter in this table that is used in rate calculations, described throughout this report, is the time-averaged spectral density at peak energy $F = (0.8–4.0)\cdot 10^4$ photons/(s·eV), corresponding to a gamma energy range $E$ = 0.2−19.5 MeV.

*Table A1*

Properties of the ELI-NP γ beam at four energies [24]. All quantities are given as rms.

| | Low Energy Interaction | Low Energy Interaction | High Energy Interaction | High Energy Interaction |
|---|---|---|---|---|
| Energy (MeV) | 2.00 | 3.45 | 9.87 | 19.5 |
| Spectral Density (ph/sec/eV) | 39,760 | 21,840 | 16,860 | 8,400 |
| Bandwidth (%) | 0.5 | 0.5 | 0.5 | 0.5 |
| Photons/s within FWHM | $4.0\cdot 10^8$ | $3.7\cdot 10^8$ | $8.3\cdot 10^8$ | $8.1\cdot 10^8$ |

Figure A1 shows the energy dependence of the time-averaged spectral density using the data from Table 1.

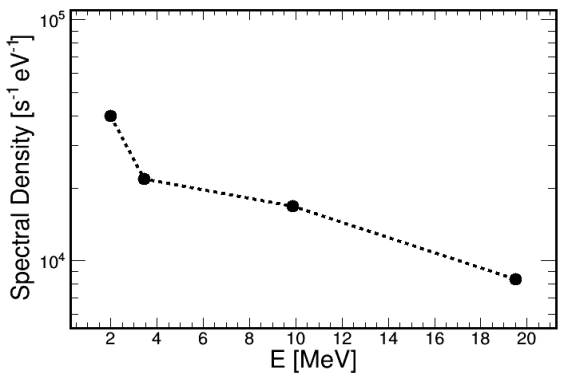


Fig. A1 − Energy dependence of the gamma source spectral density.

*Table A2*

Specifications of the gamma beam produced by the complete GBS [59]

| Quantity | Symbol | Units | Specification |
|---|---|---|---|
| Minimum Photon Energy | $E_\gamma$ | MeV | 0.2 |
| Maximum Photon Energy | $E_\gamma$ | MeV | 19.5 |
| Tunability of the photon energy (b) | | | continuously variable |
| Linear polarization of the gamma ray beam (b) | $P_\gamma$ | % | ≥99 |
| Frequency of the gamma ray macropulses (b) | $\Omega_{\gamma,M}$ | Hz | 100 |
| Number of gamma ray micropulses per macropulse (b) | | | 32 |
| Micropulse-to-micropulse separation (b) | | ns | 16 |
| Divergence (b) | $\Delta\theta$ | rad | $(0.25–2.0)\cdot10^{-4}$ |
| Source rms diameter (b) | | m | $(0.01–0.03)\cdot10^{-3}$ |
| Average diametral FHWM of beam spot (a, b) | $\sigma_r$ | m | $\leq1.0\cdot10^{-3}$ |
| Average bandwidth of the gamma ray beam (a, b, c) | $W$ | | $\leq5.0\cdot10^{-3}$ |
| Time-average spectral density at the peak energy (d) | $F$ | 1/(s·eV) | $(0.8–4.0)\cdot10^{4}$ |
| Time-average brilliance at peak energy (a, d) | $B_{av}$ | $1/(s\cdot mm^2\cdot mrad^2\cdot 0.1\%BW)$ | $\geq1.0\cdot10^{13}$ |
| Peak brilliance at peak energy (a, d) | $B$ | $1/(s\cdot mm^2\cdot mrad^2\cdot 0.1\%BW)$ | $10^{20}–10^{23}$ |
| Average spectral off-peak gamma ray background density (a, b, c) | $\Phi_{\gamma,bkgr}$ | 1/(s·eV) | $\leq1.0\cdot10^{-2}$ |

a) at reference-point located at approximately 10 m downstream of the Compton collision point for gamma-ray production
b) for all gamma-ray energies between minimum and maximum photon energy
c) at all points within the FWHM of the beam spot
d) at gamma-ray energy of 2 MeV (for the first part of the electron accelerator) and 10 MeV (for the full electron accelerator)

The γ rate $R$ at a given energy of the γ beam $E_\gamma$ is $R(E_\gamma) = F(E_\gamma)\cdot E_\gamma\cdot BW$, where $F(E_\gamma)$ is the time-averaged spectral density at the peak energy $E_\gamma$ and $BW$ is the beam bandwidth. For example, at $E_\gamma$ = 9.87 MeV, we obtain:

$$8.3\cdot10^{8}\ [\mathrm{ph/s}] = 16860\ [\mathrm{ph/(s\cdot eV)}] \cdot 9.87\cdot10^{6}\ [\mathrm{eV}] \cdot 0.5\cdot10^{-2}.$$

When computing the integrated rate $R_{tot}$ over the entire energy spectrum of the gamma beam, $E_{tot}$, the bandwidth $BW$ integrates out when summing over all energies, as:

$$R_{tot} = F(E_\gamma)\cdot E_{tot} \approx (0.8–4.0)\cdot 10^4 \text{ [ph/(s·eV)]}\cdot 2\cdot 10^7 \text{ [eV]} \approx 2\cdot(0.8–4.0)\cdot 10^{11} \text{ [ph/s]}$$

In the calculations $F(E_\gamma) \approx 1.6\cdot 10^4$ ph/(s·eV) was used, which was evaluated from Fig. A1 at the mean energy $<E_\gamma> \approx 9.2$ MeV of the high energy γ beam source (see Fig. 6). Thus, the total γ flux delivered by the high energy γ beam source is $R_{tot} = 3.2\cdot 10^{11}$ γ/s. However, a more conservative value was accepted for day-one experiments, $R_{tot} = 5\cdot 10^{10}$ γ/s.

## APPENDIX B: PRODUCTION RATES COMPARISON AND EXTRAPOLATION

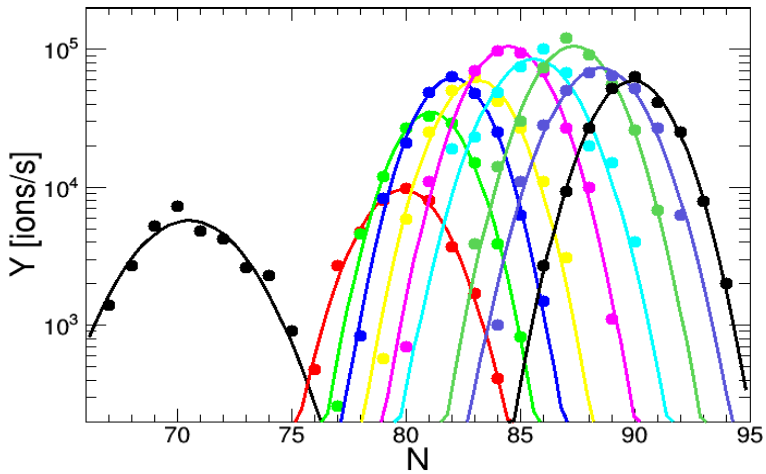


Fig. B1 − Gaussian fits of production rates at CARIBU, for elements with high-$Z$ as a function of $N$, Cd (black), Sn (red), Sb (light green), Te (blue), I (yellow), Xe (pink), Cs (cyan), Ba (green), La (light blue) and Ce (black).

In this section, the approach to compare the production rates for IGISOL-4 (Fig. 36), CARIBU (Fig. 35) and photofission (Fig. 9), is described. Based on this detailed comparison, the photofission production rates at ELI-NP to elements with higher atomic number, $Z$, up to Ce were extrapolated. In Fig. B1 Gaussian fits of CARIBU production rates as a function of the neutron number, $N$, are displayed for high-$Z$ elements, Cd ($Z$ = 48), Sn ($Z$ = 50), Sb ($Z$ = 51), Te ($Z$ = 52), I ($Z$ = 53), Xe ($Z$ = 54), Cs ($Z$ = 55), Ba ($Z$ = 56), La ($Z$ = 57) and Ce ($Z$ = 58). Note that for In ($Z$ = 49) only three data points were reported, and it was not used in the fits.

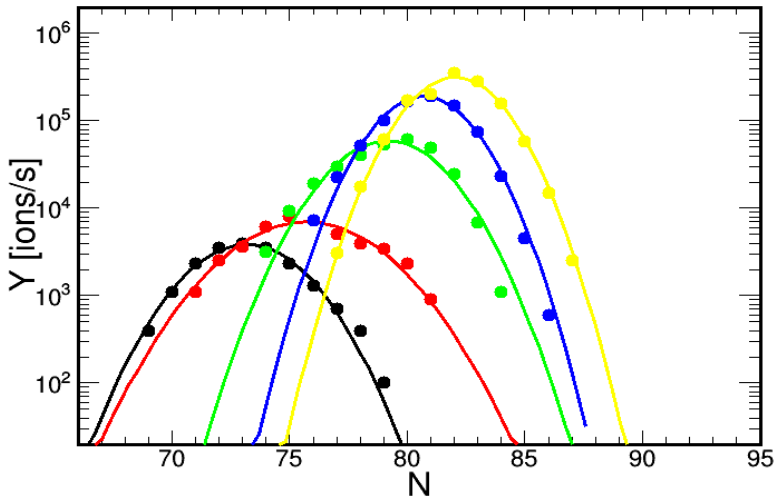


Fig. B2 − Gaussian fits to N-dependence of production rates for photofission, for the measured high-Z elements [27], Cd (black), In (red), Sn (green), Sb (blue) and Te (yellow).

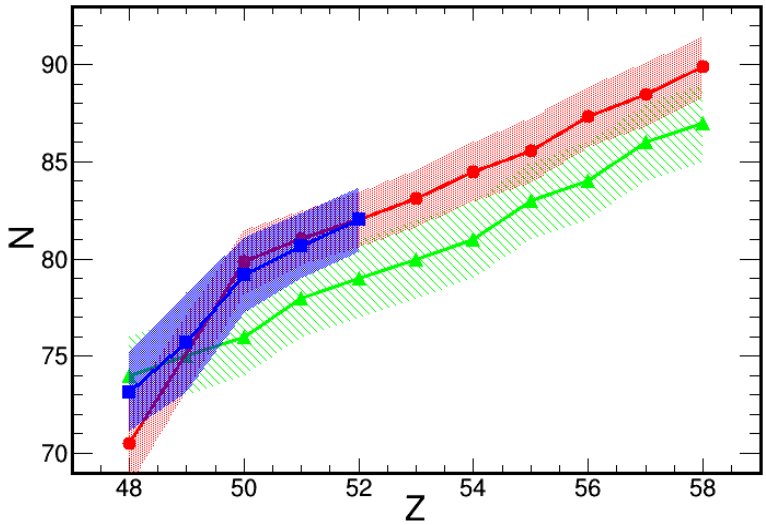


Fig. B3 − Gaussian mean (lines with symbols) and σ (hashed areas) for elements from Cd to Ce. The IGISOL-4 data is shown with green (triangles), the CARIBU data is shown with red (circles) and the photofission data is shown with blue (squares).

In Fig. B2 Gaussian fits of the photofission rate as a function of the neutron number, *N*, for the highest-*Z* elements, which were measured [27], are displayed for Cd ($Z = 48$), In ($Z = 49$), Sn ($Z = 50$), Sb ($Z = 51$) and Te ($Z = 52$).

In Fig. B3 Gaussian mean *N* values are presented as a function of the atomic number *Z* (see the explanations in the figure caption). It is demonstrated that,

wherever photofission data is available, the dependence follows the data obtained in spontaneous fission (CARIBU data).

In Fig. B4 the Gaussian amplitudes of the data fits for the isotope yields for elements from Cd to Ce, which are displayed in Figs. B1 and B2, are plotted. The red full line is a fit with a 3rd degree polynomial to high-*Z* CARIBU data. The blue dashed line is a shift of the red line, such that it matches the highest-*Z* data point of the photofission data set.

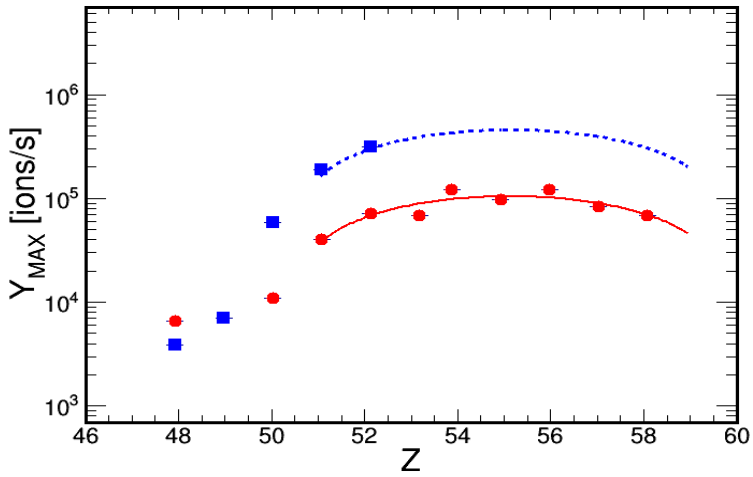


Fig. B4 − Gaussian amplitudes for the isotope yields from Cd to Ce. The CARIBU data is shown with red circles and the photofission data is shown with blue squares. The red line is a polynomial fit of the CARIBU data. The blue dashed line is the red line matched to the data point at $Z = 52$.

## APPENDIX C: GEANT4 SIMULATIONS OF THE CRYOGENIC STOPPING CELL

For the study of the target release efficiency, two target setups were used: setup A, consisting of 27 targets with 10 μm thickness, and setup B, consisting of 39 targets with 7 μm thickness. All other parameters were kept the same, the targets were tilt at a 10° angle with respect to the gamma beam, the distance between the centers of two adjacent targets is 3.5 cm, the targets are of 5 mm width and 2.9 cm length. The target number is set such that the same quantity of $^{238}$U, about 800 mg, is used in both setups. Hence, the number of fragments produced by photofission is the same, within statistical fluctuations. To account for these statistical fluctuations, each setup has been simulated three times, with different seeds for the random number generator. These targets are then placed in He gas within a CSC, as detailed in Section 3.3.1.

*Table C1*

Target release efficiency for two target assemblies with target thicknesses of 7 and 10 μm.

| Thickness | Fissions | Ions Produced | Ions Released | Release Efficiency |
|---|---|---|---|---|
| (A.1) 10 μm | 725 | 1450 | 137 | 9.5% |
| (A.2) 10 μm | 731 | 1462 | 178 | 12.2% |
| (A.3) 10 μm | 746 | 1492 | 154 | 10.3% |
| (B.1) 7 μm | 706 | 1412 | 214 | 15.2% |
| (B.2) 7 μm | 723 | 1446 | 228 | 15.8% |
| (B.3) 7 μm | 734 | 1468 | 241 | 16.4% |

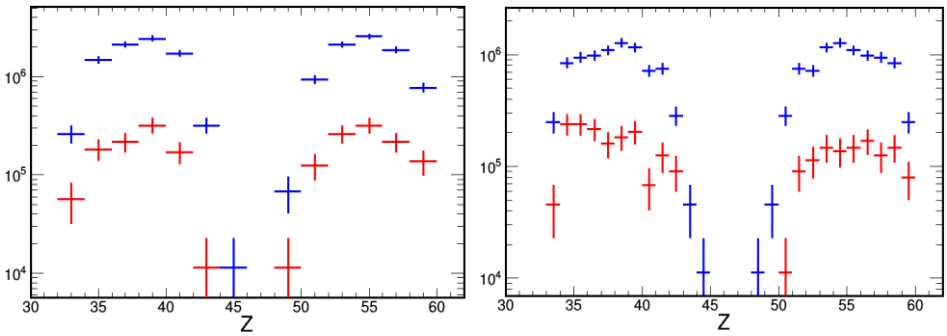


Fig. C1 − Atomic number distributions of the produced ions (blue) and released ions (red) for $^{238}$U targets with thickness 7 μm (left) and 10 μm (right).

The resulting values for the number of photofission events, the number of produced fragments in fission, the number of fragments released from the targets, and the resulting target release efficiency are presented in Table C1.

The average target release efficiency is 11% for the setup A, consisting of 10 μm targets, and 16% for setup B, consisting of 7 μm targets. However, a more relevant quantity is the absolute number of released ions. For the same target mass, or number of produced ions as above, a 50% increase in efficiency is reflected by a 50% increase in the number of released ions. This comes at a cost, an increase in the total length $L$ of the gas cell, which is defined as $L = N{\cdot}D + 2d = N{\cdot}3.5 + 20$ [cm], where $D$ is the inter-target distance, $N$ is the number of targets and $d$ is the distance to the cell walls. Hence, $L_B/L_A = 153/111 = 1.38$. In the first phase of implementation of the IGISOL facility at ELI-NP, the CSC length is limited to a little above 1 m. Rescaling the number of released ions by the ratio of the number of targets $N_A/N_B = 27/39 = 0.69$ cancels most of the benefits in the increase in the release efficiency, the number of released ions increases only by 4%. A more detailed study, which combines simultaneously several parameters of the geometry of the target assembly at fixed total length $L$ of the CSC, is needed to find an optimal solution. For example,

the 2.9 cm target length covers the FWHM of about 2.36σ of the beam. However, it can be reduced to 1.5−2σ, providing optimal target burning. In this way thinner targets can be used, to keep the same total mass.

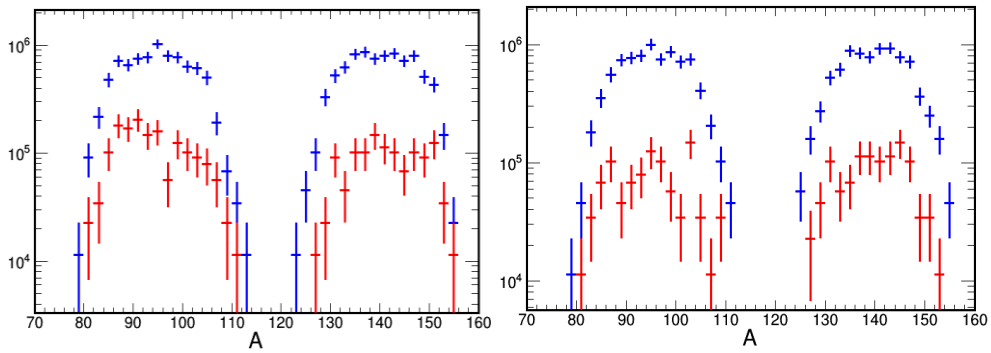


Fig. C2 − Atomic mass distributions of the produced ions (blue) and released ions (red) for $^{238}$U targets with thickness 7 μm (left) and 10 μm (right).

Next, the properties of the released ions are discussed. Figs. C1 and C2 display the distributions of the atomic mass and charge numbers of the produced ions (blue) and released ions (red) for both values of the target thickness. Apart from a reduction in total yields, there is no other change in the distributions.

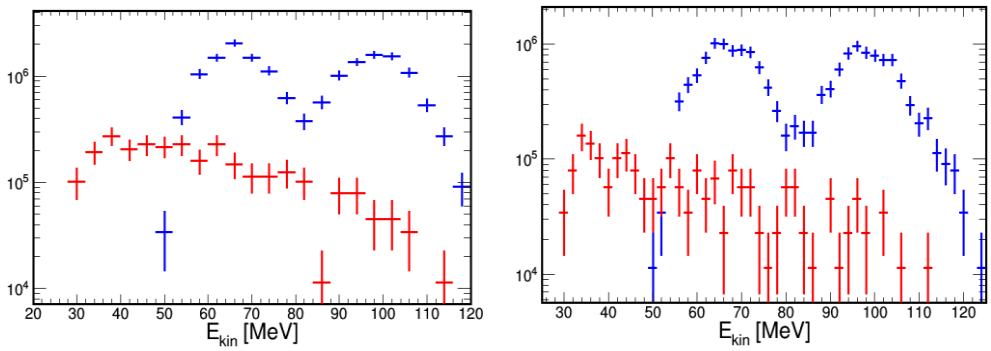


Fig. C3 − Kinetic energy distributions of the produced ions (blue) and released ions (red) for $^{238}$U target thickness 7 μm (left) and 10 μm (right).

In Fig. C3 the corresponding kinetic energy distributions are presented. They reveal a significant change in shape, mean value and spread. This can be seen also in the two-dimensional plots from Fig. C4. All distributions have been normalized to the total rate of the high-energy γ-beam source, as discussed in Appendix A, such that they represent ions per second, produced or released from the targets.

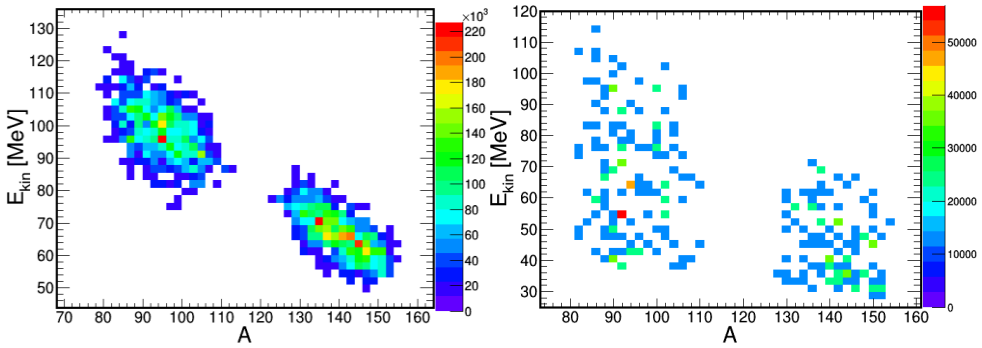


Fig. C4 − 2D plots of kinetic energy *vs.* atomic mass distributions of the produced ions (left) and released ions (right) for $^{238}$U target with thickness 7 μm.

As discussed in Section 2.3, GEANT4 simulations are done within two independent approaches [25, 26], which use different implementations of the photofission process. As an example, in Fig. C5 the same calculation, as the one of Fig. C4, which was carried out with the program of P. V. Cuong [26], is shown.

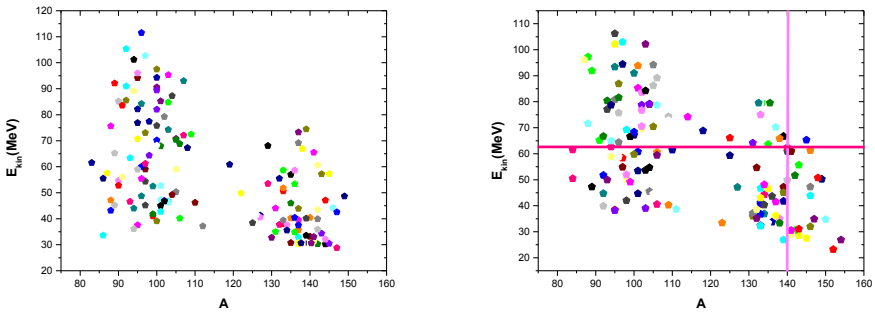


Fig. C5 − 2D plot of the kinetic energy *vs.* atomic mass distributions of released ions for $^{238}$U target with thickness 7 μm with the GEANT4 code of P. V. Cuong [26].

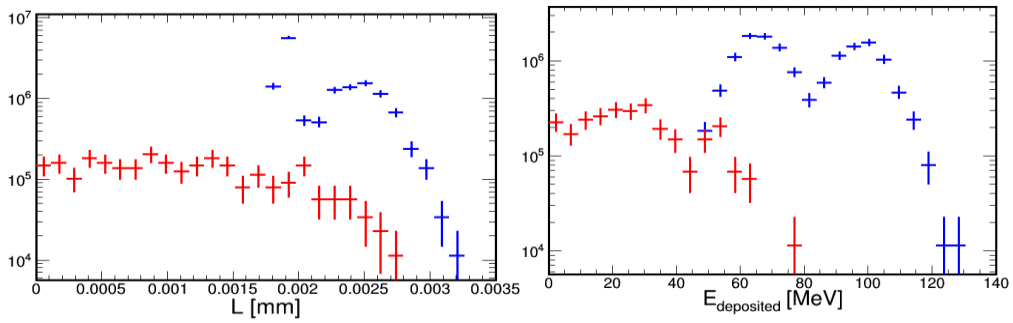


Fig. C6 – Left: Path length in the 7 μm target of the produced ions (blue) and the released ions (red). Right: Energy deposited in the 7 μm target by the produced ions (blue) and the released ions (red).

*Table C2*

The mean and rms of the kinetic energy distributions of photofission fragments.

| Target | Distribution | $<E_{kin}>$ | RMS($E_{kin}$) |
|---|---|---|---|
| 10 μm | produced ions | 82.8 MeV | 17.2 MeV |
| | released ions | 56.4 MeV | 20.0 MeV |
| 7 μm | produced ions | 82.5 MeV | 17.6 MeV |
| | released ions | 58.0 MeV | 19.5 MeV |

The parameters of the kinetic energy distributions of produced and released ions for the two target setups are summarized in Table C2. It demonstrates that ions lose on average about 26 MeV in the $^{238}$U target, with a very weak dependence on its thickness in the range considered here.

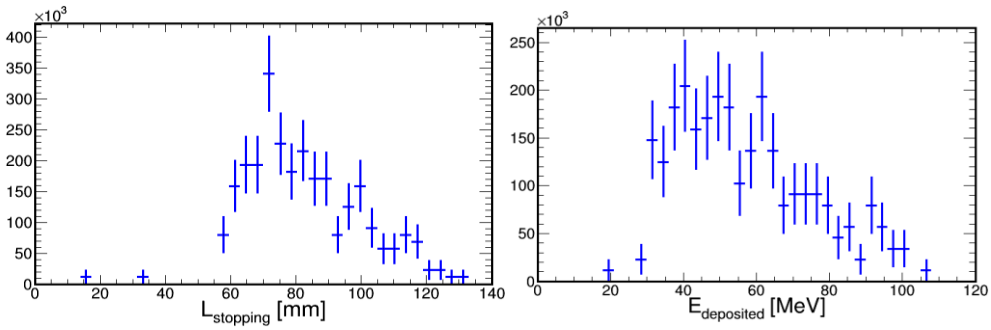


Fig. C7 – Stopping length (left) and deposited energy (right) in the cell He gas by the released ions.

Next, the stopping of the ions, which are released from the targets, in the CSC He gas is studied. The path length and the deposited energy of all produced fragments are shown in Fig. C6 for the 7 μm target assembly (in blue). It is demonstrated that

the fragments with the highest energy of 120 MeV (see Fig. C3) lose all their energy and stop in about 3.5 μm of $^{238}$U. The subset of ions that succeed to leave the target, the released ions, are plotted in red. Their path length distribution is rather flat up to about 2 μm and then starts to drop, presumably having a maximum around 3.5 μm, where the calculations run out of statistics. The released ions lose about a third of their energy in the target, in agreement with the values from Table C2. Note that the red distribution is a subset of the blue one, and it overlaps with the blue one at small values.

*Table C3*

Parameters of the ion stopping for the 7 μm target assembly.

| Distribution | Produced ions in target | Released ions in target | Released ion in cell gas |
|---|---|---|---|
| $<E_{\mathrm{dep}}>$ | 73.0 MeV | 27.5 MeV | 56.9 MeV |
| RMS($E_{\mathrm{dep}}$) | 26.5 MeV | 16.5 MeV | 18.6 MeV |
| $<L>$ | 2.0 μm | 1.1 μm | 82.7 mm |
| RMS($L$) | 0.57 μm | 0.68 μm | 17.6 mm |

In Fig. C7 the stopping length (left) and the deposited energy (right) of the ions, which are released in the He gas of the CSC, are shown for the 7 μm target assembly. These parameters provide crucial information for the design of the CSC: (i) the inner radius of the CSC needs to be about 12 cm to stop most, more than 95%, of the ions, which are released in the gas; (ii) the peak of the deposited energy of the ions in the stopping process is at about 7 cm away from the targets, while the other component of energy deposition via ionization in the gas, the $e^+e^-$-induced ionization, has its peak close to the targets (see Fig. 30); (iii) the rate of energy deposition in the gas by the released ions is:

$$<E_{dep}>\cdot<N_{rel}>/(L\cdot w\cdot d)\approx 15\ \mathrm{GeV}/(\mathrm{cm}^3\cdot\mathrm{s})$$

where $<E_{dep}> \approx 57$ MeV (see the right plot in Fig. C7) is the mean deposited energy, $L = 155$ cm is the length of the 7 μm target assembly, $w = 25$ cm is twice the stopping length (see above), $d \approx 2$ cm is the spread of the profile of the released ions (see the left plot of Fig. C7), and $<N_{rel}> \approx 2.1\cdot10^6$ ions/s is the average rate of released ions for the 7 μm target foils. It is estimated by multiplying the mean number of released ions, from Table C1, by the normalization factor that scales the number of γ-rays used in the simulation to the total rate of the high-energy γ beam source (see Appendix A).

The same value is obtained for the 10 μm target assembly. In this case both $L$ and $<N_{\mathrm{rel}}>$ decrease. It should be noted that the ion-parameter distributions for the 10 μm setup look very similar to those for the 7 μm setup, which are plotted in Figs. C6 and C7, having about 50% less counts. The main parameters of the ion-stopping distributions for the two target assemblies are summarized in Tables C3 and C4.

*Table C4*

Parameters of the ion stopping for the 10 μm target assembly.

| Distribution | Produced ions in target | Released ions in target | Released ions in cell gas |
|---|---|---|---|
| $<E_{dep}>$ | 75.9 MeV | 25.3 MeV | 55.5 MeV |
| RMS($E_{dep}$) | 25.4 MeV | 15.0 MeV | 19.0 MeV |
| $<L>$ | 2.0 μm | 1.0 μm | 81.2 mm |
| RMS($L$) | 0.51 μm | 0.62 μm | 17.7 mm |

## REFERENCES


1. V.M. Strutinsky, Nucl. Phys. A **95**, 420 (1967).
2. B.B. Back *et al.*, Phys. Rev. Lett. **28**, 1707 (1972).
3. P. Möller, S.G. Nilsson and R.K. Sheline, Phys. Lett. B **40**, 329 (1972).
4. L. Csige *et al.*, Phys. Rev. C **87**, 04432 (2013).
5. M. Kowal and J. Skalski, Phys. Rev. C **85**, 061302 (2012).
6. P. Jachimowicz, M. Kowal and J. Skalski, Phys. Rev. C **87**, 044308 (2013).
7. S. Cwiok *et al.*, Phys. Lett. B **322**, 304 (1994).
8. A. Krasznahorkay, "*Handbook of Nuclear Chemistry*" vol. 1, editors A. Vertes *et al.*, Springer Verlag, Berlin, p. 281 (2011).
9. P. G. Thirolf *et al.*, EPJ Web of Conferences **38**, 08001 (2012).
10. D .L. Hill and J. A. Wheeler, Phys. Rev. **89**, 1102 (1953).
11. http://www.nndc.bnl.gov/empire/
12. http://www.talys.eu/
13. G. Bellia *et al.*, Z. Phys. A **314**, 43 (1983).
14. C. D. Bowman *et al.*, Phys. Rev. C **17**, 1086 (1978).
15. C.K. Shalem *et al.*, Nucl. Instr. Meth. A **558**, 468 (2006).
16. C. Budtz-Jorgensen *et al.*, Nucl. Instr. Meth. A **258**, 209 (1987).
17. W. Neubert, Nucl. Instr. Meth. A **237**, 535 (1985).
18. P. Heeg *et al.*, Nucl. Instr. Meth. A **278**, 452 (1989).
19. F. Goennenwein, EPJ Web of Conferences **62,** 07002 (2013).
20. V. A. Rubchenya *et al.*, Int. J. of Mod. Phys. E **18,** 830 (2009).
21. G. Savard *et al.*, Nucl. Instr. Meth. B **266**, 4086 (2008).
22. M. Pfutzner *et al.*, Rev. Mod. Phys. **84**, 567 (2012).
23. J.T. Cadwell *et al.*, Phys. Rev. C **21**, 1215 (1980).
24. O. Adriani *et al.*, arXiv:1407.3669 [physics.acc-ph] (2014).
25. P. Constantin, D.L. Balabanski, and P.V. Cuong, Nucl. Inst. Meth. B **372**, 78 (2016).
26. P. V. Cuong, *"Development of a new surface ion-source and ion guide in the ALTO project"*, PhD thesis, University Paris XI, Orsay (2009).
27. C. Donzaud *et al.*, Eur. Phys. J. A **1**, 407 (1998).
28. E. Cheifetz *et al.*, Phys. Rev. Lett. **25**, 38 (1970).
29. S. Naimi *et al.*, Phys. Rev. Lett. **105**, 032502 (2010).

30. M. Albers *et al.*, Phys. Rev. Lett. **108**, 062701 (2012).
31. C. Thibault *et al.*, Phys. Rev. C **23**, 2720 (1981).
32. C. Sotty *et al.*, Phys. Rev. Lett. **115**, 172501 (2015).
33. W. Urban *et al.*, Eur. Phys. J. A **22**, 241 (2004).
34. M. M. Sharma *et al.*, Phys. Rev. C **61**, 054306 (2000).
35. B. Fogelberg *et al.*, Nucl. Phys. A **429**, 205 (1984).
36. P. Bhattacharyya *et al.*, Phys. Rev. Lett. **87**, 062502 (2001).
37. W. Urban *et al.*, Phys. Rev. C **79**, 037304 (2009).
38. J. M. Mueller *et al.*, Phys. Rev. C **89**, 034615 (2012).
39. V. Bellini *et al.*, Nucl. Instr. Meth. A **204**, 439 (1983).
40. N. S. Rabotnov *et al.*, Sov. J. Nucl. Phys. **11**, 285 (1970).
41. A. Wolf and E. Cheifetz, Phys. Rev. Lett. **36**, 1072 (1976).
42. http://www.caen.it/csite
43. http://www.ortec-online.com/Products-Solutions/index.aspx
44. S. Purushothaman *et al.*, Europhys. Lett. **104**, 42001 (2013).
45. M. Ranjan *et al.*, Nucl. Instr. Meth. A **770**, 87 (2015).
46. P. Constantin, D.L. Balabanski, and P.V. Cuong, Nucl. Instr. Meth. B, in preparation.
47. A. Al-Adili *et al.*, arXiv:1409.0714 [nucl-exp] (2014).
48. M. Ranjan *et al.*, Europhys. Lett. **96**, 52001 (2011).
49. S. Purushothaman *et al.*, Nucl. Instr. Meth. B **266**, 4488 (2008).
50. T. Dickel *et al.*, GSI Scientific Report 2013, 106 (2014); T. Dickel *et al.*, Nucl. Instr. Meth. B **376**, 216 (2016).
51. E. Haettner, "*A novel radiofrequency quadrupole system for SHIPTRAP & New mass measurements of rp nuclides*", PhD thesis, Giessen University (2011).
52. C. N. Davis and D. Peterson, Nucl. Instr. Meth. B **266**, 4449 (2008).
53. Y. Aysto *et al.*, eds. *"Three decades of research using IGISOL at the University of Jyvaskyla"*, Springer, Berlin (2014).
54. I. D. Moore *et al.*, Nucl. Instr. Meth. B **317**, 208 (2013).
55. M. Wada *et al.*, Hyperfine Interactions 199, 269 (2011).
56. W. R. Plass *et al.*, Int. Journal of Mass Spectrometry **349-350**, 134 (2013).
57. K.L. Brown *et al.*, CERN 80-04 (1980); K.L. Brown, Technical Report 91, SLAC (1979).
58. C. Alonso-Arias *et al.*, Nucl. Instr. Meth. **206**, 361 (1983).
59. http://www.eli-np.ro/documents/ELI-NP-GBS-Specifications-rev3-1.pdf